DOCTORAL DISSERTATION

Bio-inspired Propellers toward Safety Collision for Unmanned Aerial Vehicles

BUI Tien Son

Supervisor: **HO Anh Van**

Graduate School of Advanced Science and Technology

Japan Advanced Institute of Science and Technology

Materials Science

March 2023

JAPAN ADVANCED INSTITUTE OF SCIENCE AND TECHNOLOGY

Abstract

School of Materials Science

Graduate School of Advanced Science and Technology

Doctoral Dissertation

Bio-inspired Propellers toward Safety Collision for Unmanned Aerial Vehicles

by **BUI Tien Son**

There is an increasing demand for vertical take-off and landing vehicles, including drones, that are safe to use and can handle collisions. These vehicles face risks of damage from collisions with humans, environmental obstacles, and other drones. To address this issue, researchers have been looking to nature for examples of resilient structures that can be used to design propellers that reduce these risks and increase safety. My proposed solution is a bio-inspired drone propeller called the *Tombo* propeller, which is inspired by the flexibility and resilience of dragonfly wings. In this study, the design and fabrication process for the *Tombo* propeller is presented, which allows it to withstand collisions and recover quickly while still providing sufficient thrust to hover and fly. The performance characteristics of the propeller, such as thrust force, collision force, recovery time, lift-to-drag ratio, and noise, were also investigated through the development of an aerodynamic model and experiments. Additionally, a control strategy was designed for a drone equipped with *Tombo* propellers that could collide with an obstacle, recover from the collision, and continue flying. The results show that the maximum collision force generated by the *Tombo* propeller is less than two-thirds that of a traditional rigid propeller, indicating the potential for using deformable propellers on drones in cluttered environments. To enhance the collision sensing capabilities of the propeller, a novel hub was also introduced, with details on its design, fabrication, force

modeling, and preliminary experiments with potential results. This research has the potential to inform the design of flying vehicles for agile and resilient performance.

Keywords: *Bio-inspired design, Collision accommodation and sensing, Deformable propeller, Soft robotics, Drones' safety*

Acknowledgements

First and foremost, I would like to express my deep gratitude and sincere appreciation to my supervisor, ***Assoc. Prof. Ho Anh Van*** for all the support he has done for me. There are things that are very difficult to write down, and only an insider can understand, I mean, he is always be here, listening, patience, motivating, and sure, all by his enthusiasm and immense knowledge. From the first time I visited Ho Lab. in 2018 until the day of writing this sentence, his office has always been open to me at any time, and for any support I need. I don't know how far I can go without his advisor, but I know that the things I have here are the treasure for me to go on the next journey.

My special thankfulness also goes to ***Prof. Hideyuki Murata*** as my second supervisor, for listening, patience, and keeping my research in the right direction, and ***Prof. Nguyen Le Minh*** for his excellent advice and for opening up my mind to my minor research project.

It has been a fantastic experience and fortunate to study at JAIST and do research in Ho Lab. I would like to thank all colleagues and staff I have had a chance to work with, especially my labmates, for their supportive, collaborative, and family atmosphere. This will be a forever moment in my heart. Thank you all, guys.

To my beloved ***Mrs. Doan Thi Phuong Nga***, I owe you a deep sense of gratitude and apology for your sacrifice. Four years and a half of my absence in eight years of marriage, you have been taking care of our children and yourself. Moreover, you did it without any complaints that made me fade into the shameless. I am looking forward to standing by you in the next chapter of life.

For ***Bun*** and ***Oc***, my little angles, it's a privilege to see you grow up every day, even if it's just through video calls. I will try my best to make up for you, daddy's promise.

Last but not least, my gratefulness goes to my dad, ***Mr. Bui Tien Dong*** and my mom, ***Mrs. Giang Thi Thep*** for the endless love they give to me. I understand how

much silent sacrifice you have made to make your smile whenever we see each other on a video call. I wish you health and happiness forever.

Contents

Abstract **iii**

Acknowledgements **v**

1 Introduction **1**

1.1 Drone collision safety 1

1.2 Research question 3

1.3 Publications 5

1.4 Structure of thesis 6

2 Background and related works **9**

2.1 Collision avoidance 9

2.1.1 Vision-based methods 9

2.1.2 Other contactless methods 11

2.2 Collision impact reduction 12

3 Bio-inspired design for deformable propeller: A case study on dragonfly's *nodus* **17**

3.1 Insect wing and their inspiration for flying robot 17

3.2 Dragonfly's *nodus*: a bio-inspiration for deformable soft joints 21

3.3 *Tombo* propeller design and fabrication 22

3.3.1 Design 22

3.3.2 Fabrication 25

3.3.3 Improvement of *Tombo* propeller quality 27

4 Aerodynamic modelling and simulation for *Tombo* propeller **31**

4.1 Aerodynamic modelling 31

4.1.1 Revisit of the aerodynamic model of a classical propeller . . . 31

4.1.2 The role of deformable angles α, β, and γ 32

4.1.3 *Nodus* modelling 33

Material modelling 33

Structure modelling 36

Hybrid modelling 37

4.1.4 Aerodynamic model of *Tombo* propeller 38

4.2 Aerodynamic simulation 40

4.2.1 Numerical implementation of the aerodynamic model 40

4.2.2 JAXA rFlow3D-based simulation and results 44

4.2.3 *TomboGenerator*: A simulation tool for *Tombo* propeller 46

Airfoil Tool 46

Materials Tool 49

Aerodynamic Tool 49

5 Experimental investigation of *Tombo* propeller's characteristics **53**

5.1 Measurement of *Tombo* propeller's characteristics 53

5.1.1 Thrust force measurement experiments 55

5.1.2 Deformable angle β measurement experiments 55

5.1.3 Time recovery measurement experiments 57

5.1.4 Collision force measurement experiments 57

5.1.5 Noise measurement experiments 59

5.2 Aerodynamic model of the *Tombo* propeller 61

5.2.1 *Nodus*' parameters 61

5.2.2 Aerodynamic model of the *Tombo* propeller 62

5.3 Characteristics of *Tombo* propeller with different configurations . . . 67

6 Fly experiments with *Tombo* propellers **71**

6.1 Recovery control strategy for *Tombo* propeller 71

6.2 Drone setup 72

6.2.1 Hardware 72

6.2.2 PID tunning 74

6.2.3 ROS implementation 75

6.3 Flying test setup 75

6.4 Flying experiments 76

7 *TomboHub*: Collision sensing and shock absorbing **81**

7.1 Structure design 83

7.2 Fabrication 84

7.3 *TomboHub* modelling 85

7.4 Impact force modelling 86

7.5 Twist angle modelling 87

7.6 Torsion spring rigidity coefficient measurement 88

7.7 Experimental setup and results 89

7.7.1 Recovery time experiment 89

7.7.2 Collision force experiment 90

7.7.3 Collision sensing experiments 91

The sensitivity 92

Collision sensing demonstration 92

7.7.4 Flying demonstration 93

8 Discussion and conclusion **95**

8.1 Impact of bio-inspired structure on collision accommodated control for robotics system 95

8.1.1 Design and fabrication 95

8.1.2 Aerodynamics model 98

8.1.3 Flight ability 99

8.1.4 The contribution of *TomboHub* 100
8.1.5 Possible Applications 101
8.2 Directions for future research 103

Bibliography **105**

A Appendix **121**

List of Tables

3.1 Comparison of surface roughness between two methods of fabrication at different parts of *Tombo* propeller 27

4.1 The stress of the Dragonskin series at different strains 36
4.2 The contribution of tendons in the material properties of *nodus* 36
4.3 Parameters of LEPs, TEPs, and attack angle on several sections of a halve of propeller 41
4.4 The coefficients of the interpolated polynomials of $f(x)$ and $g(x)$ . . 41

5.1 *Tombo* propeller configurations used to evaluate the aerodynamic model and observe working characteristics 54
5.2 Collision force and thickness of collided blade of a *Tombo* propeller Conf. 13 at 2500 rpm 59
5.3 Characteristics of *Tombo* propellers and a rigid propeller measured at 2000 rpm of rotational speed 69

7.1 Recovery time of several propellers with/without *TomboHub* 89

List of Figures

1.1 Various applications of drone benefit human lives in many fields . . 1
1.2 Big Techs with drones 2
1.3 Drone crash by bird attack [7], tree, UAVs, and airplane [8] 3
1.4 Safety drone equipped with *Tombo* propellers. Collision-accommodated propellers that can deform passively (A) upon collision and then self-recover (B) to work normally (C) are employed for uncrashed drones. 4

2.1 Drone-equipped vision-based sensors for collision avoidance 10
2.2 Drone-equipped sensors for collision avoidance 11
2.3 Sonar sensor and magnetometer sensor equipped on drones 12
2.4 Drone with special mechanisms toward impact collision reduction . 14
2.5 Resilient propellers 15

3.1 The graph illustrates the distribution of research that involves insect wings across different fields from 2012 to 2018 [53] 18
3.2 Insect's wings accommodate collision with wind and surrounding objects 19

3.3 Several motor-powered, tailless FW-MAVs (miniature aerial vehicles) that are inspired by insects and can fly freely and be controlled, includes (A) Nano Hummingbird from AeroVironment Inc [66]. (B) TechJect Dragonfly from TechJect Inc [67]. (C) BionicOpterfrom Festo AG & Co. KG [68]. (D) iMotionButterflies from Festo AG & Co. KG [69]. (E) Robotic Hummingbird from Texas A&M University [70]. (F) KUBeetle from Konkuk University [71]. (G) Colibri robot from the Universit'e Libre de Bruxelles [72]. (H) Robotic Hummingbird from Purdue University [73]. (I) Quad-thopter from Delft University of Technology [74]. (J) NUS-Robobird from the National University of Singapore [75]. (K) DelFly Nimble from the Delft University of Technology [76]. (L) Butterfly-type Ornithopter from Beihang University [77]. 20

3.4 The dragonfly *B. contaminata* wing (modified from [49]). (A) Structure of dragonfly *B. contaminata* wing. (B) Dorsal side SEM images of the forewing nodus, representing the interface of the pre- and post-nodal parts. The costal and subcostal veins are located on the pre-nodal part of the nodus. The elevated ridge (white arrow) is located on the distal end of the costal vein in the proximal part of the nodus and somewhat covers its distal part. Scale bars: 500μm. (C) Dorsal side CLSM images of the forewing *nodus*. Scale bars: 200μm 21

3.5 *Tombo* propeller was designed with inspiration from the wings of a dragonfly 22

3.6 Original cross-sections for *Tombo* design 23

3.7 *Nodus* – liked hinge of different flapping robots [78], [79] 24

3.8 Effect of deformable Nodus on geometrical characteristics of the *Tombo* propeller 25

3.9 Process for fabrication of the deformable propeller 26

3.10 Injection molds for *Tombo* rigid part fabricating 27

3.11 Improvement of *Tombo* upper end surface quality by injection molding, measured by color 3D laser microscopy VK-9700 (Keyence, USA), 20x, scale bar 500 μm 29
3.12 Damage types of two versions of *Tombo* propeller 30

4.1 *Pressure center* of an airfoil 31
4.2 *Nodus* deformation represent in three deformable angles 32
4.3 Composite structure of *nodus'* material 33
4.4 Stress - strain experiment setup 34
4.5 Stress - strain test result 35
4.6 Structure modelling of *nodus* 37
4.7 The design of a propeller includes a boundary surface element d(S) and geometrical functions L and T. The magenta lines mark the locations where cross-sections are taken to gather data about the airfoil . 40
4.8 rFlow3D's architecture 44
4.9 Bottom up method approach for rFlow3 blade input 45
4.10 Top down method approach for rFlow3 blade input 45
4.11 Process of generating blade grid of *Tombo* propeller by rFlow3D using Airfoil tool as an input processing program, the results of step 3 and step 4 are visualized by Paraview 46
4.12 *TomboGenerator* architecture 47
4.13 Airfoil Tool visualization functions: 48
4.14 The cross-section view of *Tombo* propeller at X = 40 mm 49
4.15 The airfoil properties of the cross-section at $x = 40\,mm$ 50
4.16 Visualization of the deformation of *Tombo* propeller with the output gained from *TomboGenerator* 51
4.17 The detail of *TomboGenerator* architecture 52

5.1 The experiment setup for thrust force measurement experiments: 1 - *Tombo* propeller, 2 - IMADA force gauge ZTS-5N, 3 - Brushless motor X2212 960 KV, 4 - Motor base 55

5.2 The experiment setup for deformable angle β measurement experiments: 1 - *Tombo* propeller, 2 - IMADA force gauge ZTS-5N, 3 - Brushless motor X2212 960 KV, 4 - Motor base, ... 56

5.3 Method of deformation angle β detection: $\beta = acos(\frac{r^d - r^N}{r - r^N})$ where the original radius of a Tombo propeller is denoted as r^d. If the propeller is deformed, its radius is represented by r^d. The distance from the center of the propeller to the beginning of the nodus is referred to as r^d. The camera view angles in the resting state of the propeller are designated as ψ, and when it is in a deformable state, the camera view angles are referred to as ψ^d. The difference between the two camera view angles is represented by δ_ψ, which is calculated as the change in the angle from the deformable state to the resting state 58

5.4 An experiment was conducted to measure the time needed for recovery in a particular scenario, as depicted in Inset A of the setup. This scenario involved a propeller colliding with a simulated human finger 59

5.5 The experiment setup for collision force measurement experiments: 1 - *Tombo* propeller, 2 - IMADA force gauge ZTS-5N, 3 - Optical breadboard, 4 - Acrylic plate, 5 - Collided object, 6 - IMADA force gauge ZTS-500N, 7 - Guide tube, 8 - Rope 60

5.6 Noise measurement method and requirement devices: : 1 - Transmitter for rotational speed control, 2 - Handheld Meter MK09 Sound Lever Meter 60

5.7 Noise measurement results 61

5.8 Comparison of thrust and collision response among *Tombo* propellers with different nodus configurations. Experiments were conducted with three configurations of the *Tombo* propeller (Conf. 1, Conf. 2, and Conf. 3), and a rigid propeller (Conf. 0) in the speed range 2000 rpm to 3200 rpm. The red line plots the estimated thrust force (EsT), the blue line depicts the experimental thrust force (ExT), and the yellow triangles indicate the error of simulation (EoS). The sub-graphs (in boxes within graphs a, b, c, and d) show EsT and ExT of the propeller operating at a speed of 2500 rpm. (a) Conf. 1. (b) Conf. 2. (c) Conf. 3. (d) Conf. 0. 62

5.9 The thrust forces acting on four different configurations of propellers were investigated over a range of rotational speeds up to 18,000 rpm in order to determine the distribution of these forces. The maximum thrust force for each configuration (designated as Conf. 1, Conf. 2, and Conf. 3) occurred at the respective rotational speeds of ω_1, ω_2, and ω_3. 63

5.10 Simulation was conducted to determine the *lift-to-drag ratio* of three different Tombo propellers (Conf. 1, Conf. 2, and Conf. 3) at various rotor speeds. The results showed that the maximum *lift-to-drag ratio* (ε_{mld}) was achieved at specific rotational speeds (ω^1_{mld}, ω^2_{mld}, and ω^3_{mld}) for each propeller, with a value of 2.17. 64

5.11 Simulated lift forces of propellers Conf. 0, Conf. 1, Conf. 2, and Conf. 3 versus rotor power 65

5.12 Simulated deformable angle of Conf. 1 versus rotational speed of rotor 66

5.13 Comparison of theoretical and practical deformable angle β 67

5.14 In Conf. 1, Conf. 2, and Conf. 3, the twist angle γ had the same value of γ_{mtf} and γ_{mld} in both situations where the maximum thrust force and the maximum lift-to-drag ratio were achieved. 68

5.15 Comparison between nine variations of the *Tombo* propeller and a traditional rigid propeller, normalized using the metrics of the rigid propeller. The results are presented in Table 5.1, showing the *Tombo* propeller in various colors and the rigid propeller in black. Table 5.3 contains further information about the metrics used for each *Tombo* propeller configuration in comparison to the rigid propeller. 69

6.1 Illustration of the response strategy that was carried out after the *Tombo* propeller hit a stationary object is provided. 72

6.2 Main hardware of the experimental drone: *Tombo* propellers, pearl markers, a Px4 flying controller, and an onboard computer TX2 Jetson 73

6.3 A standard cascaded control architecture of PX4[5] 73

6.4 PID tuning experiment (case of roll tuning) 74

6.5 During flight tests and collision experiments, the OptiTrack Mocap system was utilized to determine the location of the *Tombo* quadrotor within an indoor setting. This system is specifically designed for motion picture and 3D tracking. 76

6.6 An investigation of how a quadrotor responds to colliding with a *Tombo* propeller obstacle revealed that without a specific reaction strategy in place, the quadrotor would crash to the ground. However, video evidence showed that the reaction strategy was able to stabilize the quadrotor within 5 seconds after the collision. 77

6.7 The records of the quadrotor's position and orientation during the flight and collision experiment reveal that the reaction control mode was activated at the moment of the collision (t_c) and attempted to stabilize the quadrotor in a safe position with coordinates $\mathbf{x}_r = [0.2,\ 0.9,\ -2.0]^{\mathrm{T}}$. It is important to note that the height of the quadrotor is represented by the negative z-coordinate. 78

6.8 Mid-air collision force report 79

7.1 *TomboHub*'s structure idea . . . 82
7.2 *TomboHub* structure includes Hub.Outer 1, Hub.Shaft 3, Hub.Ring 4, Hub.Button 5, Hub.Adapter 8, Hub.Spring 10, Hub.Battery 11, Hub.Screw(s) 12, and Hub.IR.Led(s) 13 . . . 83
7.3 *TomboHub* universal design for assembly with various sizes propeller 84
7.4 *Tombo* Hub fabrication process . . . 85
7.5 Illustration of *TomboHub* collision modelling and rigidity coefficient measurement . . . 85
7.6 Propellers used for experiments . . . 89
7.7 Comparison of collision forces of propellers with and without *TomboHub* 91
7.8 *TomboHub* collision sensing experiment setup . . . 91
7.9 *TomboHub* collision sensing sensitivity performance . . . 92
7.10 *TomboHub* collision sensing demonstration . . . 93
7.11 Succesful hovering demonstration of a drone equipped *TomboHub* . . . 94

8.1 Scalable design for various sizes of *Tombo* propeller . . . 97
8.2 Behavior of two elastic elements in series with external force . . . 101
8.3 An sample state of a supercritical hit . . . 102
8.4 Potential applications of *Tombo* family toward a sustainable solution for nature . . . 102

A.1 Improvement of *Tombo* upper mid surface quality by injection molding, measured by color 3D laser microscopy VK-9700 (Keyence, USA), 20x, scale bar 500 μm . . . 121
A.2 Improvement of *Tombo* upper tip surface quality by injection molding, measured by color 3D laser microscopy VK-9700 (Keyence, USA), 20x, scale bar 500 μm . . . 122
A.3 Improvement of *Tombo* lower end surface quality by injection molding, measured by color 3D laser microscopy VK-9700 (Keyence, USA), 20x, scale bar 500 μm . . . 123

A.4 Improvement of *Tombo* lower mid surface quality by injection molding, measured by color 3D laser microscopy VK-9700 (Keyence, USA), 20x, scale bar 500 μm 124
A.5 Improvement of *Tombo* lower tip surface quality by injection molding, measured by color 3D laser microscopy VK-9700 (Keyence, USA), 20x, scale bar 500 μm 125

List of Abbreviations

VTOL	**V**ertical **T**ake-**O**ff and **L**anding
IMU	**I**nertial **M**easurement **U**nit
LE	**L**eading **E**dge
TE	**T**railing **E**dge
LEPs	**L**eading **E**dge **P**oint**s**
TEPs	**T**railing **E**dge **P**oint**s**
NASA	**N**ational **A**eronautics and **S**pace **A**dministration
JAXA	**J**apan **A**erospace e**X**ploration **A**gency
NACA	**N**ational **A**dvisory **C**ommittee for **A**eronautics
STL	**S**tandard **T**riangle **L**anguage
ROS	**R**obot **O**perating **S**ystem

1 Introduction

1.1 Drone collision safety

FIGURE 1.1: Various applications of drone benefit human lives in many fields

Drones have provided numerous benefits to various industries, such as VTOL which are capable of vertical takeoff and landing. These drones have been used for surveillance, inspection, logistics, transportation, and entertainment (see Figure 1.1). Due to their small size and ability to maneuver in tight spaces, drones have gained interest from both academia and industry, with the potential for a large market [1], [2]. According to Precedence Research, the global commercial drone market is predicted to be worth around USD 504.5 billion by 2030, with a compound annual growth rate of 46.04% between 2022 and 2030 [1]. Additionally, a report by Phystech Ventures states that USD 5 billion Additionally, a report by Phystech Ventures states that [3].

[1] https://finance.yahoo.com/news/commercial-drones-market-size-worth-220000386.html

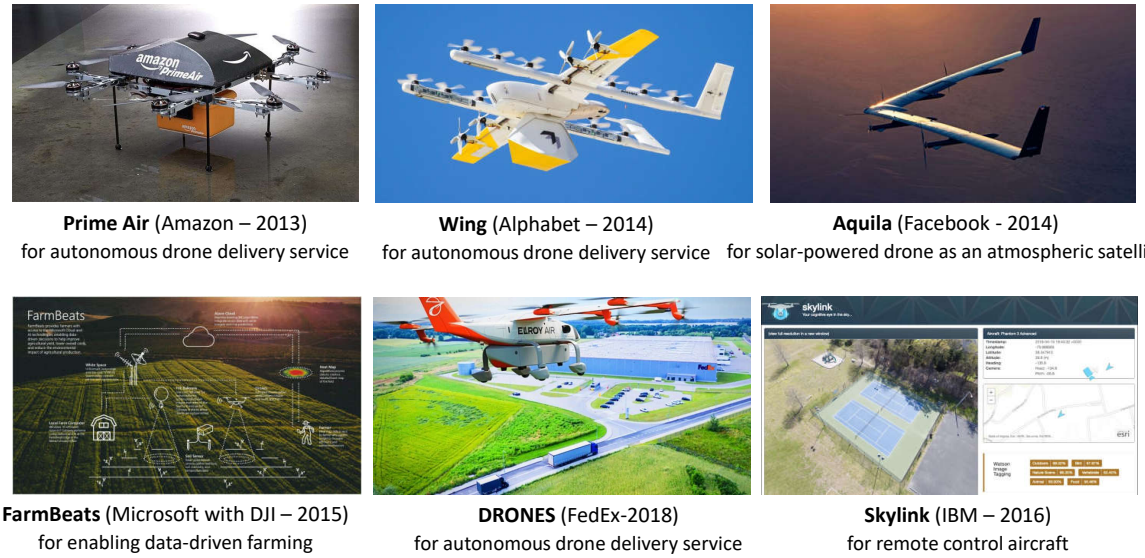

Prime Air (Amazon – 2013)
for autonomous drone delivery service

Wing (Alphabet – 2014)
for autonomous drone delivery service

Aquila (Facebook - 2014)
for solar-powered drone as an atmospheric satellite

FarmBeats (Microsoft with DJI – 2015)
for enabling data-driven farming

DRONES (FedEx-2018)
for autonomous drone delivery service

Skylink (IBM – 2016)
for remote control aircraft

FIGURE 1.2: Big Techs with drones

Several companies have started initiatives to explore the use of drones in different industries. For example, Amazon launched Prime Air in 2013, Alphabet launched Wing in 2014, and FedEx launched DRONES in 2018 for autonomous drone delivery. Microsoft partnered with DJI in 2015 to create FarmBeats for data-driven farming, Facebook developed Aquila in 2014 for a solar-powered drone that could act as an atmospheric satellite, and IBM created Skylink in 2016 for remote control aircraft (as shown in Figure 1.2). Taxis, a traditional industrial service, promises to be a huge potential market as prototypes from many big names such as Boeing [4], Airbus [5], Delta Air Lines[2], and the city of Paris [6] are continuously introduced, and public pilot flights of drone taxis are successful[2] [3] [4].

A major concern in drone operation is the possibility of a collision with the environment (see Figure 1.3). Drones remain sensitive to collision, especially in case of colliding with a propeller. In such a scenario, birds, UAVs, or planes (see Figure 1.3) might create a drone's mid-air crash. As a result, both the environment and the drone itself can suffer damage due to property damage.

If a drone experiences problems with its propellers, it could potentially cause harm to a person or damage property if it were to crash. To address this issue,

[2] https://www.youtube.com/watch?v=4wbFw165ar0&t=3s
[3] https://www.youtube.com/watch?v=WEQk_w0pn_o
[4] https://www.youtube.com/watch?v=x3yz46jN5go

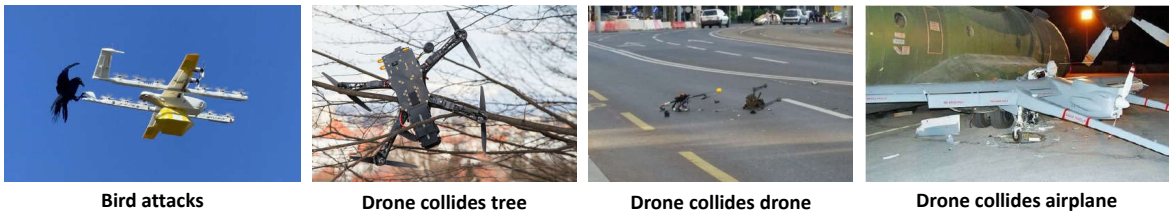

FIGURE 1.3: Drone crash by bird attack [7], tree, UAVs, and airplane [8]

various safety technologies have been developed for drones, such as protective cages and obstacle-avoidance algorithms. These solutions can either add additional weight to the drone or require more processing power, meaning there is a trade-off between efficiency and safety. Despite this, there is a growing demand for drones to be used in crowded areas or close proximity to people, making it necessary to implement measures to prevent accidents or injuries from collisions.

1.2 Research question

There is a balance that must be struck between the safety of drones and their structure and design. While there have been efforts to enhance the structure and perception capabilities of drones in order to prevent collisions, they are still vulnerable to accidents due to technical limitations and unpredictable factors. This is a significant concern as drones are becoming more widely used in a variety of complex and potentially cluttered environments. The question remains: **Is it possible to significantly improve the safety of drones without compromising their basic design and function?**

This dissertation introduces the *Tombo* propeller, which is a bioinspired design that is able to withstand collisions while still providing enough rotation and thrust to keep a drone in the air. The *Tombo* propeller has a unique hinge-like structure, called the nodus, which is made of silicone and fiber tendons and is inspired by the structure and function of a dragonfly wing nodus. This nodus mechanism allows the propeller to self-recover and rotate properly within 0.46 seconds at a speed of 2000 rpm after a collision, allowing drones to bounce back from sudden impacts

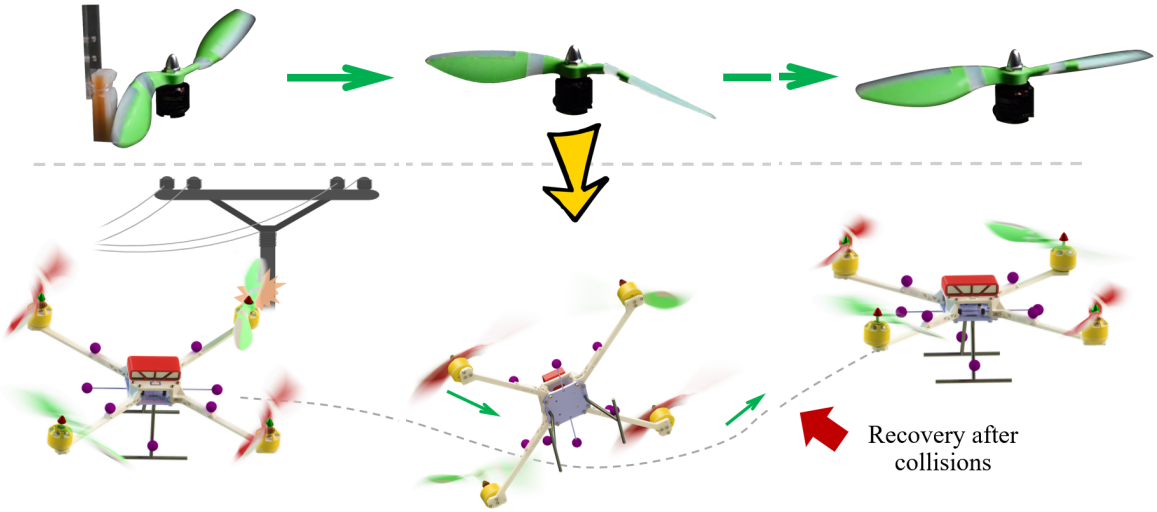

(A) Deforming upon collision (B) Self-recovering (C) Working normally

FIGURE 1.4: Safety drone equipped with *Tombo* propellers. Collision-accommodated propellers that can deform passively (A) upon collision and then self-recover (B) to work normally (C) are employed for uncrashed drones.

with their surroundings. In addition, the *Tombo* propeller is a hybrid design made up of both soft and hard parts, which allows it to regain stiffness and generate enough rotation thrust to keep the drone in the air. Furthermore, the *Tombo* propeller has a deformable leading edge that reduces the impact force and damage inflicted on objects during a collision, making it a safer choice compared to traditional drone propellers. Additionally, an extra mechanism called *TomboHub* was developed to support the collision sensing and shock absorbing for *Tombo* propeller. In this research, the following are the most significant contributions:

1. Proposal of a novel bio-inspired design for drone propellers.

2. The creation of an aerodynamic model of the Tombo propeller, as well as an open-source program for simulating aerodynamic parameters[5]

3. An analysis of the *Tombo* propeller using various configurations of *nodus* has been conducted using both theoretical and experimental methods.

4. Proposal of a control strategy which allows a drone equipped with *Tombo* propellers to recover from collisions.

[5] https://github.com/Ho-lab-jaist/tombo-propeller.git

5. Proposal of a novel design of a collision sensing and absorbing hub for UAVs.

In my Ph.D. research, I conducted a thorough analysis of the Tombo propeller, including examining variations in material composition and configuration as well as different rotational speeds. I also developed a model to characterize the thrust force generated by the propeller, taking into account its deformation and aerodynamic properties. In addition, I proposed several metrics for evaluating and determining the optimal design based on user needs. Furthermore, I tested the flight ability of a drone using the Tombo propellers and suggested a simplified control strategy for recovering a drone after a collision. Finally, I proposed an additional collision-sensing mechanism to support the activation of the automatic control strategy. This is an expansion on previous research [9] which only introduced the design, fabrication, and initial measurement of the thrust force of the Tombo propeller.

1.3 Publications

Journal publication:

S. T. Bui, Q. K. Luu, D. Q. Nguyen, N. D. M. Le, G. Loianno and V. A. Ho, "*Tombo* Propeller: Bioinspired Deformable Structure Toward Collision-Accommodated Control for Drones," in *IEEE Transactions on Robotics*, 2022, doi: 10.1109/TRO.2022.3198494.

IEEE Transactions on Robotics metrics: Impact Factor: 6.835, Eigenfactor: 0.12362, Article Influence Score: 2.451, CiteScore: 14.2; Ranking: Q1 in Computer Science Applications, Q1 in Control and Systems Engineering, Q1 in Electrical and Electronic Engineering; #4 journal in top publications of Robotics by Google scholar.

Conference proceedings:

S. T. Nguyen, H. Nguyen, **S. T. Bui**, V. A. Ho, T. D. Ngo, and H. M. La, "An Agile Bicycle-like Robot for Complex Steel Structure Inspection," in *International Conference on Robotics and Automation (ICRA)*, 2022, doi: 10.1109/ICRA46639.2022.9812153, #1 conference in top publications of Robotics by Google scholar.

1.4 Structure of thesis

In general, this dissertation will describe how bio-inspired structures can benefit novel robotic mechanisms for the accommodation of collision, especially on unmanned aerial vehicles.

- Chapter 1 highlights the potential of the UAVs industry, the current problem, and a question that arises for my research.
- Chapter 2 introduces concrete reviews of the state-of-the-art collision avoidance and collision impact reduction of UAVs. This section also discusses both the advantages and disadvantages of the current solutions, and from that, one again reminds the reader of the research question of this dissertation.
- Chapter 3 shows the bio-inspired design for the deformable propeller, bio-inspired from dragonfly's *nodus*. This section also briefly reviews insect wings and their inspiration for flying robots. Focus on the dragonfly's wing ability for shock accommodation, an investigation of this wing structure is summarized as an inspiration for *Tombo* propeller design. The fabrication and the improvement of *Tombo* quality have been reported.
- Chapter 4 presents in detail the analytical model for aerodynamics parameters of *Tombo* propeller and the simulation in three approaches: Numerical implementation from Matlab, JAXA rFlow 3D-based simulation, and *TomboGenerator* a self-developed simulation tool.
- Chapter 5 investigates the characteristics of *Tombo* propeller through several experiments in comparison with the estimation from Chapter 4. This section also gives a deep discussion about the experimental results, readers can see a huge picture of *Tombo* in various parameters.
- Chapter 6 demonstrates the experiment for a drone equipped with *Tombo* propellers in two cases: with and without a recovery strategy. The fly ability of drones has been confirmed, and the need for a recovery strategy is proved.

- Chapter 7 introduces *TomboHub*, a collision sensing and shock absorbing mechanism, a next step device to support *Tombo* to activate the recovery strategy automatically. The design, fabrication, and initial test results have been reported.

- Chapter 8, finally, summarizes all the findings and contributions presented in this dissertation and discusses potential applications and future research directions to develop the works are also introduced.

2 Background and related works

This section of the discussion looks at various approaches that have been implemented to enhance the safety of **U**nmmaned **A**erial **V**ehicles (UAVs). These strategies can be broken down into two categories: *Collision Avoidance*, which is a proactive approach, and *Collision Impact Reduction*, which is a passive method.

2.1 Collision avoidance

To prevent collisions, various techniques have been suggested, including geometric, force-field, optimized, sense, and avoid [10], [11] (as shown in Figure 2.1 and Figure 2.2). To detect objects within the drone's range, it is advisable to use passive sensors like monocular cameras [12], [13], stereo cameras, and depth cameras [14], [15], or active sensors such as ultrasonic sensors [16], [17], light detection and ranging [18], and radar [19]. It is also possible to use a combination of these sensors [20], [21] for collision avoidance.

2.1.1 Vision-based methods

Vision-based sensors are popular choices for drones because of their extensive range of senses. Herissé et al. use a minimum system including an **I**nertial **M**easurement **U**nit (IMU) and a monocular camera for hovering and landing tasks. This method helps a successful landing on a deck of a sea-going vessel but can not help to avoid other obstacles such as buildings or trees. Multiple stereo cameras were used by Gohn et al. in order to detect obstacles in real-time from any direction by providing 360 degree coverage [22]. An active sense and avoid system for flying robots has been developed by Chen et al., drawing inspiration from the abilities of owls [23].

The system, which is designed for use in dynamic environments, includes a stereo camera and servo motor mounted on a quadrotor, functioning similarly to an owl's head and neck in order to "look around" and track dynamic obstacles while also monitoring the direction of travel, as shown in Figure 2.1b. M. Lacono and A. Sgorbissa employed a depth camera and designed algorithms for an autonomous UAV to follow a path and avoid obstacles indoors. While the results demonstrate that the method is able to adjust in real-time to avoid various types of obstacles, there is no mention of the UAV being able to avoid flying objects [24].

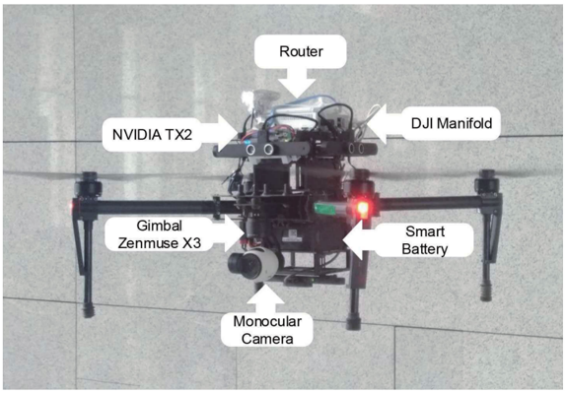

(A) Monocular camera [13]

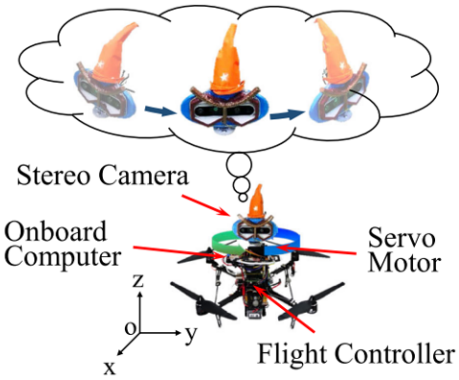

(B) Stereo camera [23]

(C) Depth camera [15]

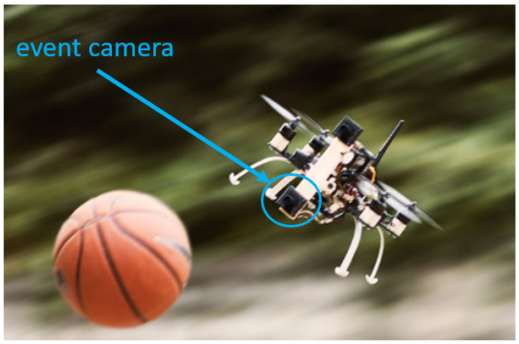

(D) Event camera [25]

FIGURE 2.1: Drone-equipped vision-based sensors for collision avoidance

Despite the wide field of view and high resolution of these cameras, their ability to detect obstacles through their associated algorithm is greatly influenced by factors such as weather, lighting, reflective surfaces, and low visibility due to smoke or fog. Furthermore, these vision sensors work best with stationary objects, but they must still be able to accurately respond to fast-moving images traveling at speeds of over

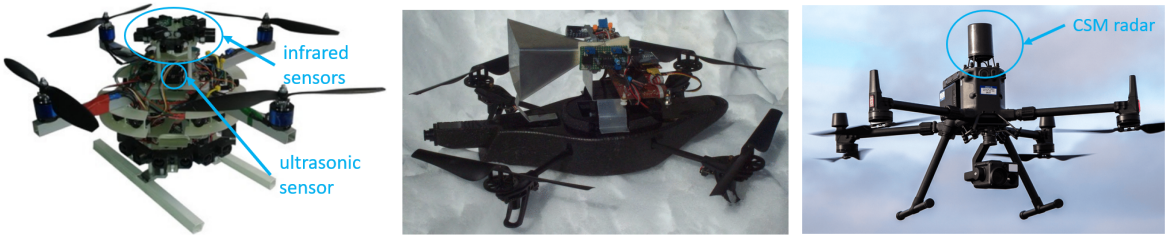

(A) Ultrasonic sensor [17] (B) Self-designed radar [27] (C) CSM radar [28]

FIGURE 2.2: Drone-equipped sensors for collision avoidance

35 km/h [26]. To address the issue of blind spots and improve calculation accuracy, additional sensors are necessary, which can increase the weight and cost of UAVs.

Recently, researchers have explored the use of event cameras on UAVs, finding that they are effective at avoiding fast-moving obstacles [25]. However, event cameras tend to be heavier, larger, and noisier than standard cameras, even at the exact resolution. Additionally, their high noise levels can decrease their accuracy at greater distances, limiting the range of reliable detection to about 1.5 m.

2.1.2 Other contactless methods

Gageik et al. see a set of infrared and ultrasonic sensors as a good and cheap solution to detect obstacles and avoid collision [17]. However, during the experiment, the moving obstacle (person) had a speed of approximately 1 m/s. That speed is quite far from the velocity of natural flying obstacles (such as birds, tennis balls, etc.). Laurijssen et al. introduce sonar sensor as a flexible low-cost sensor solution for drone [29]. However, this is only to prove that the sonar sensor weight is light enough (90 g) to assemble into drone without affect too much to the payload. No flight was conducted. Radar has a more extensive range of sense than the standard cameras and works well with various weather and light conditions [27], [28], [30]. This sensor senses and feedbacks obstacles and their attitude. While the self-design radar in [27] has a big size and a low sensing angle, the CSM radar [28] is a state-of-the-art radar for drones. This CSM camera can detect thin power lines or cable lines and work even at nighttime, which vision-based cameras can not do. Moreover, this modern radar has a large sensing angle of about 360°in the horizontal direction,

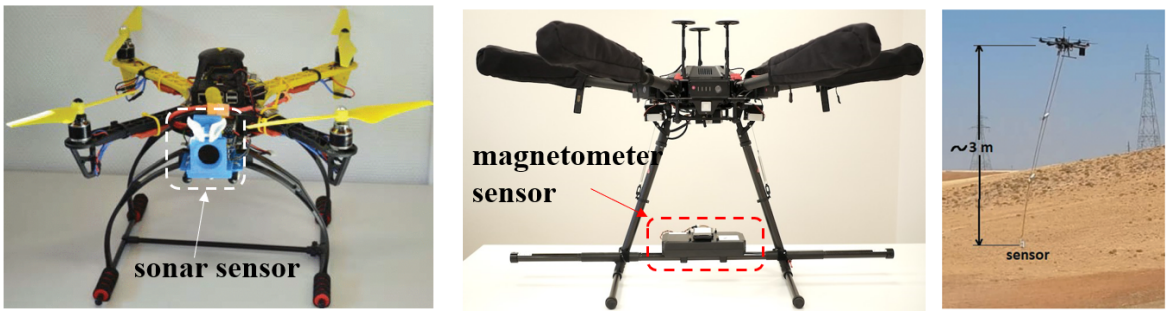

(A) Drone with sonar sensor[29] (B) Drone with magnetometer sensors [31], [32]

FIGURE 2.3: Sonar sensor and magnetometer sensor equipped on drones

60°in the vertical direction, and 45°in the upper direction. Moreover, this CSM radar can detect obstacles at long distances between 1.5 and 30 meters. However, this radar can not sense the below things, such as the top of a tree when it flies above. Overall, the bulky size, the limitation of sensing angle, and the high-cost band the application of radar on small UAVs (see Figure 2.2).

Magnetometer (not the one in drone controller) is another exciting sensor that has been equipped on drones[1] [31], [32]. This sensor was utilized to identify unexploded ordnance, detect the location of underground metal pipes and shielded cables, uncover archaeology, and survey for any metal objects weighing more than a few hundred grams that are buried underground. This function, for sure, can help the drone to avoid some particular cases but can not work with popular non-metal material obstacles such as trees or rocks. In addition, the noise of data becomes more intense when the sensor approaches the metallic object. Therefore, this sensor was limited to obstacle avoidance.

2.2 Collision impact reduction

To reduce the impact of collisions, protective measures must be implemented to safeguard the rotors (actuators) or enable recovery following a collision (as shown in Figure 2.4). One common solution is the use of a cage [33]–[37], which is a cost-effective and easy-to-use option that provides protection for motors and prevents

[1] https://integrated.ugcs.com/magnetometer-drone

multi-directional impacts. However, these cages can be bulky and may increase the risk of collision due to their size, as well as add extra weight to the drone, reducing its flight time. This method is suitable for some tasks, such as underground investigations, where the construction is complex, and the light is weak[2][3].

One possibility for reducing the size and crash risk of UAVs in tight spaces is to utilize foldable structures, as has been suggested in several studies [38]–[40]. These transformations help the drone adapt to the changes in the environment to keep flying. However, the transformation in most cases is not fast enough to deal with the speed of flying obstacles as mentioned above. Additionally, this solution requires extra actuators and mechanisms that increase the drone's weight and reduce flying time. An innovative method that combines both rigid and soft components has been developed to decrease the impact of crashes, absorb collision shock, and maintain resilience during collisions. This approach involves using both rigid guards and deformable mechanisms to achieve these goals [40]–[43]. While resilient drone [41] can deform and reshape impressively, the rotorigami [42] presents a delicate design for impact reduction. Both kinds of drones perform nicely in their showcases but also imply that they can not prevent the shock in the vertical rotor plane. However, integrating systems can be complex and resource-intensive due to the need for a control strategy. scenarios.

Another exciting approach is changing the design of the propeller (see Figure 2.5). Folding propellers [44]–[47] are able to adapt to collisions and return to their original shape due to the presence of rotating joints and the use of centrifugal force. However, these propellers are not able to prevent collisions from occurring from other directions, such as those that occur parallel to the rotor axis as seen with the Aero-Naut CAM carbon folding propeller. Additionally, the time it takes for the propeller to recover after a collision in the air is largely dependent on the use of centrifugal force, which could potentially take longer than what is necessary for the drone to regain control. In addition, assembly error generated by the gap between surfaces

[2] https://www.intelligentliving.co/tokyo-drones-inspect-subway-tunnels/
[3] https://www.commercialuavnews.com/construction/underground-surveys-inspections-drones

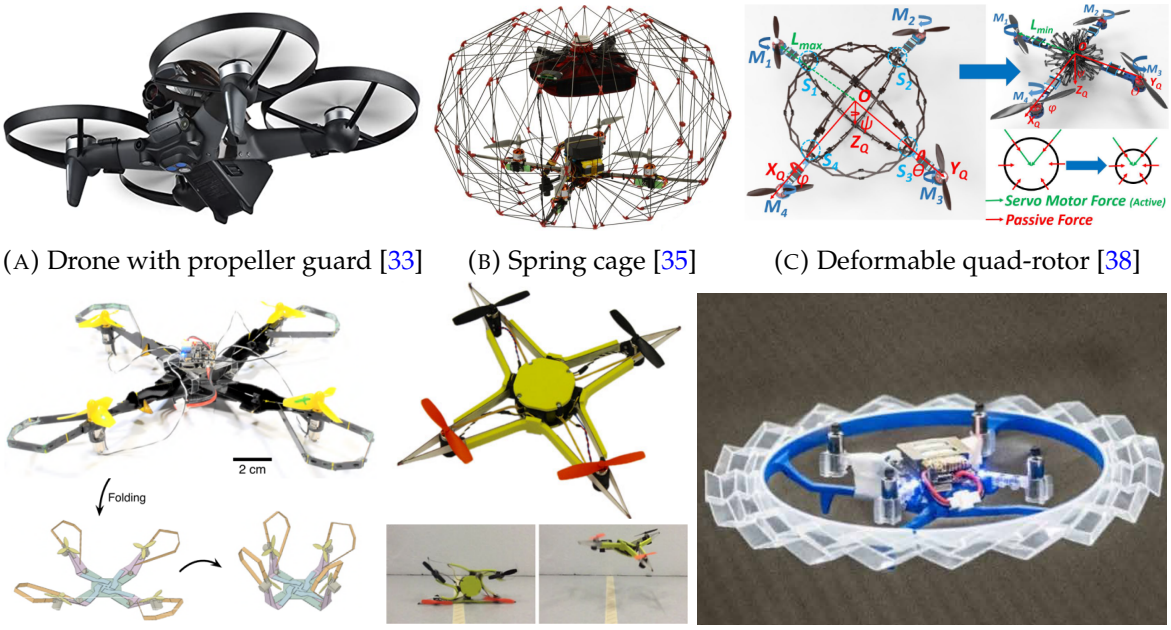

(A) Drone with propeller guard [33] (B) Spring cage [35] (C) Deformable quad-rotor [38]

(D) Foldable arms [40] (E) Resilient drone [41] (F) Rotorigami [42]

FIGURE 2.4: Drone with special mechanisms toward impact collision reduction

and the unbalance of halves of the propeller creates unwanted vibration that must be considered. Our experiment has indicated that cheap resilient propellers have a significant vibration that can not be ignored. There has been increased interest in the concept of a flexible blade [48], which allows a propeller to deform and return to its original shape without the need for additional components when it comes into contact with an object. However, it is still potentially harmful to soft materials like human skin. In addition, none of the practical flight and collision events of a drone equipped with flexible blades were reported. That raises a question of the flight ability of drones with flexible blades in case of strong wind or external impact force applying. Additionally, thin blades that are large in size tend to undergo significant deformations while rotating, which limits the application of these propellers in large unmanned aerial vehicles (UAVs).

The development of technology helps drones become popular with users for various needs. However, a complete safety solution as a standard for drones does not public. This limits the application of drones in closed human environments such as

(A) Aero Naucam prop [45] (B) DJI prop [44] (C) Flexible blade [48]

FIGURE 2.5: Resilient propellers

metropolitan delivery or factories.

3 Bio-inspired design for deformable propeller: A case study on dragonfly's *nodus*

3.1 Insect wing and their inspiration for flying robot

Mother Nature can be seen as the ultimate creator and a valuable source of information for those in the field of robotics research. She provides a wealth of knowledge that can be utilized to find solutions to engineering issues. In order to see the inspiration for insect wings, Hasan and colleagues conducted a study in which they examined over 2700 scientific articles about insect wings and their various applications from 2012 to 2018 using the Web of Science search engine (see Figure 3.1). In Hasan's research, the publications were grouped into 10 categories based on their focus on various aspects of insect wing bio-inspiration. The results indicated that insect wings have excellent efficiency in many research fields, from aerospace to antibacterial. Among these great applications, the collision accommodation of insect wings has strongly attracted researchers in the field. While insects like dragonflies, [49], yellowjackets, and bumblebees [50] are able to collide with objects in their environment without causing any harm or damage, seemingly gliding through with ease [51], [52]. That plays the key in inspiring many insect wing-mimicked flying robots (see Figure 3.3).

Former research indicates that although they are different in size, insect wings share some important features, such as shape, structure, and function. From mosquitoes

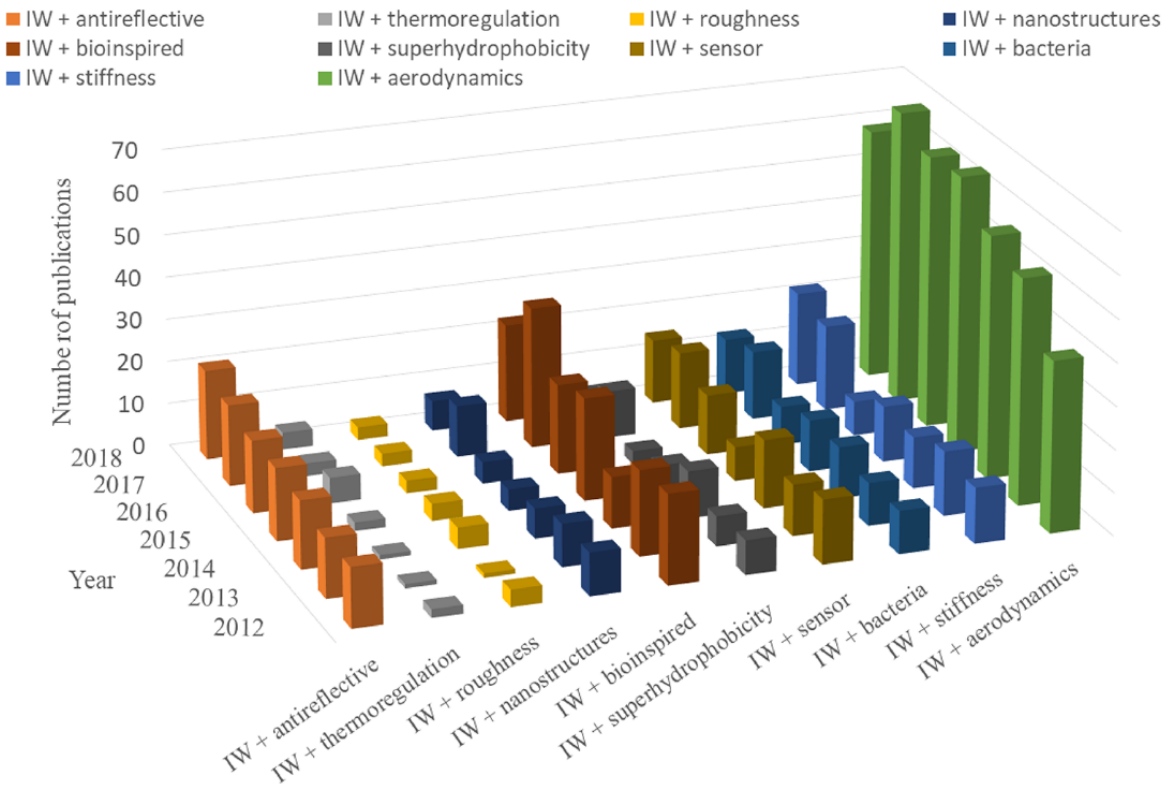

FIGURE 3.1: The graph illustrates the distribution of research that involves insect wings across different fields from 2012 to 2018 [53]

to Goliath beetle, their wings are composed of two membranes that are supported by a rigid vein structure. In detail, the cuticle is used as an exoskeleton to form the shape of the wing [54], [55]. The cuticle, which is found in the wings of insects, displays various characteristics depending on the layer. These characteristics may include the thickness or the materials that make up the cuticle, such as chitin or long-chain hydrocarbons. These properties can vary among different orders and species of insects. Epicuticle is the cuticle outermost layer, which is thin and could be classified into meso-, outer, and inner epicuticle [56]. Multiple studies have analyzed and described the outermost epicuticle layer of various species of dragonflies [57], [58]. The outer layer of a dragonfly's wing is primarily composed of fatty acids and aliphatic hydrocarbons with long chains, such as stearic and palmitic acid.. Procuticle, the next layer of the dragonfly wing, which is grouped into a soft endocuticle and a hard exocuticle, is made of chitin proteins and microfibers. The cross-linking

of quinone compounds attributes to the exocuticle hardness through individual protein molecules within a sclerotization process [54], [59]. The appearance of resilin, an elastic protein, helps the endocuticle become softer [60], [61]. The resilin present in the wings of insects like dragonflies, beetles, and damselflies gives the wings a higher level of stiffness and reduces their ability to be deformed under the pressure of aerodynamic forces. This elastic property helps the wings withstand the forces they encounter while in flight [62]–[64] (see Figure 3.2). Previous research has shown that insect wings can be subjected to stress due to wind gusts and impacts with their surroundings [50]. To deal with these challenges, the structure of insect wings has evolved to incorporate features that help absorb shock and prevent damage upon collision [51], [52]. Note that at the same time, these experiments have indicated that the damage to the insect wings appears mostly on the membrane of the trailing curve. All of this research build a fundamental knowledge about insect wing anatomy that benefits the later researchers to apply to robotic applications.

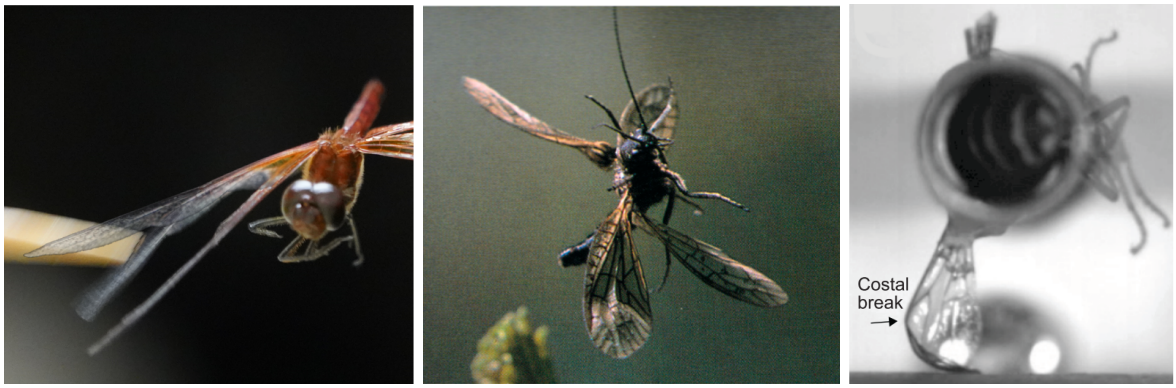

(A) Dragonfly's wing (B) *S. lutaria*'s wing [65] (C) Yellowjacket's wing [50]

FIGURE 3.2: Insect's wings accommodate collision with wind and surrounding objects

These aforementioned interesting characteristics lead to the question of applying the structure of insect wings to aerial vehicles. In my study, I examine the dragonfly wing as a model of shock absorption and self-recovery due to the high flexibility of the nodus, a hinge-like structure [49]. From the perspective of soft robotics, replicating such structures or functions through biomimicry can help improve the safety of drones.

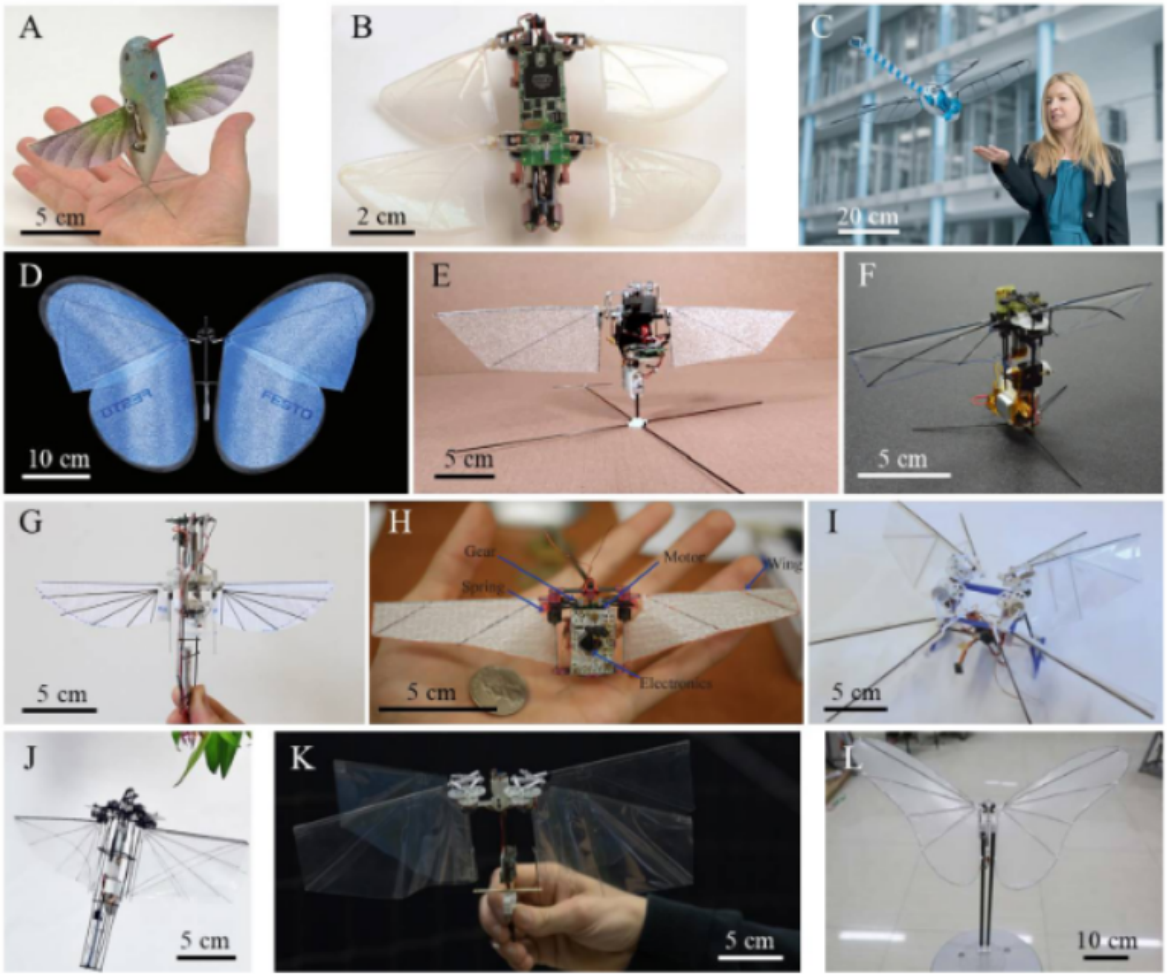

FIGURE 3.3: Several motor-powered, tailless FW-MAVs (miniature aerial vehicles) that are inspired by insects and can fly freely and be controlled, includes (A) Nano Hummingbird from AeroVironment Inc [66]. (B) TechJect Dragonfly from TechJect Inc [67]. (C) BionicOpterfrom Festo AG & Co. KG [68]. (D) iMotionButterflies from Festo AG & Co. KG [69]. (E) Robotic Hummingbird from Texas A&M University [70]. (F) KUBeetle from Konkuk University [71]. (G) Colibri robot from the Universit'e Libre de Bruxelles [72]. (H) Robotic Hummingbird from Purdue University [73]. (I) Quad-thopter from Delft University of Technology [74]. (J) NUS-Robobird from the National University of Singapore [75]. (K) DelFly Nimble from the Delft University of Technology [76]. (L) Butterfly-type Ornithopter from Beihang University [77].

3.2 Dragonfly's *nodus*: a bio-inspiration for deformable soft joints

The *nodus*, a hinge-like structure found in dragonfly wings, plays a vital role in their function. It has the ability to flex in response to external contact without being damaged [49], something that foldable propellers are unable to do. This flexible component, made of resilin similar to rubber, both reinforces the wing's structure and absorbs shock. As a result, the wing maintains its aerodynamic properties while also being able to withstand collisions without being damaged. As discussed above, the insect wing inspires many flying robots. However, because these robots completely mimic the structure of insect wings, the flying principle is flapping (see Figure 3.3). As a result, these robots generate low thrust and are not suitable for delivery tasks. In my research, the insect wing structure and function need to be adapted into a drones with rotational propellers in a novel way.

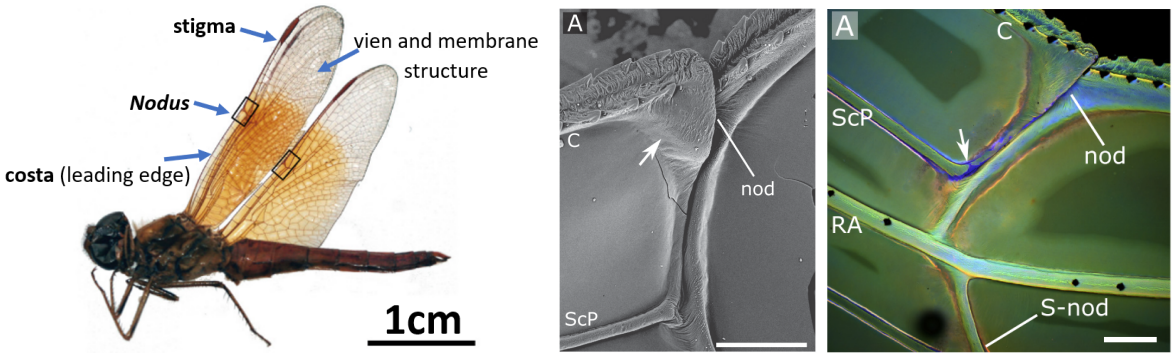

(A) The dragonfly *B. contaminata* (B) *Nodus* SEM image (C) *Nodus* CLSM image

FIGURE 3.4: The dragonfly *B. contaminata* wing (modified from [49]). (A) Structure of dragonfly *B. contaminata* wing. (B) Dorsal side SEM images of the forewing nodus, representing the interface of the pre- and post-nodal parts. The costal and subcostal veins are located on the pre-nodal part of the nodus. The elevated ridge (white arrow) is located on the distal end of the costal vein in the proximal part of the nodus and somewhat covers its distal part. Scale bars: 500μm. (C) Dorsal side CLSM images of the forewing *nodus*. Scale bars: 200μm

In order to apply the insect structure to drone propellers, two main problems must be overcome. Firstly, insect wings with veins and membranes will easily deform when rotating (drone propeller works at thousands of rotations per minute).

Another problem is how to structure and locate the insect's *nodus* for applying to propeller design.

3.3 *Tombo* propeller design and fabrication

3.3.1 Design

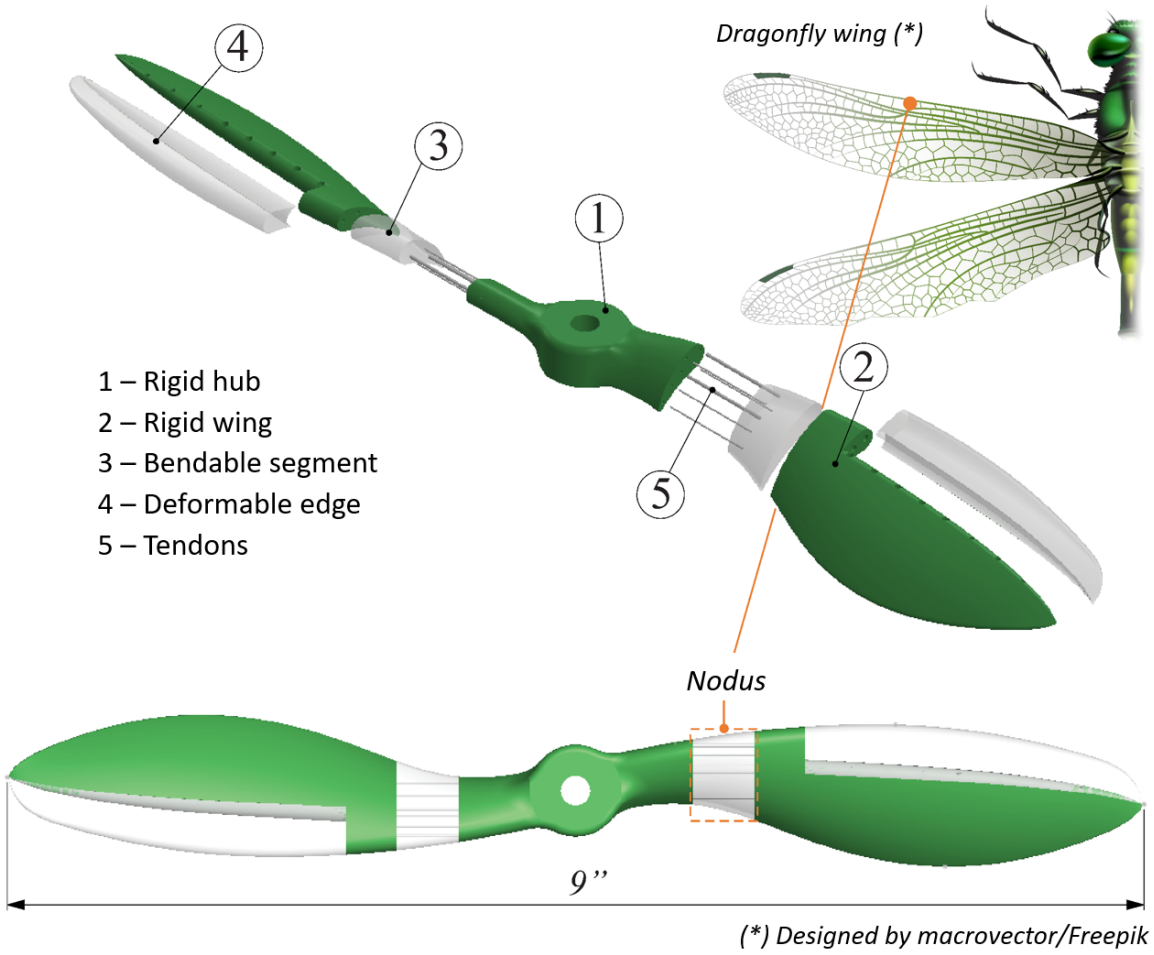

FIGURE 3.5: *Tombo* propeller was designed with inspiration from the wings of a dragonfly

The *Tombo* propeller is a new type of deformable propeller that has been designed based on the characteristics of the dragonfly wing nodus (Figure 3.5). It consists of a hub (1) and wing (2) that are connected by a flexible segment (3) made from silicon rubber and reinforced with nylon fibers, known as tendons (5). The structure of the *nodus* in the Tombo propeller is similar to that of a dragonfly's *nodus*, with the fibers

acting as veins and the silicone rubber functioning as soft membranes. The fibers are distributed evenly within the cross-section of the *nodus* to ensure uniformity in the materials and ease of drilling holes for fiber insertion. An additional deformable edge (4) can also be added to the propeller to allow for quick absorption of an impact during a collision.

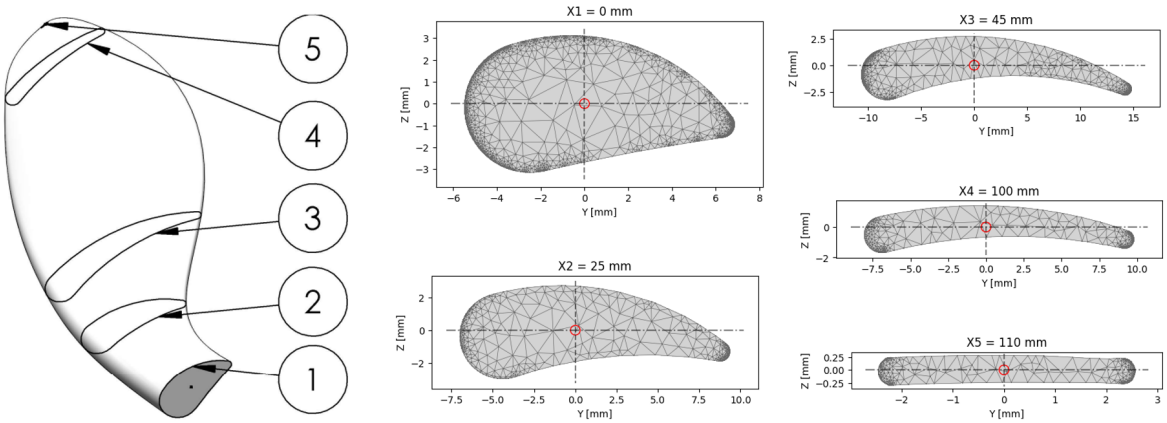

FIGURE 3.6: Original cross-sections for *Tombo* design

Nodus (hinge) is successfully applied in the flapping wing designs toward collision accommodation (Figure 3.7). Although they have different approaches, these designs share the same way of using flexible mechanisms like tendons to bend or twist the flapping wings (such as TPE films [78], or a spring tendon [79]. In the *Tombo* case, the *nodus* of a rotary propeller needs to be stronger than that of the flapping wings. While the flapping wing accepts the soft winding during a flapping beat, the rotary propeller limits the deformation toward a stable rotation. Moreover, the collision force with the external object of flapping wings seems weaker than the rotary propeller's one. In addition, the *nodus* of *Tombo* needs to be done in a hall section, while in the flapping wing, it takes only the rigid frame part. The reason is that the flapping wing mimics the structure of insect wings with frames and membranes, which leads to the need for folding the rigid frames only. Therefore, in my design, the *nodus* consists of several tendons and silicone rubber.

A slow-flying propeller model citeNexusmodels was taken into consideration as a basis for creating the Tombo propeller. By referencing this particular propeller, I

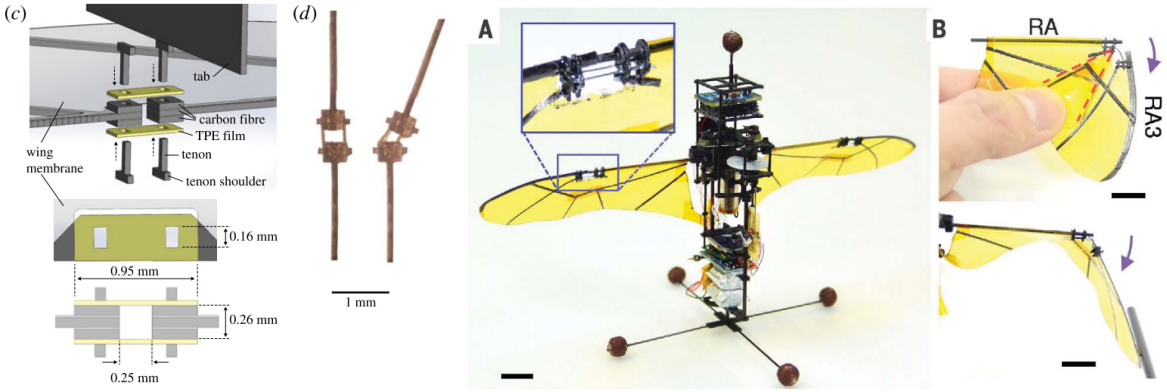

(A) Flying beetle robot hinge design (B) Insect-inspired collapsible wing hinge design

FIGURE 3.7: *Nodus* – liked hinge of different flapping robots [78], [79]

incorporated thick airfoils in the design of the Tombo propeller to ensure an appropriate morphology. In detail, I have used five airfoils (cross sections) at the position of span length at 0, 5, 25, 45, 100, and 110 mm, respectively. The parameters of each airfoil can be seen in Figure 3.6. Then a halve of the propeller was constructed using *Loft function* of SolidWorks CAD software. These thick airfoils can help solve the two problems I have mentioned in section 3.2. These explanation has been described below.

- The airfoils provide a solid structure for stable operation with minimal deformation and vibration, and also allows for the placement of fibers within the *nodus*.
- The *nodus* position was set at the close-to-center part of the propeller to reduce the unwanted effect on aerodynamics.

Additionally, the airfoil along the length of the span can be identified using the airfoil tool of *TomboGenerator*, a software I created for detecting any airfoil from a 3D model of a propeller (the code and implementation can be found in our git project[1]). The detail of this software will be discussed at section 4.2.3.

The mechanical properties and performance of the *nodus* significantly impact the effectiveness of the proposed propeller. As shown in Figure 3.8, the rotation of the

[1] https://github.com/Ho-lab-jaist/tombo-propeller.git

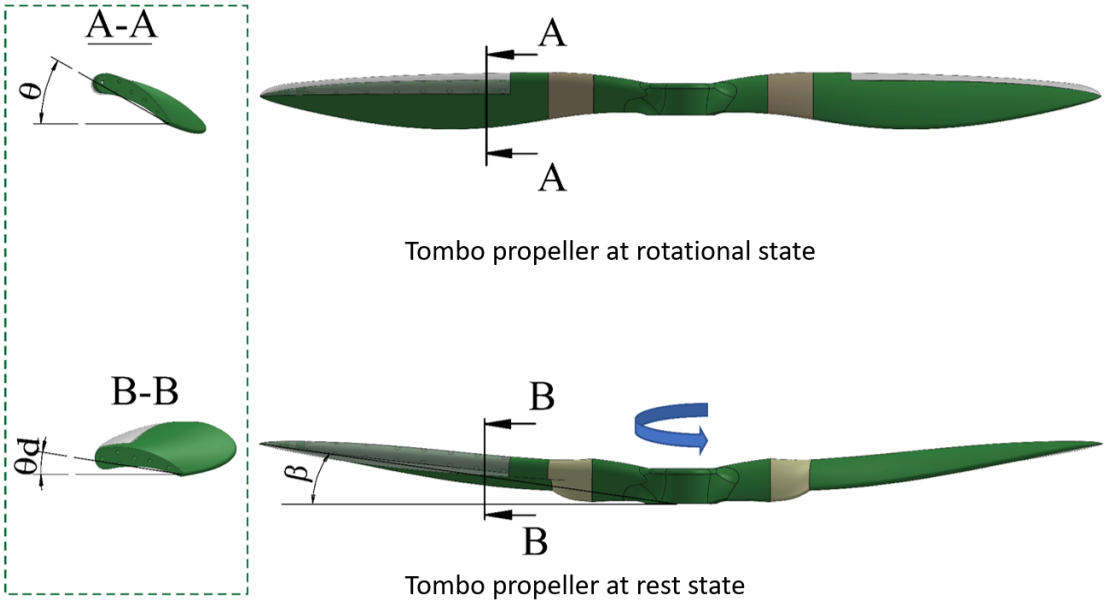

FIGURE 3.8: Effect of deformable Nodus on geometrical characteristics of the *Tombo* propeller

propeller leads to a reduction in the pitch angle, known as theta, due to the deformation of the propeller. This decrease in the pitch angle negatively affects the ability of the propeller to generate thrust, which is heavily dependent on the pitch angle. Additionally, the softness of the *nodus* may affect the stability of a drone using Tombo propellers. As a result, this study investigates various configurations of the *nodus* structure and materials, including the use of silicone rubber with monofilament nylon fibers, in order to determine the optimal construction for Tombo propellers.

3.3.2 Fabrication

The fabrication process for Tombo propellers, as depicted in Figure 3.9, involves seven steps in order to create a fully deformable propeller. The first step involves designing the rigid parts and molds using SolidWorks. The second step involves injecting these rigid parts through the use of injection molding. The third step involves attaching tendons to the rigid parts using adhesive solid glue to form the frame of the propeller. This frame is then placed on an aluminum alloy mold and covered with silicone rubber to create the deformable propeller. The propeller is

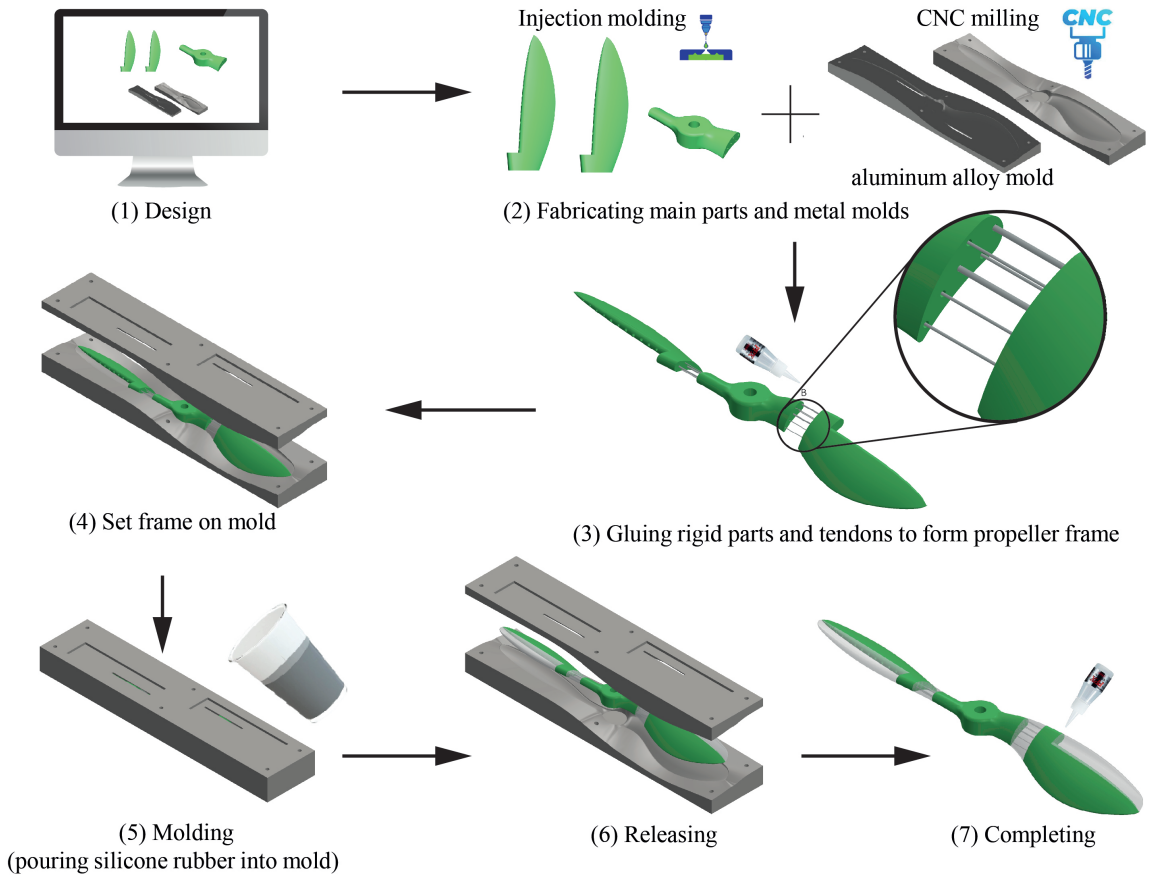

FIGURE 3.9: Process for fabrication of the deformable propeller

then removed from the mold, and finally, PPX glue is used for solid adhesion between the soft and rigid parts. This process is used not only for the propeller shown in Figure 3.9, but also for smaller sizes such as 5, 9, 10, 20 inches.

In previous work [9], the rigid parts of the propellers were made of Acrylonitrile Butadiene Styrene (ABS) through the use of Fused Filament Fabrication (FFF) 3D printing, which resulted in a layered structure that reduced strength upon lateral impact. Therefore, in this work, a new model is proposed in which the rigid parts are fabricated through injection molding like commercial rigid propellers to improve the uniformity of the Tombo propeller. In order to improve the surface quality, particularly the nodus-like part, the molds were made of aluminum alloy fabricated through CNC machining rather than ABS 3D printing.

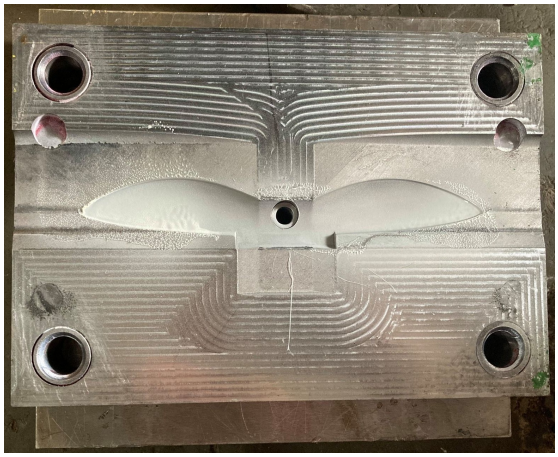

(A) Mold for fabricating wing

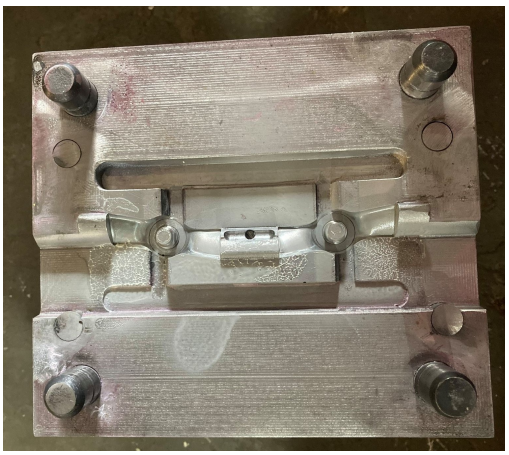

(B) Mold for fabricating shaft

FIGURE 3.10: Injection molds for *Tombo* rigid part fabricating

TABLE 3.1: Comparison of surface roughness between two methods of fabrication at different parts of *Tombo* propeller

	Upper end	Upper mid	Upper tip	Lower end	Lower mid	Lower tip
	Rz, Ra [m]					
Tombo v1	96.693, 8.588	107.246, 8.494	107.246, 8.494	7116.48, 7.274	85.829, 7.981	85.829, 7.981
Tombo v2	62.670, 1.288	109.519, 0.800	56.695, 1.484	38.156, 1.510	88.154, 0.649	43.312, 0.638

3.3.3 Improvement of *Tombo* propeller quality

Using aluminum alloy molds in injection molding helps to increase the quality of the *Tombo* propeller clearly. In order to evaluate the improvement of the *Tombo* surface quality, I have used the color 3D laser microscopy VK-9700 (Keyence, USA), 20x, scale bar 500 μm to measure both *Ra* (the average of the absolute heights of the profile over a specific period of time) and *Rz* (the average of the absolute heights of the five highest peaks and the depths of the five lowest valleys within the same time frame) of the end, middle, and tip area of each *Tombo* surface version. The result has been summarized in Table 3.1. Overall, it can be seen that the surface roughness of the *Tombo* propeller's second version is relatively lower than that of the first version.

Firstly, while the roughness *Ra* of the second version is almost one-eighth of that of the first one, the roughness *Rz* does not show the same results. The main reason is that the surface quality of injected part copies the surface quality of the injection mold, which can be improved massively by **C**omputer **N**umerical **C**ontrol

(CNC) machining and high-skill manual finishing. In contrast, the quality of 3D printed objects based on the diameter of the nozzle and the precision of printer axis movement can not be compared with that of the CNC machine (see Figure 3.11). Note that, the other images of *Tombo* surface roughness at the middle and the tip of both versions can be found in Appendix A. Moreover, the surface roughness *Rz* of the two propeller versions shows similarities in the center position of the wing, but there is a large difference in the tip and tip positions of the wing. This is explained by the morphology of the wing when the curvature diameter (in the flatwise direction) is largest and gradually decreases towards the ends of the wing. Therefore, in the center position, the wing surface is flatter than the two ends, leading to quite similar results, while at the wing tips, the change in pitch (due to the small curvature) causes difficulty for the 3D printing method. As a result, the roughness *Rz* between these locations is different.

Next, I have used these *Tombo* propellers for durability tests for normal tasks of a drone to clarify the damage types of both versions. The detail of each test is described in Chapter 5. While the Tombor first version used to break after a critical collision, the second version can stand several critical ones without total damage. Figure 3.12 shows the improvement of *Tombo* durability in the next version, while most damages focus on the tip and tendon. None of the broken at the rigid part of the wing has been reported, again confirming the injection method's success in the advantages of *Tombo* quality.

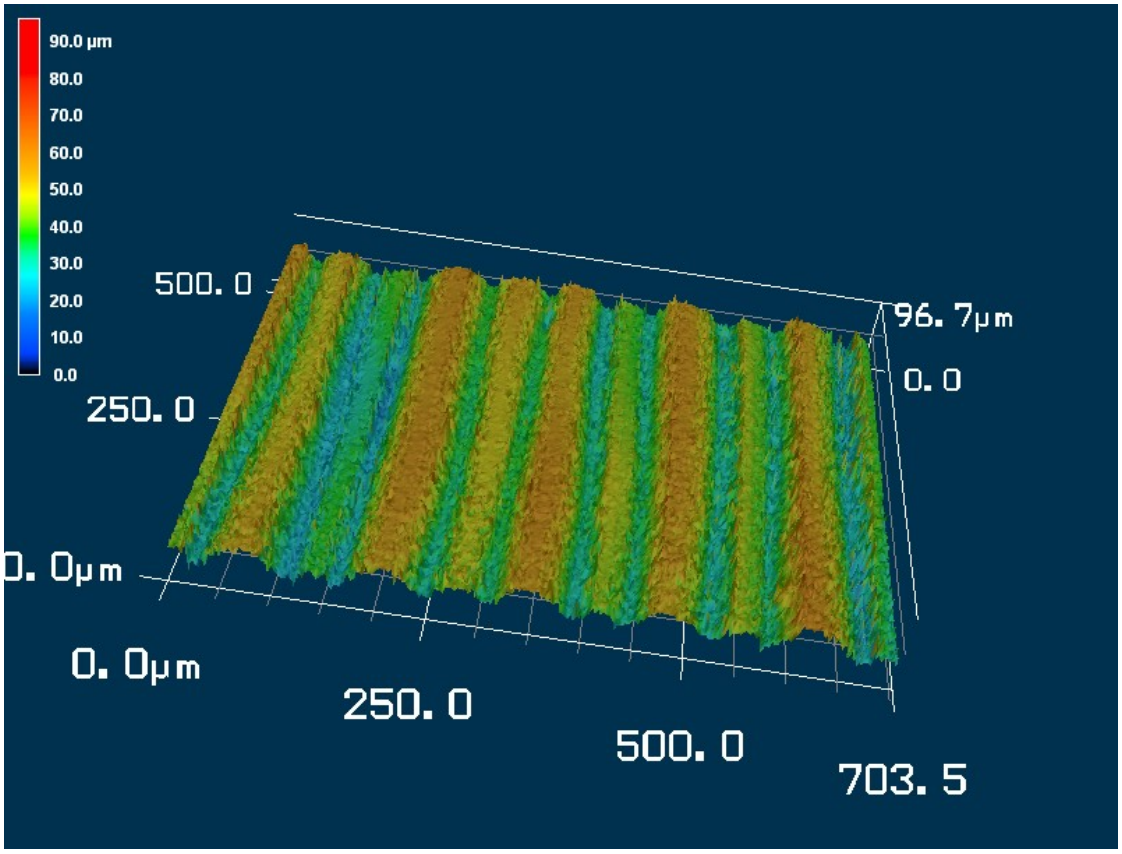

(A) *Tombo* v1 upper end

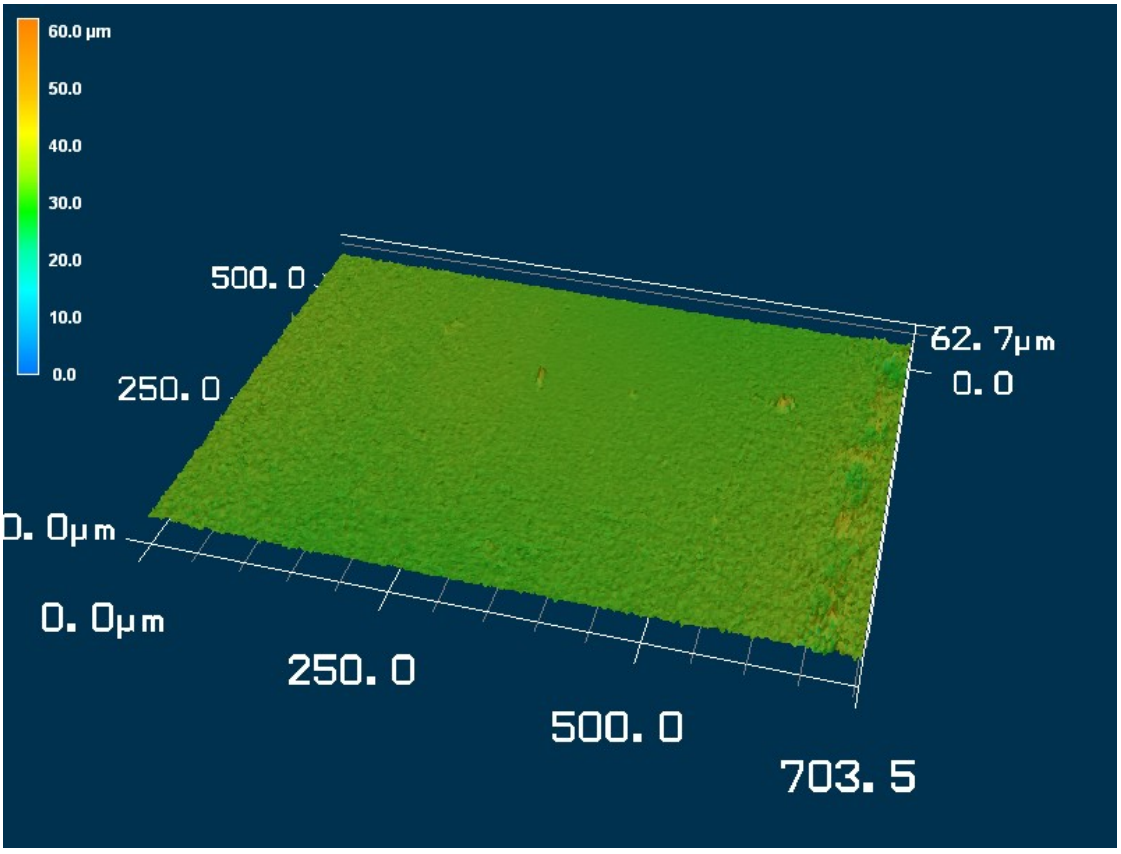

(B) *Tombo* v2 upper end

FIGURE 3.11: Improvement of *Tombo* upper end surface quality by injection molding, measured by color 3D laser microscopy VK-9700 (Keyence, USA), 20x, scale bar 500 μm

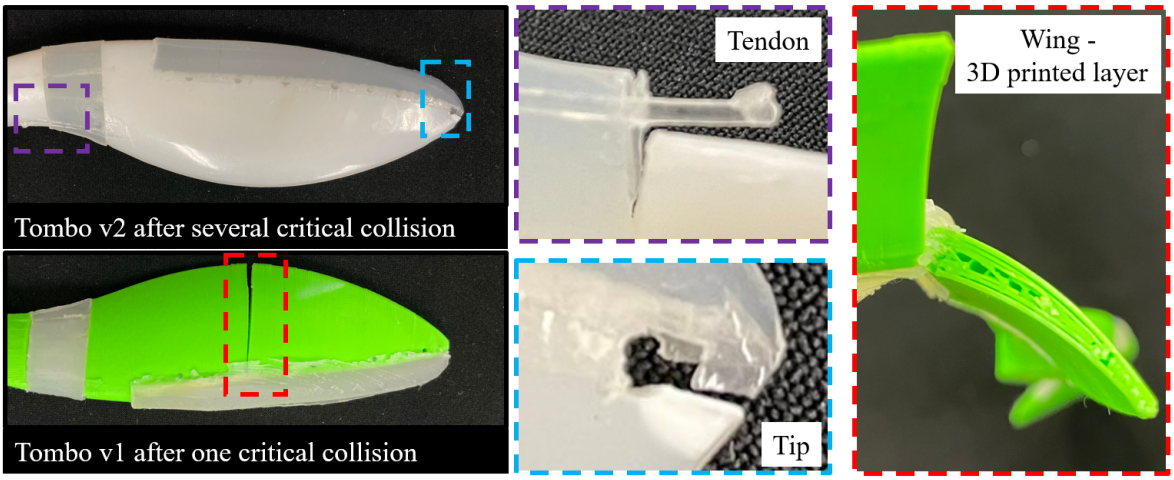

FIGURE 3.12: Damage types of two versions of *Tombo* propeller

4 Aerodynamic modelling and simulation for *Tombo* propeller

4.1 Aerodynamic modelling

4.1.1 Revisit of the aerodynamic model of a classical propeller

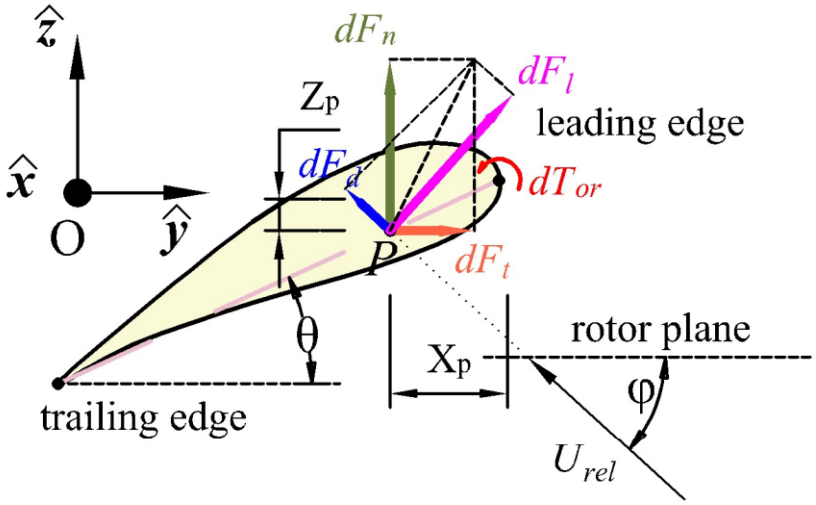

FIGURE 4.1: *Pressure center* of an airfoil

There are established models for the aerodynamics of standard propellers and quadrotors [80]–[82]. The main aerodynamic factors, including the normal force (F_n), tangential force (F_t), lift force (F_l), and drag force (F_d) (seen in Figure 4.1), can be calculated using this equation below.

$$F_i = \int_p \rho \omega^2 C_i \mathrm{d}S x^2 \mathrm{d}x, \qquad i \in \{n, t, l, d\} \tag{4.1}$$

where the length of the span for the airfoils, denoted as P, is a function that is determined in advance. The density of the air is represented by ρ, and the rotational speed is represented by ω. The aerodynamics force coefficients noted as $C_i = C_i(\theta)$ (see [83]), is a function that depends on the pitch angle, represented by θ, which is also a function that is predetermined and shown in Figure 4.1). The boundary surface function, represented as S, is also predetermined. The length of the span element along the airfoils is represented by x.

4.1.2 The role of deformable angles α, β, and γ

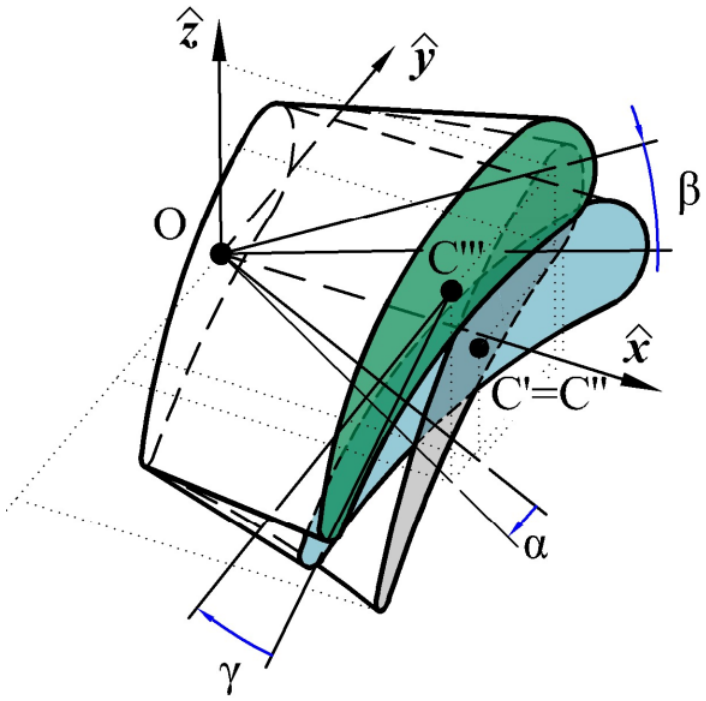

FIGURE 4.2: *Nodus* deformation represent in three deformable angles

The *nodus*' ability to deform helps protect the propeller from collision damage, but it can also cause deformation during rotation. Specifically, the rotation of a rotor causes displacement of the rigid wing, which is measured by the bending anglesα, β, and twist angle γ shown in Figure 4.2. These deformable angles change the shape of the propeller, including the pitch angle θ, and affect the aerodynamic forces F_d and F_l. Therefore, a Tombo propeller's aerodynamic model must take these deformable angles into account to ensure the device functions efficiently.

To assess the flexibility of the angles, I utilize a combination of composite and beam models to analyze both the material and structure (morphology) of the *nodus*.

4.1.3 *Nodus* modelling

Material modelling

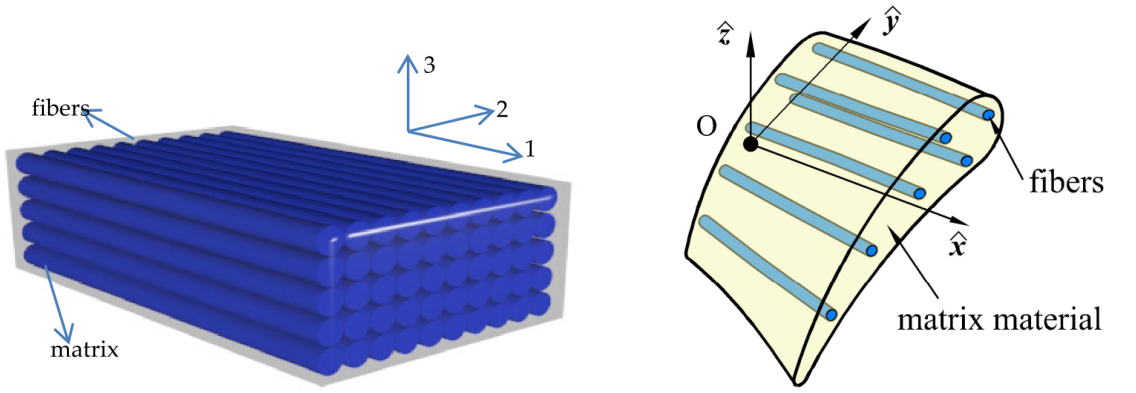

(A) Composite structure [84] (B) Composite structure of *nodus'* material

FIGURE 4.3: Composite structure of *nodus'* material

Based on the design of the *nodus*, it appears to be made up of a combination of silicone rubber and a tendon serving as the material matrix and reinforced fibers, respectively (as shown in Figure 4.3b). The compliance material matrix [M] of the composite beam is defined as [84].

$$[M] = \begin{bmatrix} \frac{1}{E_{yy}} & \frac{-\nu_{yz}}{E_{yy}} & \frac{-\nu_{yx}}{E_{yy}} & 0 & 0 & 0 \\ \frac{-\nu_{yz}}{E_{yy}} & \frac{1}{E_{zz}} & \frac{-\nu_{xz}}{E_{zz}} & 0 & 0 & 0 \\ \frac{-\nu_{yz}}{E_{yy}} & \frac{-\nu_{xz}}{E_{zz}} & \frac{1}{E_{zz}} & 0 & 0 & 0 \\ 0 & 0 & 0 & \frac{1}{G_{xz}} & 0 & 0 \\ 0 & 0 & 0 & 0 & \frac{1}{G_{yz}} & 0 \\ 0 & 0 & 0 & 0 & 0 & \frac{1}{G_{yz}} \end{bmatrix} \tag{4.2}$$

According to Younes et al.'s research on composite modelling [84], the Chamis model was chosen due to its high accuracy in predicting elastic modulus coefficients in various matrix and fiber materials. This model defines the Young modulus E_N and the shear modulus G_N of *nodus* as follows:

$$E_N = \frac{E^m}{1 - \sqrt{v^f}(1 - \frac{E^m}{Ef})}, G_N = \frac{G^m}{1 - \sqrt{v^f}(1 - \frac{G^m}{G^f})}, \tag{4.3}$$

where the fiber volume fraction, denoted as v^f, is a measure of the percentage of fiber area within the composite cross-section. It ranges from 0 to 1 and has a significant impact on the mechanical properties of the *nodus*. The Young modulus and shear modulus of the matrix material are represented by E^m and E^m, respectively, while the Young modulus and shear modulus of the fiber material are represented by E^m and G^f. By altering the number of fibers or their diameter, the fiber volume fraction v^f can be modified, leading to a corresponding change in the stiffness of the *nodus*.

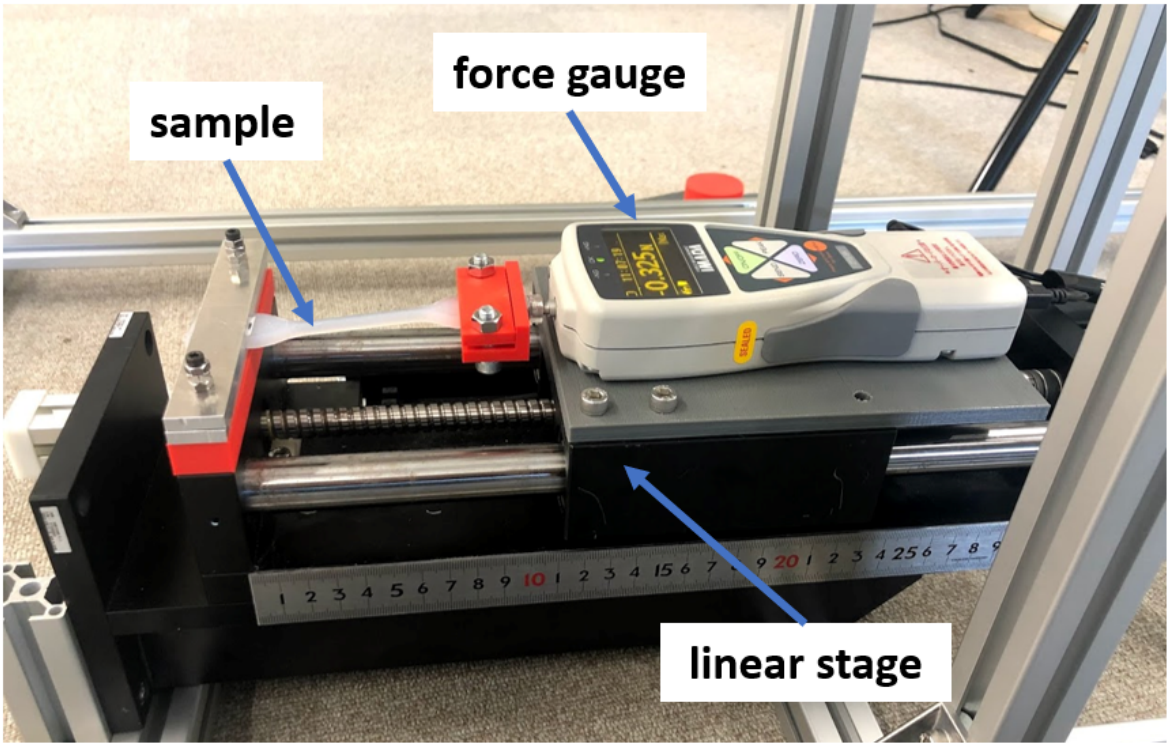

FIGURE 4.4: Stress - strain experiment setup

Therefore, material characteristics of nodus required the Young and Shear modulus of the silicon rubber (matrix material) and the tendon (fiber). I have done a stress-strain experiment to measure the Young modulus of DragonSkin 10, DragonSkin 20, and DragonSkin 30 (Smooth-On, Inc., USA) at various strain ratios. The experiment apparatus and results have been shown in Figure 4.4 and Figure 4.5. The samples are created from the DragonSkin series, which follows the ASTM 412 Die D dumbbell size and shape standards set by the American Society for Testing and Materials, and fixture by a linear stage (Suruga Seiki Co., Ltd - Japan). I controlled and recorded the movement of this linear through a controller by Matlab 2019b. Two force gauges (IMADA Co.,Ltd, Japa) 5N and 50N have measured the applied force on the sample at two ranges (the first one with a high ratio for the range of strain (from 1% to 20%), the second one for the range from 20% to 300%). The test has been taken in these ranges due to the working of *nodus* strain are defined lower 20% during the flying process with the size of a 9-inch propeller and the rotational speed under 8000 rpm.

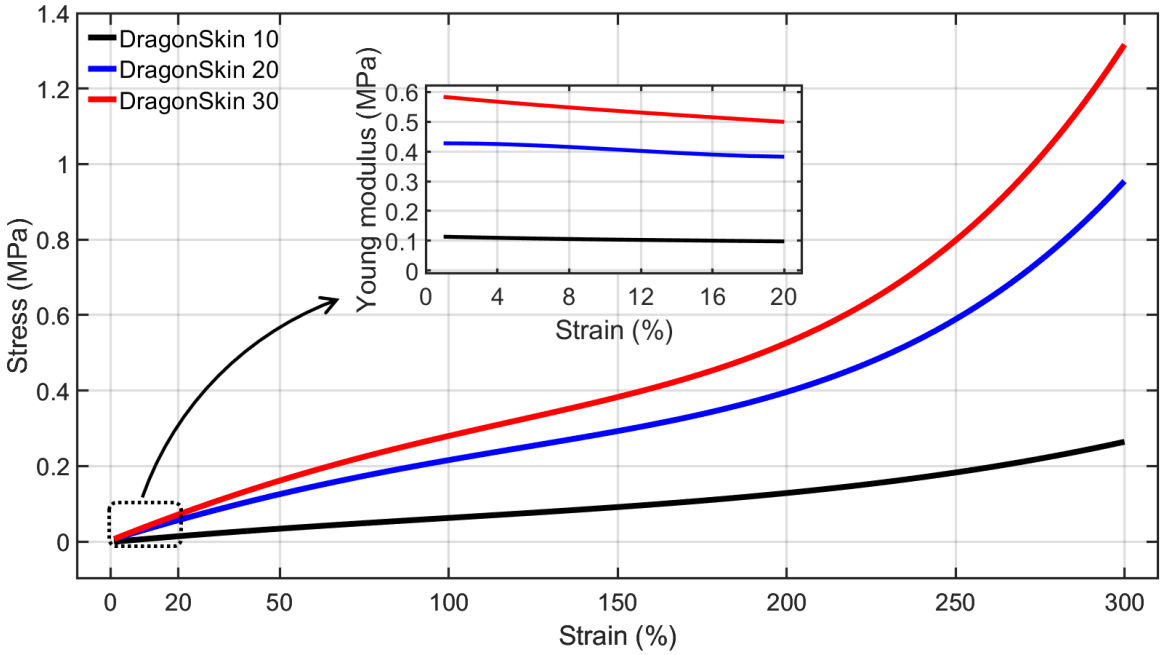

FIGURE 4.5: Stress - strain test result

Table 4.1 compares the stress of the Dragonskin series at different strains from the manufacture datasheets, my experiment, and other research. In my experiment,

TABLE 4.1: The stress of the Dragonskin series at different strains

Stress	Manufacture datasheets [1]		My experiment		Other experiments	
	psi	Pa	psi	Pa	psi	Pa
DragonSkin 10 (100% modulus)	22	151,685	11.8	81,333	39	271,722 [85]
DragonSkin 20 (100% modulus)	49	337,843	44.7	308,000	-	-
DragonSkin 30 (100% modulus)	86	592,949	56.2	387,333	58	398,000 [86]
DragonSkin 20 (30% modulus)	-	-	15.7	108,133	20	140,951 [87]

TABLE 4.2: The contribution of tendons in the material properties of *nodus*

Nodus (strain = 1%)	*Tombo*'s Conf. 1		*Tombo*'s Conf. 2		*Tombo*'s Conf. 3	
	with tendons	without tendons	with tendons	without tendons	with tendons	without tendons
Young modulus (KPa)	151	113	570	427	775	580
Shear modulus (KPa)	54.1	40.5	203.7	152.4	276.9	207.1

I record the stable data in 5 minutes at each step and twice in tests of a sample. The result indicates that none of the publications share the same extensive strain range as my experiment. While Dragonskin 20 data in my experiment is close to the official datasheets, Dragonskin 10 and 30 show the difference. Additionally, my Dragonskin 30 result is close to the publication from Ranzani et al. [86]. Moreover, the data varies between one experiment at different conditions of strain processing [88]. Therefore, I keep using my result to do the next step due to the extensive result range and the stable results.

Next, the Young and shear modulus of *nodus* of Conf. 1, Conf. 2, and Conf. 3 are calculated and summarized in Table 4.2. Here, both Young's modulus and shear modulus see a significant improvement with the appearance of tendons. Therefore, it can be said that the tendons contribute to the behavior of the nodus in bending or twisting.

Structure modelling

My hypothesis was that the *nodus* would follow the behavior of a cantilever beam with one fixed end as it rotated (refer to Figure 4.6a). To model the deformable angles of a stationary cantilever at a specific rotation speed, we used beam modeling. Based on this, the bending angles α in the Oxy plane and β in the Oxz plane of the

Tombo propeller were determined according to [89] as follows:

$$\alpha = \frac{F_{BN}^{y} L_N^2}{2E_N I_N^z} \qquad \beta = \frac{F_{BN}^{z} L_N^2}{2E_N I_N^y}, \tag{4.4}$$

where the forces from the wing applied to the nodus are represented by F_{BN}^{y}, F_{BN}^{z} while L_N refers to the *nodus* length and E_N represents the Young modulus of the *nodus*. I_N^y and I_N^z are the inertial moments of the cross-section of the *nodus* in the $\hat{y}$ and $\hat{z}$ directions, respectively. It can be seen from Equation 4.4 that there is a strong connection between the *nodus* length, the position of the cross-section, and the deformable angles α and β.

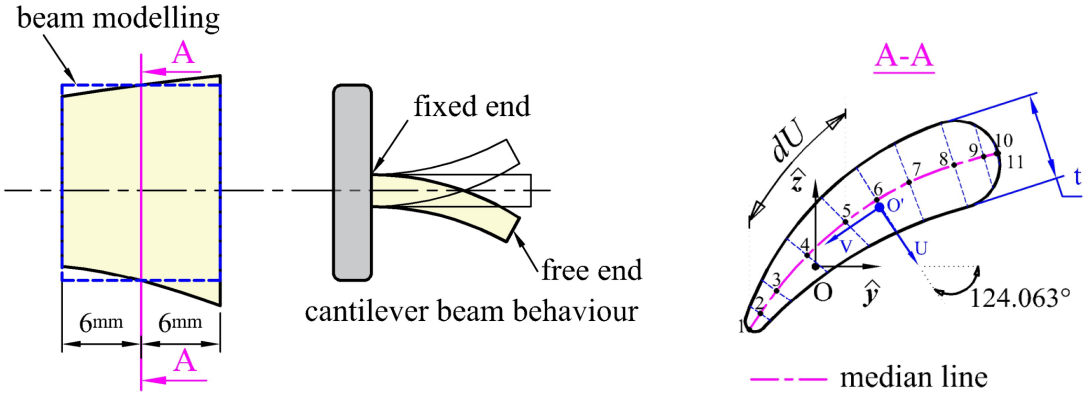

(A) Deformation of *nodus* as a cantilever beam deflection (B) The *representative cross-section* parameters

FIGURE 4.6: Structure modelling of *nodus*

Hybrid modelling

In order to study the mechanical properties of the nodus, we employed a hybrid modeling approach that took into account both material and structural models. However, we found that the composite models discussed in [84] and the beam model [89] often assume a high level of material homogeneity and a standard cross-sectional area structure, which do not accurately reflect the *nodus* with its different directions of nylon tendons and variable morphology along its body. As a solution, we proposed using a *representative cross-section* (shown in Figure 4.6b) located in the

middle of the *nodus* (section A-A) for all related calculations. This particular cross-section was chosen to simplify the modeling process and account for the unique features of the *nodus*. The twist angle γ of a Tombo propeller can also be defined as an elongated cross-section, as described in [90].

$$\gamma = \frac{3(1 + \frac{4F}{3A_N U^2})T_{or}L_N}{G_N F}, \tag{4.5}$$

Here, the applied torque, represented by T_{or}, is caused by the aerodynamic forces F_d and F_t. It is calculated by taking into account the infinitesimal length along the camberline (dU), the area and length of the camberline on the representative cross-section (A_N and U), and the length of the *nodus* (L_N). The thickness of the airfoil, perpendicular to the median line, is also considered (t). The *center of pressure* at the quarter-chord point, denoted as P, can be used to define the applied torque element (dT_{or}). This information can be found in references [81], [91] and is illustrated in Figure 4.1.

$$\mathrm{d}T_{or} = \mathrm{d}F_t \frac{\mid y_{LE} - y_{TE} \mid}{4} + \mathrm{d}F_d \frac{\mid z_{LE} - z_{TE} \mid}{4}, \tag{4.6}$$

where the coordinates of the front and back edge of the cross-section in the $\hat{x}$ and $\hat{z}$ directions are represented by y_{LE}, z_{LE}, y_{TE}, and z_{TE}. y_{LE}, z_{LE}, y_{TE}, and z_{TE}.

4.1.4 Aerodynamic model of *Tombo* propeller

At a particular rotational speed, it was assumed that the shape of the deformable propeller remained unchanged. Therefore, the aerodynamic forces acting on a *Tombo* propeller could be calculated using Equation 4.1. It was also assumed that the optional deformable edge (4) of the propeller did not change shape during rotation, so its influence was considered insignificant in the computational model. The main factors influencing the deformable angles in the model were the span length, aerodynamic force coefficient, and boundary surface. The aerodynamic forces acting on

the propeller were made up of three components generated by the hub, the *nodus*, and the wing, which could be explained as follows:

$$F_i = F_i^h + F_i^N + F_i^w, \qquad i \in \{n, t, l, d\} \tag{4.7}$$

I can use Equation 4.1 to determine both F_i^h and F_i^N due to the rigidity of the hub and the fact that the nodus length is approximately 10 % the length of the propeller. Regarding the aerodynamic force of the *Tombo* propeller's wing [81], it is necessary to consider the influence of the deformable angles as below.

$$F_i^w = \int_{P^{de}} \rho \omega^2 C_i^{de} \mathrm{d}(S^{de}) x^2 \mathrm{d}x, \qquad i \in \{n, t, l, d\} \tag{4.8}$$

where The deformable span length function, P^{de}, along the airfoils is influenced by the deformable pitch angle function, θ^{de}(x), of the Tombo propeller airfoil, represented by $C_i^{de} = C_i(\theta^{de}(x))$. The deformable boundary surface function, S^{de}, an P^{de} can also be determined by the projections of the wing in the $\hat{x}$ direction and the Oxy plane when deformation occurs. It is important to note that the position of the wing can be described using the rotation matrix, $\mathbf{R}(\alpha, \beta, \gamma)$, which belongs to $SO(3)$ and involves a sequence of roll, pitch, and yaw rotations around the axes of a fixed reference frame [92]:

$$\mathbf{R}(\alpha, \beta, \gamma) = \mathbf{R}(\hat{z}, \alpha)\mathbf{R}(\hat{y}, \beta)\mathbf{R}(\hat{x}, \gamma), \tag{4.9}$$

where the functions α and β represent the bending angles of the nodus on the Oxz and Oxy planes, respectively. The twist angle around the centroid contour along the nodus is represented by γ. $\mathbf{R}(\hat{x}, \gamma)$, $\mathbf{R}(\hat{y}, \beta)$, and $\mathbf{R}(\hat{z}, \alpha)$ are rotations around the $\hat{x}$, $\hat{y}$, and $\hat{z}$ axes of the fixed reference frame (as illustrated in Figure 4.2), respectively.

To clarify the change in the boundary surface function, I divided the wing into three planes: Oxy, Oyz, and Ozx. This allowed me to calculate the equation for the aerodynamic forces acting on the wing, which is shown below.

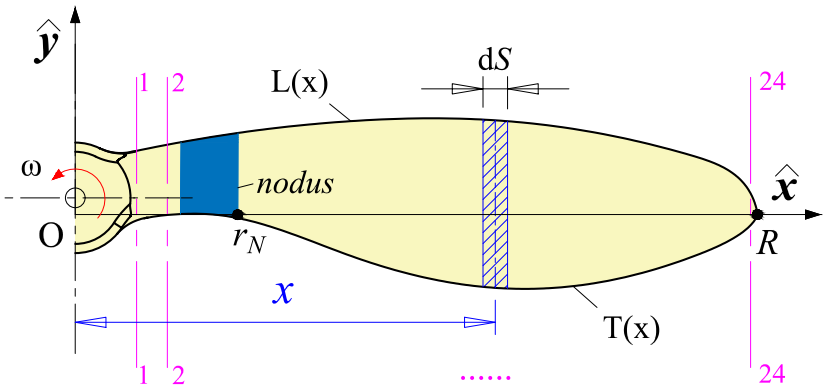

FIGURE 4.7: The design of a propeller includes a boundary surface element d(S) and geometrical functions L and T. The magenta lines mark the locations where cross-sections are taken to gather data about the airfoil

$$F_i^w = \int_{r_N}^{R} \rho\omega^2 C_i^{de} \frac{\cos\alpha\cos\beta\cos(\theta-\gamma)}{\cos\theta}(L-T)\,x^2\mathrm{d}x, \qquad i \in \{n,t,l,d\} \tag{4.10}$$

where the radii of the inner and outer curvatures of the design are denoted by r_N and R, respectively, starting from the nodus. The leading and trailing edges have specific geometrical functions represented by L and T.

Using SolidWorks 2020 and AutoCad 2022, half of a propeller was analyzed by dividing it into 24 cross-sections along the span (as shown in Figure Figure 4.7 and Table 4.3). The angle of attack and the coordinates of the leading and trailing edges were collected for each section. Then, using the polyfit function in Matlab R2020b, the L, T, and θ functions were determined based on the span length. The coefficients of the interpolated polynomials of f(x) and g(x) are presented in Table 4.4. Note that the mean square error of each poly-fitted function is under 0.6%.

4.2 Aerodynamic simulation

4.2.1 Numerical implementation of the aerodynamic model

According to the principle of the model, there is an inherent issue caused by the relationships between the input variables. While non-linear techniques can address this

TABLE 4.3: Parameters of LEPs, TEPs, and attack angle on several sections of a halve of propeller

Section number	**Leading edge points**		**Trailing edge points**		**Angle of attack**
	X coordinate [m]	**Y** coordinate [m]	**X** coordinate [m]	**Y** coordinate [m]	[degree]
1	0.015	0.00831	0.015	-0.00265	36.34
2	0.02	0.00919	0.02	-0.00243	37.99
3	0.025	0.01001	0.025	-0.00286	37.9
4	0.03	0.01076	0.03	-0.00399	36.56
5	0.035	0.01139	0.035	-0.00562	34.78
6	0.04	0.01191	0.04	-0.0075	33.03
7	0.045	0.01231	0.045	-0.00937	31.51
8	0.05	0.01261	0.05	-0.01104	30.21
9	0.055	0.01278	0.055	-0.01243	29.07
10	0.06	0.01281	0.06	-0.01351	28.03
11	0.065	0.0127	0.065	-0.01426	27.08
12	0.07	0.01241	0.07	-0.01467	26.19
13	0.075	0.01195	0.075	-0.01473	25.34
14	0.08	0.01132	0.08	-0.01442	24.53
15	0.085	0.0105	0.085	-0.01376	23.75
16	0.09	0.0095	0.09	-0.01275	23
17	0.095	0.00832	0.095	-0.01139	22.29
18	0.1	0.00697	0.1	-0.00972	21.58
19	0.105	0.0052	0.105	-0.00769	20.71
20	0.106	0.00468	0.106	-0.0072	20.5
21	0.107	0.00405	0.107	-0.00666	20.28
22	0.108	0.00325	0.108	-0.00605	20.09
23	0.109	0.0022	0.109	-0.00534	19.8
24	0.11	0.0007	0.11	-0.00445	19.48

TABLE 4.4: The coefficients of the interpolated polynomials of $f(x)$ and $g(x)$

	x_{min}[mm]	x_{max}[mm]	**polynomials**
Part I	10	25	$f(x) = -13.5 + 0.5185x - 0.00739x^2$ [m]
			$g(x) = -1.3 + 0.2219x + 0.0052735x^2$ [m]
			$\theta(x) = -29900 + 1356.9x + 22.739x^2$ [rad]
Part II	25	110	$f(x) = 27.893 + 0.590x - 0.551x^2 + 0.012x^3$ [m]
			$g(x) = -35.52 + 3.697x + 0.0504x^2 + 0.01015x^3$ [m]
			$\theta(x) = -27306.8 + 6959.764x - 741.005x^2 + 53.295x^3$ [rad]
Part III	110	111	-

issue, a more straightforward method involving an iterative loop until convergence is reached may be more practical. This approach has been demonstrated through Algorithms 1 and 2, which were applied to a traditional propeller and a *Tombo* propeller, respectively (see our git project[2] for more details).

Algorithm 1 Aerodynamics Parameters Estimation for Rigid Propellers

Input: Airfoil parameters, air density ρ, and rotational speed of propeller n_r
1: $N :=$ number of cross-sections
2: $S_C = \{S_i : [x_{C_i}, y_{LE_i}, z_{LE_i}, y_{TE_i}, z_{TE_i}, \theta_{C_i}]\} :=$ coordinate of leading edge and trailing edge, and pitch angle $i \in \{1, ..., N\}$
Output: Arodynamics forces F_j, $j \in \{n, t, l, d\}$
3: *//Separate geometric functions into parts by order*
4: $k :=$ Number of geometrical function parts
5: $o_i :=$ Order of the ith part
6: $F_i := 0$
7: **for** $i := 1$ to k **do**
8: $\quad P_i :=$ polyfit$(x_C, y_{LE}, y_{TE}, o_i)$
9: $\quad F_j :=$ polyfit$(x_C, C_j(\theta_C), o_i)$
10: **end for**
11: **return** F_j

Both algorithms were used for estimating the aerodynamic forces of rigid propeller and *Tombo* propeller and the results have been shown in Section 5. This approach is suitable when approximating the aerodynamic parameters of a single propeller model. However, it also has many disadvantages as below:

1. Manual handling

2. Requires commercial softwares (SolidWorks, AutoCAD, Matlab)

3. Large total errors can arise from accumulating errors through each step.

All of these disadvantages leads me to find another solution for *Tombo* aerodynamic simulation, which I will introduce in the next section.

[2] https://github.com/Ho-lab-jaist/tombo-propeller.git

Algorithm 2 Aerodynamics Parameters Estimation for *Tombo* Propellers

Input: Airfoil functions, representative section, *nodus* parameters, air density ρ, and rotational speed of propeller n_r, loop options

S_C, k, P_i, L, T := Airfoil parameter and functions
U_C, A_C, F := *Representative cross-section* parameters
$E_N, G_N, I_C^x, I_C^z, x_N, L_N$:= Young's and shear modulus, coordinate and length of *nodus*
$nbIt$:= Maximum number of iterations
Tol := Acceptance tolerance

Output: Arodynamics parameters F_j, C_j, $j \in \{n, t, l, d\}$, Tor, lift-to-drag ratio ε_{lod}

//LOOP
loop
  $\alpha = \alpha(F_d, E_N, I_C^z)$
  $\beta = \beta(F_t, E_N, I_C^x)$
  $T_{or} = T_{or}(F_{t2}, F_{d2}, \theta_C)$
  $\gamma = \gamma(T_{or}, G_N, F_C)$
  $F_j^w = F_j(\rho, n_r, \theta_C, C_j, x_N, L_N), j \in \{n, t, l, d\}$
  //Calculate the results
  $F_j = F_j^h + F_j^N + F_j^w$
  //Convergence Criteria
  if $i > nbIt$ **then**
    break
  else
    if $|F_t - F_t last| + |F_d - F_{dlast}| < Tol$ **then**
      break
    end if
  end if
end loop
return F_j, C_j, T_{or}, and ε_{lod}

4.2.2 JAXA rFlow3D-based simulation and results

rFlow3D is a bash programming analysis tool developed by **J**apan **A**erospace **E**xploration **A**gency (JAXA) to solve the three-dimensional compressible Navier-Stokes equations of aerial vehicle propeller based on the input data [93]–[98]. This software can perform flight dynamics analysis (trim analysis), aerodynamic loading (CFD analysis), elastic deformation analysis (CSD analysis), and particle calculation. The output of rFlow3D can be visualized by third-party software such as Techplot[3] or Paraview[4]. Figure 4.8 shows the architecture of rFlow3D.

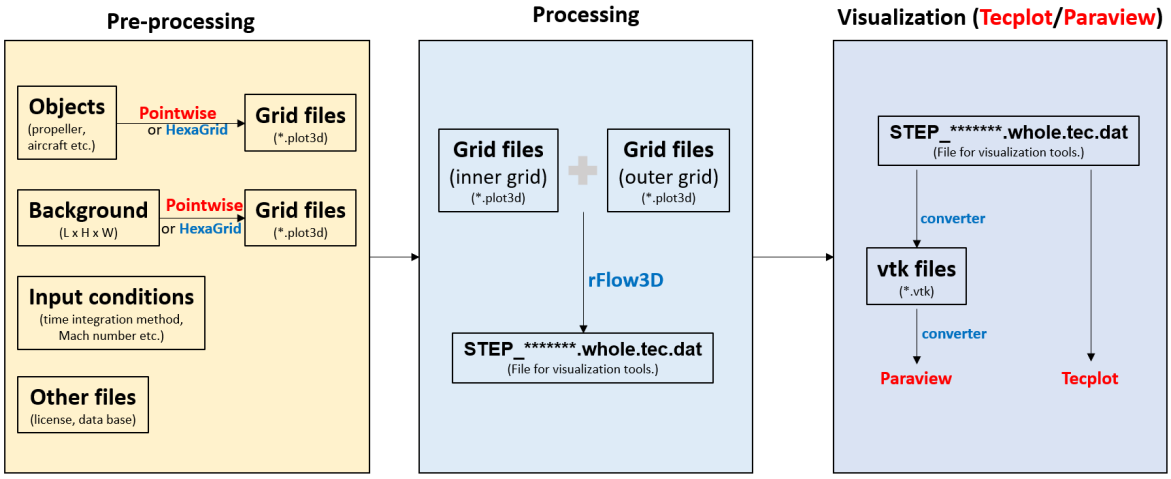

FIGURE 4.8: rFlow3D's architecture

The input of rFlow3D includes the object information (propeller/blade, aircraft, etc.), the background (length x height x weight), and the simulation conditions (time integration method, Match number, etc.). While the simulation conditions are an editable text file (*.txt), and the background file can be generated by a Jaxa-developed program (SOH3D.exe), the blade information required standard airfoils for development. In detail, the user can choose the code (four digits or five digits) to generate a **N**ational **A**dvisory **C**ommittee for **A**eronautics (NACA) airfoil. This approach is called a bottom-up method (see Figure 4.9). However, in our design, the original airfoils (see Figure 3.6) are customized. That leads to developing a program (Airfoil tool) to generate cross-sections from arbitrary propeller 3D models (see Figure 4.10).

[3] https://www.tecplot.com/
[4] https://www.paraview.org/

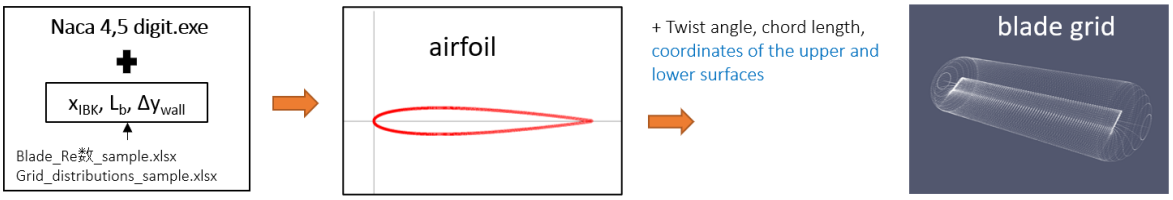

FIGURE 4.9: Bottom up method approach for rFlow3 blade input

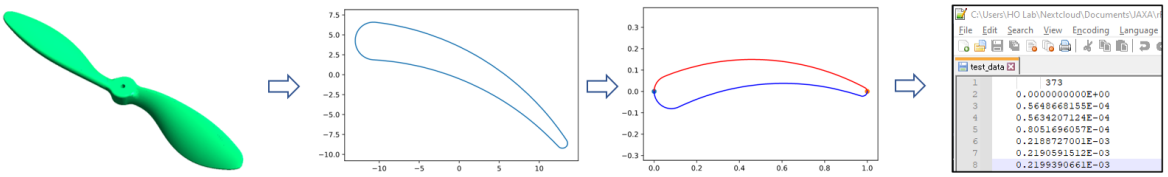

FIGURE 4.10: Top down method approach for rFlow3 blade input

In fact, this top-down approach program has been built successfully and was used to create input files for rFlow3D software. This program can make a cross-section at a point with a normal vector, and after that, it transforms all airfoils into the standardized one (twist angle equals 0 and chord length is 1 unit length) by a rotation step and scaling step in this sequence. The output of this program is a Fortran format file (see Figure 4.10). Finally, the blade grid of a *Tombo* propeller has been simulated by using five cross-sections at $r/R = 0.2, 0.4, 0.62, 0.8$, and 1 of span length (see Figure 4.11).

The simulation for the deformable propeller has not been done by rFlow3D. Firstly, rFlow3D is designed for a high accuracy for aerodynamic simulation based on a deep computing method [99], it requires a high computational load. For example, a simulation for ten revolutions of *Tombo* propeller costs more than 300 hours for computing by a desktop computer with Intel(R) Core(TM) i9-10850K CPU @ 3.60GHz, 64.0 GB installed RAM configuration. Moreover, the implementation of soft material into a rFlow3D model is complex and easy to errors. Overall, these challenges motivate me to develop an specialized program for *Tombo* propeller simulation.

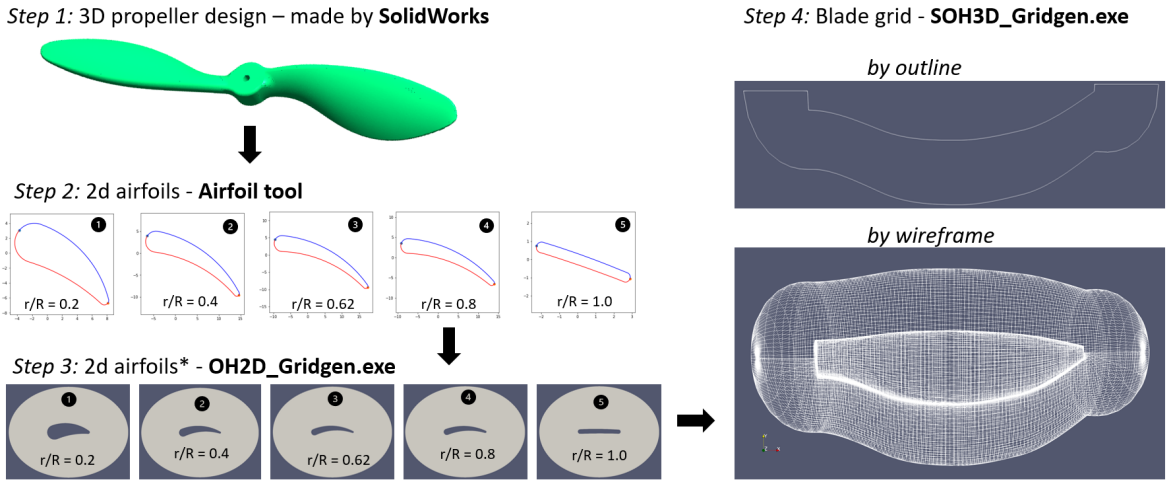

FIGURE 4.11: Process of generating blade grid of *Tombo* propeller by rFlow3D using Airfoil tool as an input processing program, the results of step 3 and step 4 are visualized by Paraview

4.2.3 *TomboGenerator*: A simulation tool for *Tombo* propeller

Section 4.2.1 and section 4.2.2 have shown two approaches to the analysis of the aerodynamics of the *Tombo* propeller. While the first approach can process aerodynamic force fast, the second one takes advantage of accuracy and multi-parameter generation. However, they both required commercial software (such as Matlab, AutoCAD, SolidWorks, rFlow3D, etc.) and several manual steps. With that in mind, based on ***sectionproperties*** [5], a Python open source package, I have developed *TomboGenerator* toward fast and free simulation for *Tombo* propeller. The architecture of *TomboGenerator* has demonstrated in Figure 4.12 while the detail can be found in Figure 4.17. A 3D model of the propeller can be inputted to this software in **S**tandard **T**riangle **L**anguage (STL) or MSH format while the output includes a graph, numerical data, and so on. The main component is the processing core includes three tools: Airfoil Tool, Material Tool, and Aerodynamic Tool.

Airfoil Tool

This tool provides the parameter analysis of any cross-section of a 3D object by giving the point of the cross-section plane and the normal vector. Users can export an

[5] https://sectionproperties.readthedocs.io/en/latest/index.html

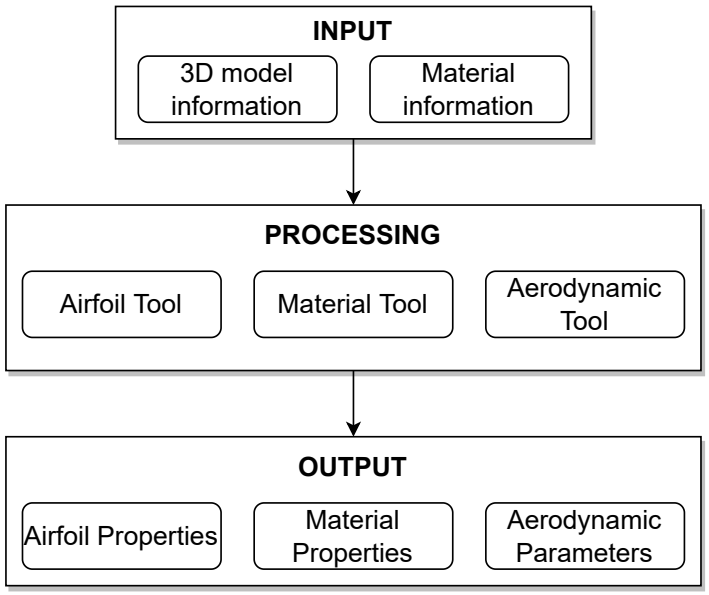

FIGURE 4.12: *TomboGenerator* architecture

STL or MSH file from a 3D object model as input for Airfoil Tool. This tool can:

- Visualize 3D view of an object including Display, Rotate, Zoom (In or Out) functions (see Figure 4.13),
- Calculate the airfoil properties (see Figure 4.14),
- Visualize analyzed section view (see Figure 4.15).

While the 3D visualization functions were built by using *trimesh* package[6], the second latter ones are the development based on the airfoil parameters from [99], [100] and the aerodynamic properties required from the numerical approach in section 4.2.1.

Figure 4.13 show the visualization functions of Airfoil Tool. Users can rotate and zoom in or out for a detailed view of a 3D object. Note that the number of notes and faces of the object model decides the rendering speed of these functions. These numbers can be adjusted toward a better result based on the object's size and shape and the aerodynamic processing accuracy. I recommend GMSH, a three-dimensional finite element mesh generator with built-in pre- and post-processing

[6] https://trimsh.org/trimesh.html

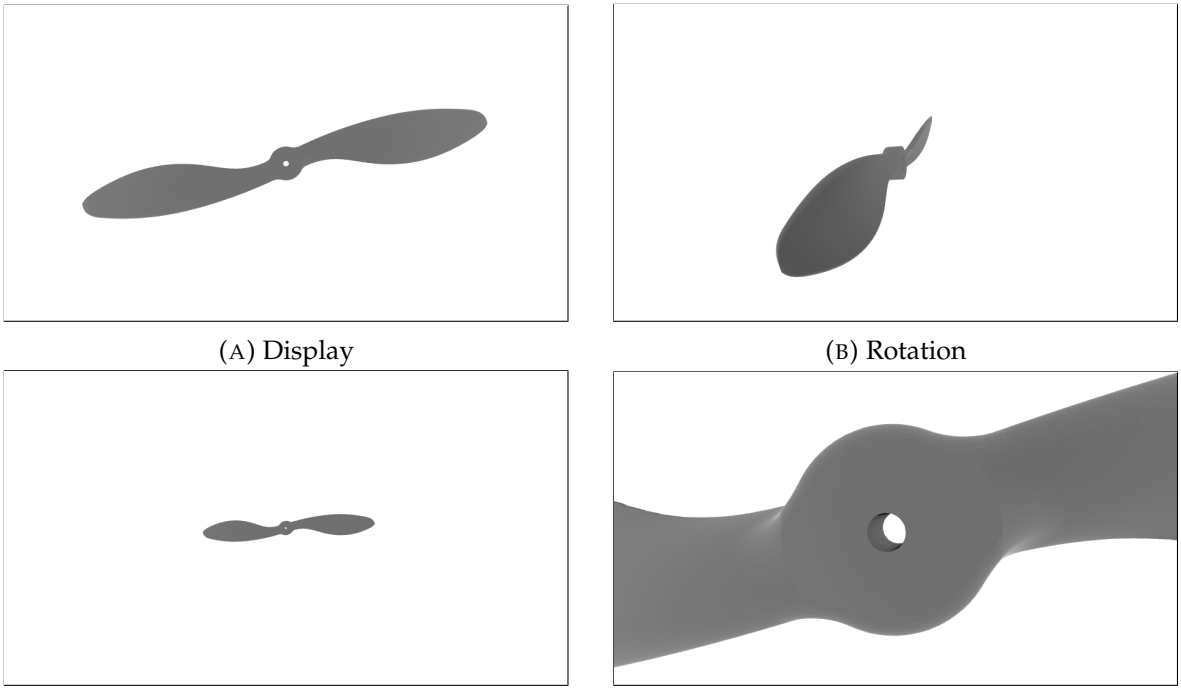

(A) Display (B) Rotation

(C) Zoom out (D) Zoom in

FIGURE 4.13: Airfoil Tool visualization functions:

facilities made by Christophe Geuzaine and Jean-François Remacle, as a 3D model tool for *TomboGenerator* input.

First, an airfoil was created in the format of a point set by the inputted 3D model with the information of cross-sectional plane and normal vector. After that, the airfoil properties were generated from Airfoil Tool (see Figure 4.15). Here, popular cross-sectional parameters (such as area, moments of inertial, and elastic centroid) and typical airfoil properties (such as the position leading edge, trailing edge, chord length, and twist angle) have been defined. Additional parameters such as chordwise position from the leading edge, tension axis from the leading edge, or rotor axis also have been investigated following the NASA document [99], [100] toward the future work of *TomboGenerator*. Next, an arbitrary propeller's cross-section (airfoil) was displayed as Figure 4.14.

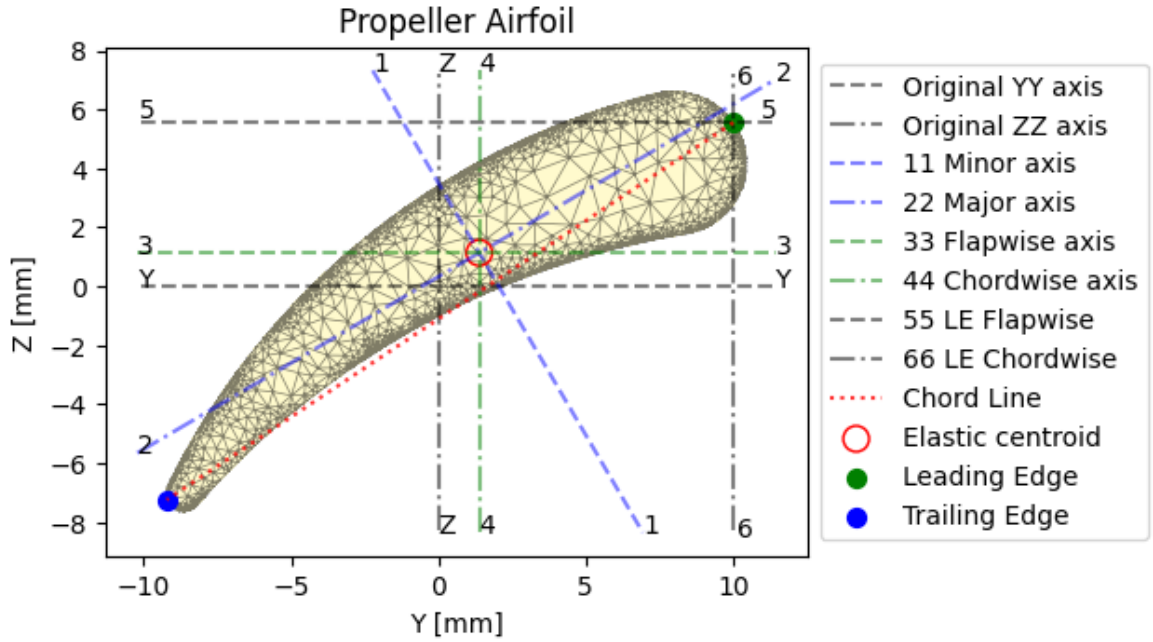

FIGURE 4.14: The cross-section view of *Tombo* propeller at X = 40 mm

Materials Tool

Materials Tool also contributes to the airfoil analysis with several parameters such as section mass and flexural rigidity (see Figure 4.15). These parameters were calculated by combining the geometrical calculating and integrated materials properties. Users can define the materials by the elastic modulus, poison ratio, density, yield strength, and color. *Nodus*, the critical part of the *Tombo* propeller, has a developing function. First, the wing mass and the wing center of pressure were determined. Then the wing centrifugal, bending forces, and twist moment applied on the wing were generated. In the case of composite structure, the elastic modulus and shear modulus of *Nodus* were calculated by Equation 4.3. In addition, it is possible to define *nodus* material if users know the distribution of material components (homogeneous type or mixed materials, for example). That is the future development of Tombo, which will be discussed in Chapter 8.

Aerodynamic Tool

With the insight from the numerical approach in section 4.2.1, this tool firstly calculates the aerodynamic forces of a rigid propeller with the same morphology as the

AIRFOIL PROPERTIES AT X = 40 [mm]

Property	Value	Unit	Expression
Ecw_jx	8.63e-03	m	Chordwise CG position from Leading Edge
Et_jx	8.00e-03	m	Tension axis from Leading Edge
Ee_jx	9.69e-03	m	Elastic axis from Leading Edge
Ra_jx	1.00e-02	m	Rotor axis (Pitching axes)
Ms_jx	8.11e-02	kg/m	Mass distribution (ABS)
kA	6.14e-03	m	Radius of gyration
EIx	7.13e+00	kg.m	Flapwise Flexural rigidity
EIy	3.30e-01	kg.m	Chordwise Flexural rigidity
Ip_jx	3.77e-05	kg.m	Polar mass moment of inertia
EIyy_jx	7.13e+00	N.m^2	Flapwise stiffness
EIzz_jx	3.30e-01	N.m^2	Chordwise bending stiffness
Gj_jx	8.88e-01	N.m^2	Torsional stiffness
Tw_jx	3.36e+01	deg	Twist (r/R = 75%) = 0
A	7.91e-05	m^2	Airfoil area
Ae_T	-2.79e-12	m^3	Tension axis position
I_eta	-1.32e-10	m^4	Inertia about minor principal axis
I_zeta	-2.85e-09	m^4	Inertia about major principal axis
Ak2_A (J)	-2.98e-09	m^4	Torsion constant
B_1	-2.22e-13	m^6	Blade cross-section integral
B_2	5.76e-12	m^5	Blade cross-section integral
m	-8.11e-02	kg/m	Section mass (ABS)
me	-2.86e-09	kg	
mk2_m1	-1.35e-07	kg.m	Flapwise mass moment of inertia distribution
mk2_m2	-2.92e-06	kg.m	Chordwise mass moment of inertia distribution
CL	2.31e-02	m	Chord length

FIGURE 4.15: The airfoil properties of the cross-section at $x = 40\,mm$

Tombo propeller and the wing torque. Then, the deformable angles were introduced as the input for modifying the aerodynamic forces as Equation 4.8. Then a loop was set to find the convergent results. Finally, the output was saved for visualization later.

Additionally, users can visualize the deformation of the *Tombo* propeller versus the rotational speed using the output from *TomboGenerator* (see Figure 4.16). This program did not optimize to integrate to *TomboGenerator*, so it was not demonstrated in Figure 4.17. **PyVista** package[7] was used as the core toolkit for visualization here.

Overall, the detail of *TomboGenerator* architecture has demonstrated in Figure 4.17. This is the very first version of *TomboGenerator* toward a full simulation software for deformable propellers.

[7] https://docs.pyvista.org/

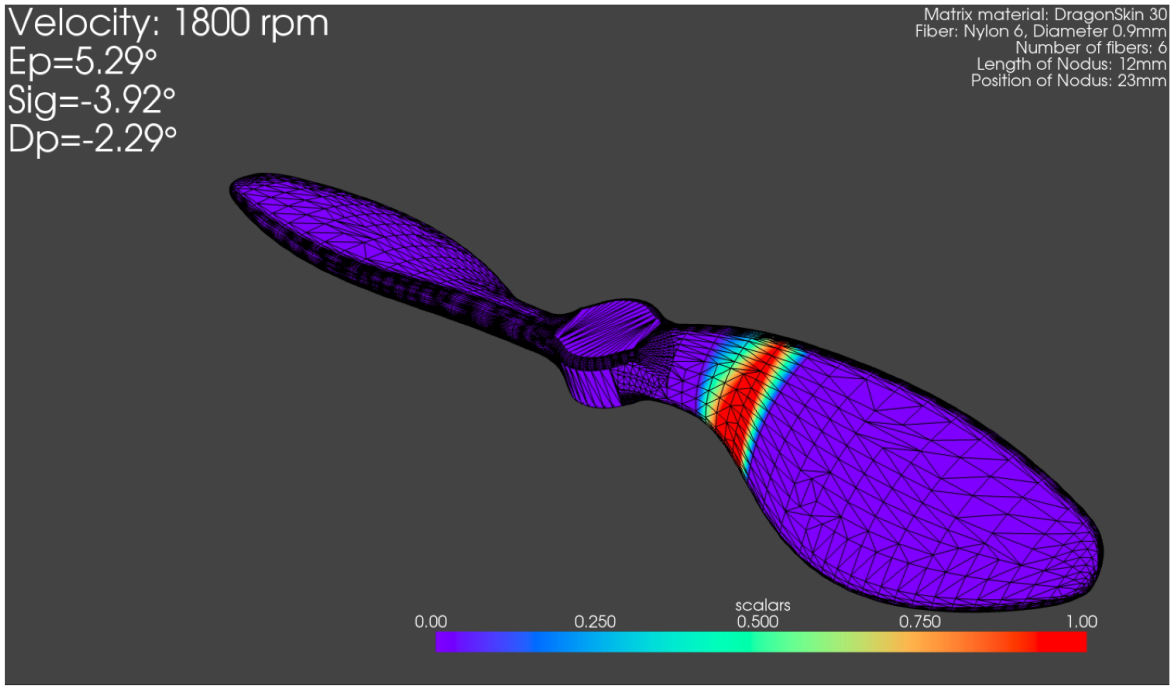

FIGURE 4.16: Visualization of the deformation of *Tombo* propeller with the output gained from *TomboGenerator*

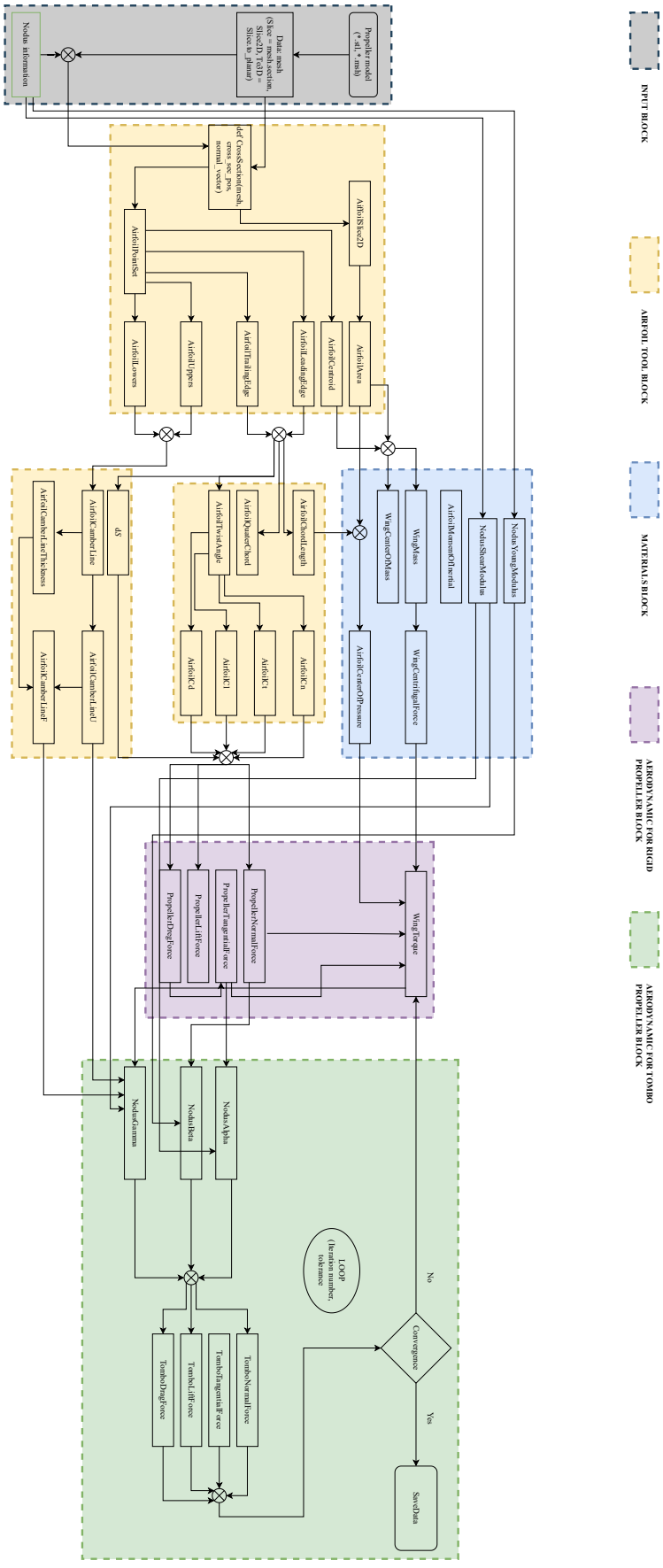

FIGURE 4.17: The detail of *TomboGenerator* architecture

5 Experimental investigation of *Tombo* propeller's characteristics

5.1 Measurement of *Tombo* propeller's characteristics

The purpose of this section is to discuss the results of indoor experiments that were conducted to evaluate the characteristics of Tombo propellers using different combinations of nodus matrix materials and fiber diameters (as detailed in Table 5.1). These experiments were carried out in order to gain a better understanding of the performance of these propellers.

1. To assess the accuracy of the aerodynamic model presented in Chapter 4 through examining the thrust force and deformation angle outcomes,

2. To gain an understanding of its performance such as thrust force, collision force, and noise at different rotational speeds. By observing its characteristics in action, we can build a foundation of knowledge about how it behaves.

The setup used in the experiment consisted of an X2212 960 KV motor connected to a 12 V power source that powered a rotating propeller. The motor was mounted on a force gauge (IMADA ZTS-5N 10Hz, Japan) and placed on an acrylic base plate to protect the conductor and other components (section 5.1.1). A high-speed camera (DSC-RX10M4, Sony, Japan) was utilized to record the recovery time and deformable angle β measurements (sections 5.1.3 and 5.1.4). Lighting and a black background were also utilized to aid in visual detection. The findings from the experiments are discussed in Chapter 8.

TABLE 5.1: *Tombo* propeller configurations used to evaluate the aerodynamic model and observe working characteristics

Name	***Nodus'* configuration**							**Deformable edge materials**	**Size** (inch)
	Matrix material	**Fiber material**	**Number of fibers**	**Diameter of fiber** (mm)	**Length** (mm)	**Young's modulus** E_N (MPa)	**Shear modulus** G_N (MPa)		
Conf. 0	-	-	-	-	-	-	-	-	9
Conf. 1	DragonSkin 10	Nylon 6	6	0.94	12	0.1542	0.0551	-	9
Conf. 2	DragonSkin 20	Nylon 6	6	0.94	12	0.5705	0.2036	-	9
Conf. 3	DragonSkin 30	Nylon 6	6	0.94	12	0.7873	0.2809	-	9
Conf. 4	DragonSkin 30	Nylon 6	6	0.38	12	0.6557	0.2341	-	9
Conf. 5	DragonSkin 10	Nylon 6	5	0.5	12	0.1315	0.0469	DragonSkin 10	9
Conf. 6	DragonSkin 10	Nylon 6	5	0.75	12	0.1413	0.0505	DragonSkin 10	9
Conf. 7	DragonSkin 10	Nylon 6	5	0.9	12	0.148	0.0528	DragonSkin 10	9
Conf. 8	DragonSkin 20	Nylon 6	5	0.5	12	0.4862	0.1736	DragonSkin 20	9
Conf. 9	DragonSkin 20	Nylon 6	5	0.75	12	0.5227	0.1866	DragonSkin 20	9
Conf. 10	DragonSkin 20	Nylon 6	5	0.9	12	0.5473	0.1954	DragonSkin 20	9
Conf. 11	DragonSkin 30	Nylon 6	5	0.5	12	0.671	0.2396	DragonSkin 30	9
Conf. 12	DragonSkin 30	Nylon 6	5	0.75	12	0.7213	0.2574	DragonSkin 30	9
Conf. 13	DragonSkin 30	Nylon 6	5	0.9	12	0.7552	0.2695	DragonSkin 30	9

5.1.1 Thrust force measurement experiments

For this experiment, I examined how the thrust force of the Tombo propeller changed with rotational speed in 13 different configurations. The measurements were taken at rotational speeds from 2000 to 3200 rpm. The experiment took place indoors and the motor's axis was positioned vertically in relation to the ground (as shown in Figure 5.1). The results are presented in Table 5.1. The measurement sampling rate was 10 Hz, and 200 samples were collected to calculate a thrust force and the mean square error of it (the thrust force deviation).

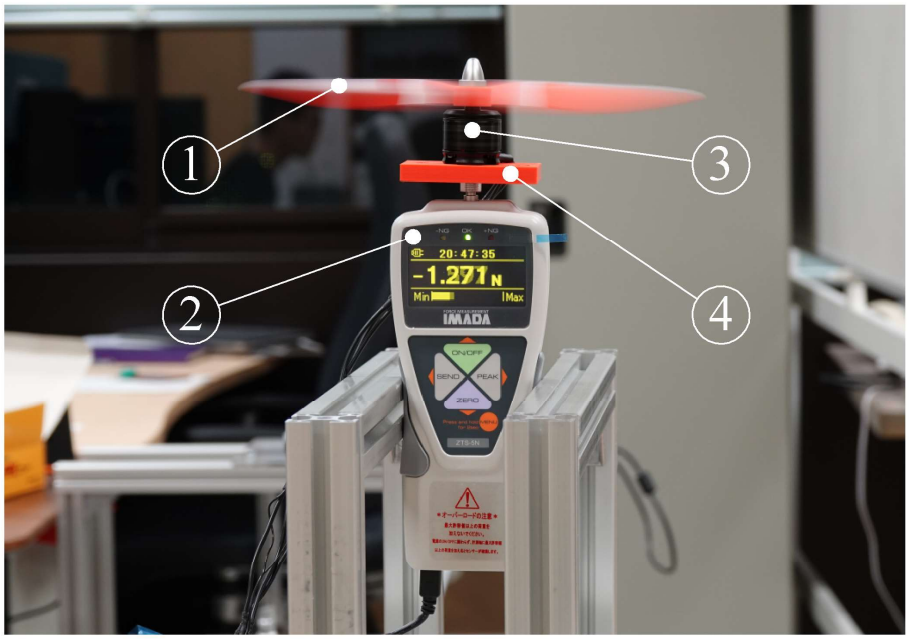

FIGURE 5.1: The experiment setup for thrust force measurement experiments: 1 - *Tombo* propeller, 2 - IMADA force gauge ZTS-5N, 3 - Brushless motor X2212 960 KV, 4 - Motor base

5.1.2 Deformable angle β measurement experiments

A high-speed camera with a 960 fps capability was used for this measurement. It was positioned perpendicular to the plane of the rotor and aligned with the rotor's axis, as depicted in Figure 5.2.

To begin, I increased the speed of the rotor to a specific rotation speed and then started recording while reducing the rotor speed to 0 rpm. The video that was

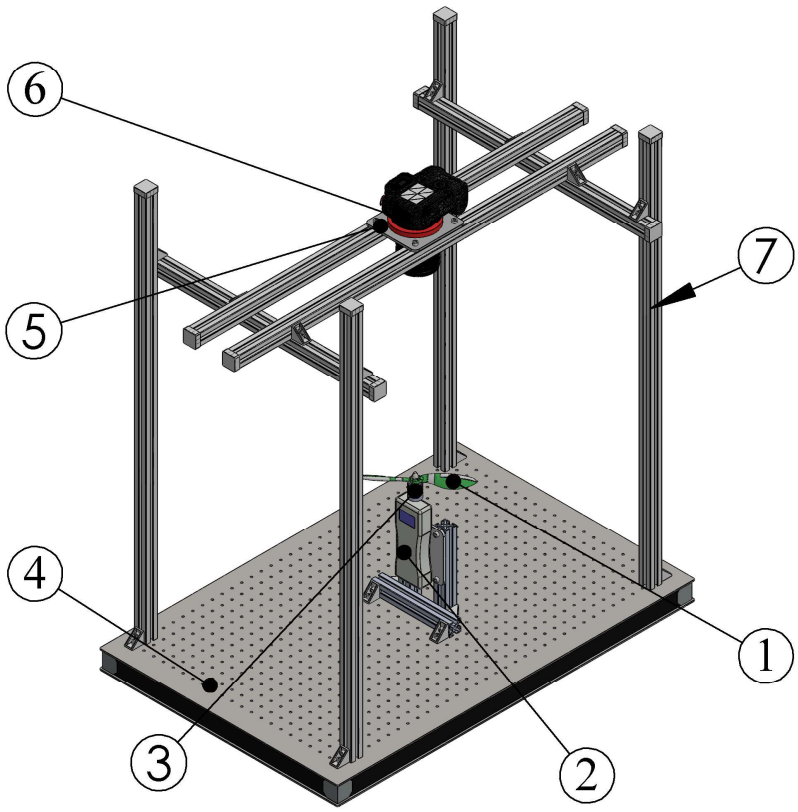

FIGURE 5.2: The experiment setup for deformable angle β measurement experiments: 1 - *Tombo* propeller, 2 - IMADA force gauge ZTS-5N, 3 - Brushless motor X2212 960 KV, 4 - Motor base,

recorded was then processed using OpenCV in Python, resulting in a series of still image frames that appeared blurry (as shown in Figure 5.3a). I then used a normalized 10-continuous-frame combo to determine the rotational speed of the *Tombo* propeller in each image frame and the corresponding propeller diameter (as shown in Figure 5.3b). In order to determine the propeller diameter at each combo, I needed to focus on the center of its rotation (as shown in Figure 5.3c). Initially, I attempted to use the OpenCV function for center detection, but the generated coordinates had to be integers and the results were poor (as shown in Figure 5.3d). To improve the accuracy, I transformed the coordinates of each pixel to the real field (as shown in Figure 5.3e) and then utilized a RANdom-SAmple Consensus (RANSAC) [101] algorithm to determine the appropriate center of a point cloud (as shown in Figure 5.3f). This allowed me to define the diameter of a 10-continuous-frame combo using

Hull's contour (as shown in Figure 5.3g). Finally, I was able to calculate the deformable angle β based on the change in diameter and the position of the nodus (as shown in Figure β). It is important to note that I excluded recorded image perspective distortions caused by the change of propeller tip in the vertical direction due to the small increment of the camera angle of view δ_ψ (which was less than 1.2 %).

5.1.3 Time recovery measurement experiments

The purpose of this experiment was to measure the time it takes for a *Tombo* propeller to recover after a collision. To do this, a silicone rubber (Dragon Skin 30) model finger with a nylon core was used, along with a high-speed camera to record the collision and recovery process (both in terms of rotational speed and thrust) (see Figure 5.4). The model finger was inserted manually above the propeller and collided randomly with it. The recovery time for the propeller was determined by measuring thrust force with both a force sensor and the camera, while rotational speed was determined from video data. The experiment was performed three times for each propeller, and the longest recovery time from a single collision was recorded. There were instances where the propeller hit the finger multiple times.

5.1.4 Collision force measurement experiments

To ensure accurate measurement, the direction of the collision force must be aligned with the axis of the force gauge. The ZTS-500 force gauge, equipped with a wide range of measurement (up to 500 N) and a tube of 3 cm diameter and 150 cm length, was positioned perpendicular to the plane of the motor (as shown in Figure 5.4). The process of measuring the collision force involved dropping an obstacle freely within the guide tube from the top end so that it would collide with the propeller at a specific location, and the force gauge would record the collision force.

In this experiment, two parts were conducted. The first part involved identifying the most hazardous crash zone on the propeller blade by striking an object at different distances from the center of the propeller, such as 50, 60, 70, 80, 90, and

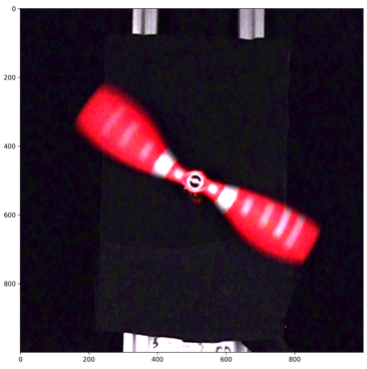

(A) Images (blurred) were recorded of the high-speed rotating propeller

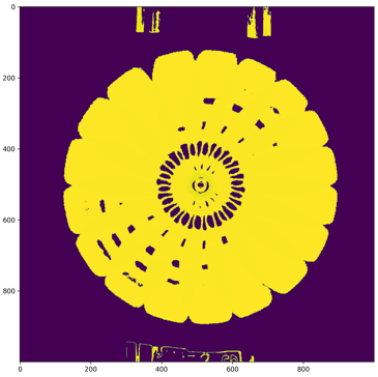

(B) A 10-continuous-frame combo was used for speed normalization

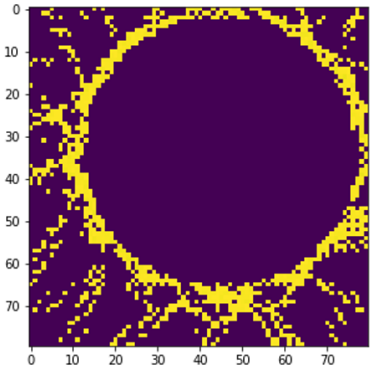

(C) The 10-frame combo image has a graph of pixels at its center

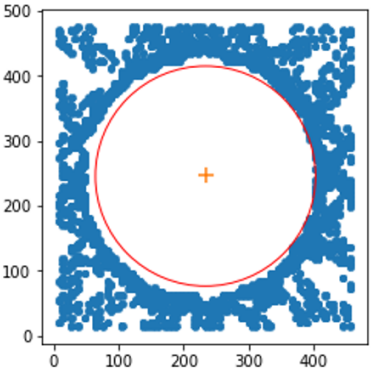

(D) The Open CV function experienced a problem in identifying the rotational center

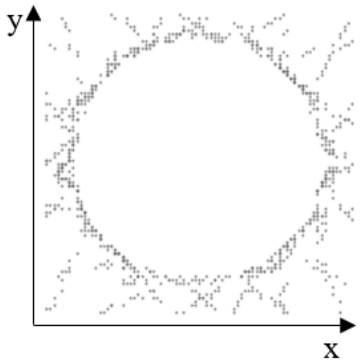

(E) In the transition from image processing to numerical processing, the pixel image is represented by a real number graph

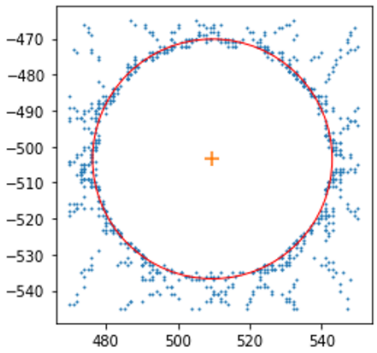

(F) The outcome of the detection of a rotational center using a function that utilizes the RANdom SAmple Consensus (RANSAC) algorithm has been determined

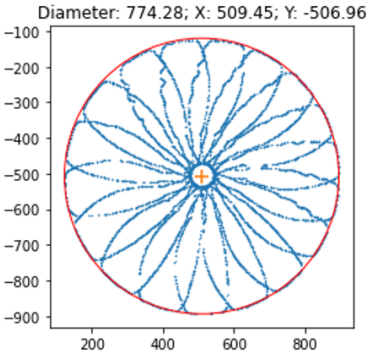

(G) The convex Hull allows quick determination and visualization of the propeller diameter

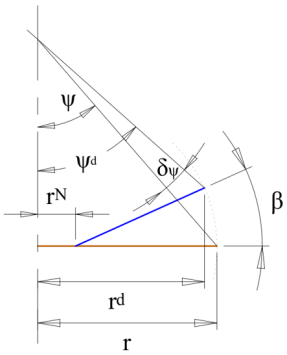

$$\beta = acos(\frac{r^d - r^N}{r - r^N})$$

(H) The deformable angle to be altered based on a change in the diameter of a propeller

FIGURE 5.3: Method of deformation angle β detection: $\beta = acos(\frac{r^d - r^N}{r - r^N})$ where the original radius of a Tombo propeller is denoted as r^d. If the propeller is deformed, its radius is represented by r^d. The distance from the center of the propeller to the beginning of the nodus is referred to as r^d. The camera view angles in the resting state of the propeller are designated as ψ, and when it is in a deformable state, the camera view angles are referred to as ψ^d. The difference between the two camera view angles is represented by δ_ψ, which is calculated as the change in the angle from the deformable state to the resting state

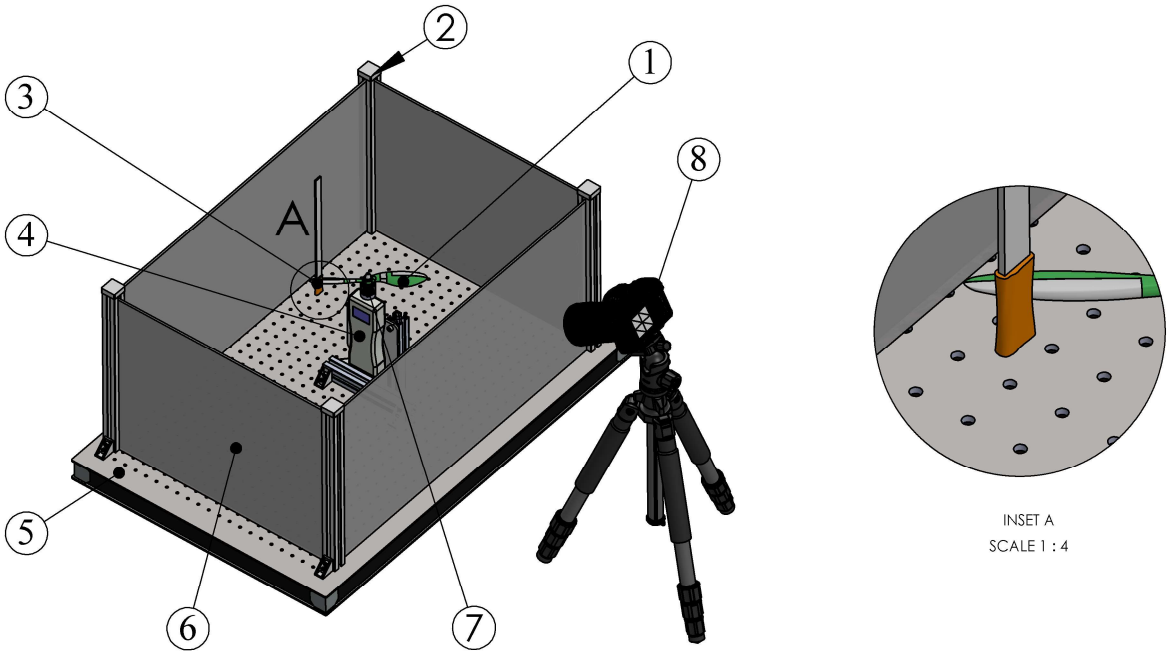

FIGURE 5.4: An experiment was conducted to measure the time needed for recovery in a particular scenario, as depicted in Inset A of the setup. This scenario involved a propeller colliding with a simulated human finger

TABLE 5.2: Collision force and thickness of collided blade of a *Tombo* propeller Conf. 13 at 2500 rpm

Collision area	**I**	**II**	**III**	**IV**	**V**	**VI**
Distance to the hub center (mm)	50	60	70	80	90	100
Maximum collision force (N)	206.5	337.2	331.2	244.4	225.3	136.3
Thickness of the blade (mm)	6.2	6.2	6.0	5.3	3.7	2.8
Force per thickness (N/mm)	33.2	54.4	55.2	45.8	61.4	49.1

100 mm. The position at 90 mm from the center was determined to be the most dangerous based on the highest critical force per thickness recorded (61.4 N/mm). For the second part of the experiment, the collision force was measured for a range of Tombo propeller configurations, ranging from Conf. 5 to Conf. 13 (see Table 5.1). The results of these tests are presented in Table 5.3.

5.1.5 Noise measurement experiments

For this experiment, I used a Meter MK09 Sound Lever Meter to measure the noise levels of single propellers at various distances, including 1, 2, 3, 4, and 5 m. Both a rigid propeller and Tombo propellers were used and the configurations for these are

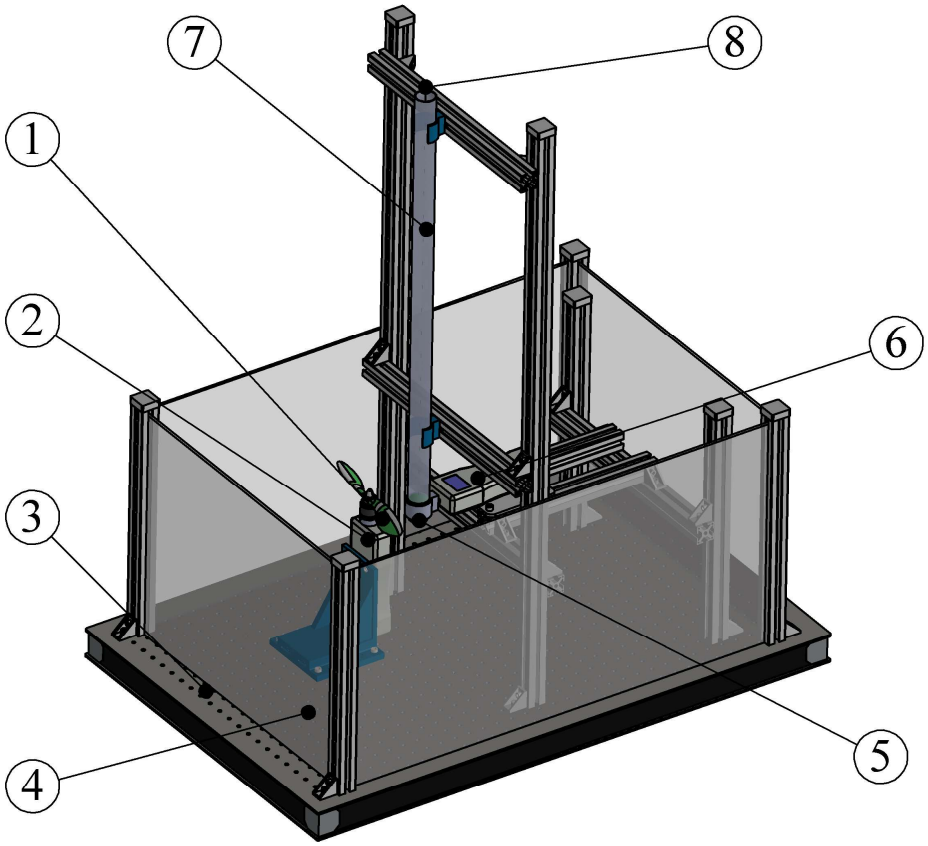

FIGURE 5.5: The experiment setup for collision force measurement experiments: 1 - *Tombo* propeller, 2 - IMADA force gauge ZTS-5N, 3 - Optical breadboard, 4 - Acrylic plate, 5 - Collided object, 6 - IMADA force gauge ZTS-500N, 7 - Guide tube, 8 - Rope

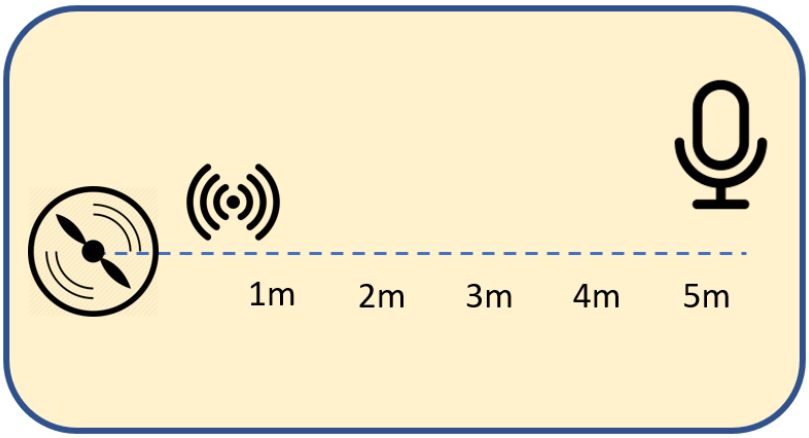

(A) Schematic of noise measurement method

(B) Noise measurement required devices

FIGURE 5.6: Noise measurement method and requirement devices: : 1 - Transmitter for rotational speed control, 2 - Handheld Meter MK09 Sound Lever Meter

detailed in Table 5.1. Finally, a drone noise test was conducted with two objectives: the former with a set of standard propellers and the latter equipped by a set of *Tombo* propellers at the distance of 2 m. Overall, the result indicates that the noise of a *Tombo* propeller and a *Tombo* drone are almost the same as that of the standard ones.

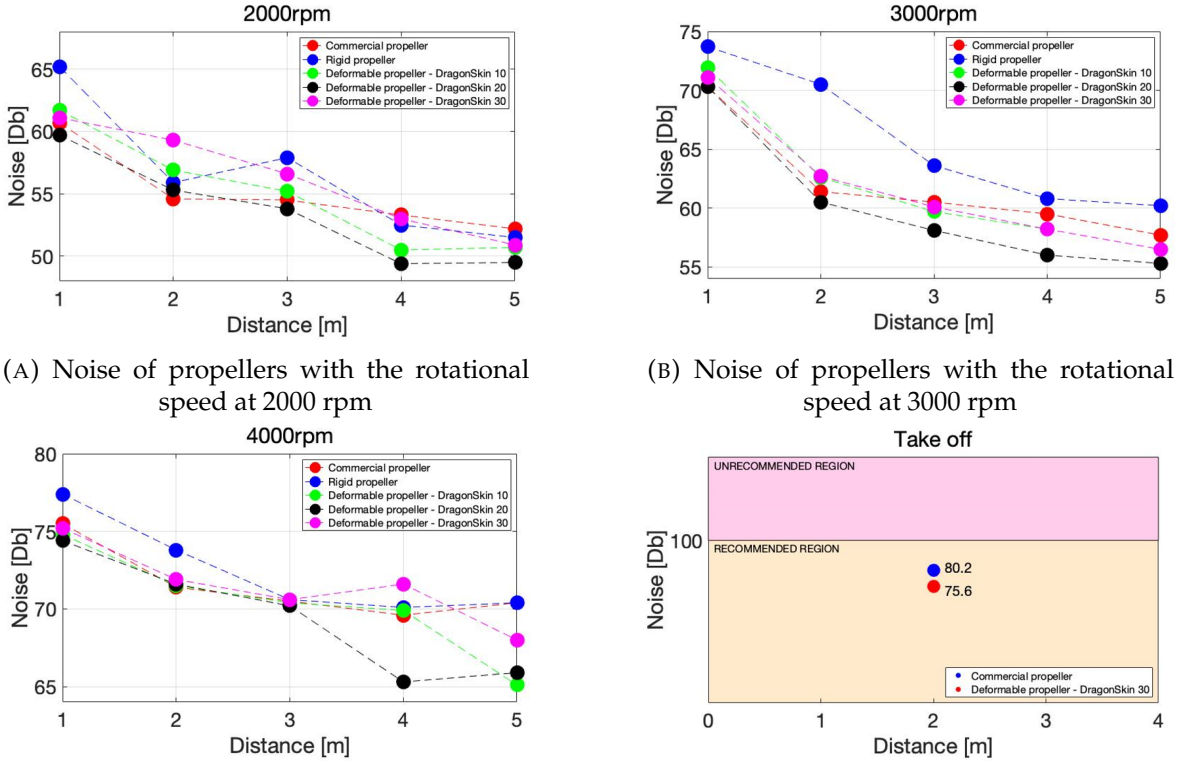

(A) Noise of propellers with the rotational speed at 2000 rpm

(B) Noise of propellers with the rotational speed at 3000 rpm

(C) Noise of propellers with the rotational speed at 4000 rpm

(D) Noise of drone at the take off state

FIGURE 5.7: Noise measurement results

5.2 Aerodynamic model of the *Tombo* propeller

5.2.1 *Nodus'* parameters

The mechanical and geometrical features of the *nodus* are crucial in constructing a propeller model that is aerodynamically efficient. It is important to consider the following parameters when using the *nodus* model outlined in section 4.1.3: the length of the *nodus*, details about the representative cross-section, the number of fibers, the diameter of the fibers (as determined by the design), the Young modulus and

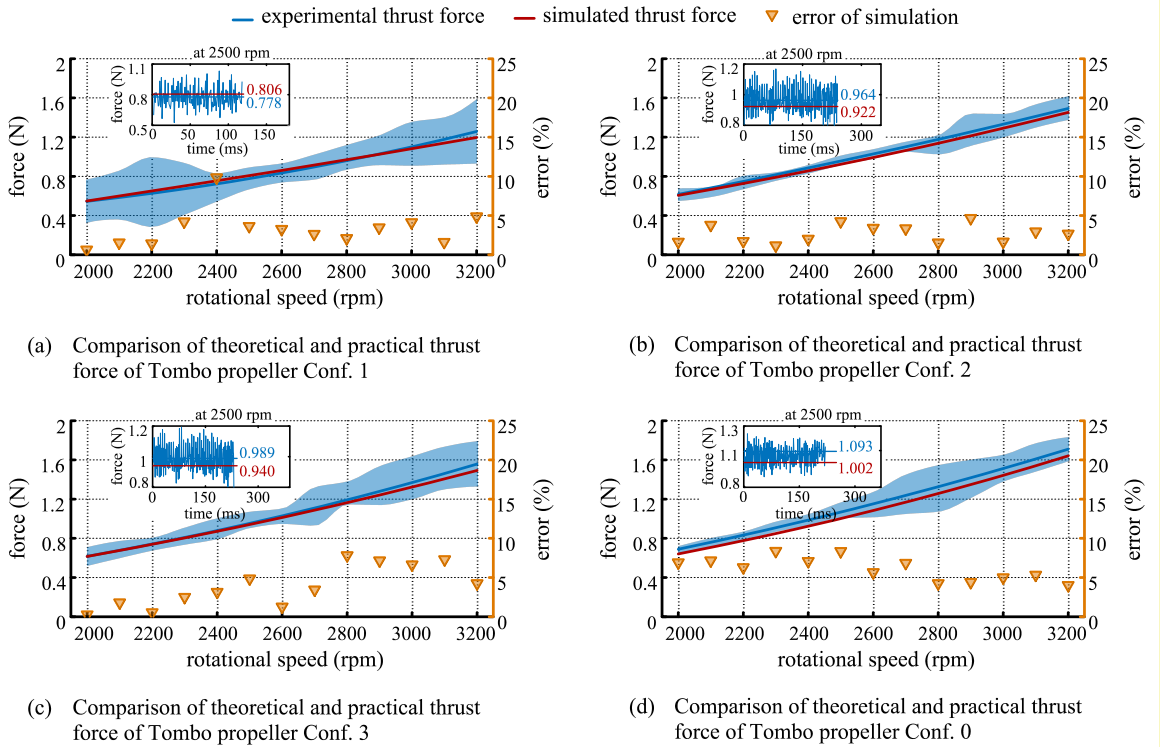

(a) Comparison of theoretical and practical thrust force of Tombo propeller Conf. 1

(b) Comparison of theoretical and practical thrust force of Tombo propeller Conf. 2

(c) Comparison of theoretical and practical thrust force of Tombo propeller Conf. 3

(d) Comparison of theoretical and practical thrust force of Tombo propeller Conf. 0

FIGURE 5.8: Comparison of thrust and collision response among *Tombo* propellers with different nodus configurations. Experiments were conducted with three configurations of the *Tombo* propeller (Conf. 1, Conf. 2, and Conf. 3), and a rigid propeller (Conf. 0) in the speed range 2000 rpm to 3200 rpm. The red line plots the estimated thrust force (EsT), the blue line depicts the experimental thrust force (ExT), and the yellow triangles indicate the error of simulation (EoS). The subgraphs (in boxes within graphs a, b, c, and d) show EsT and ExT of the propeller operating at a speed of 2500 rpm. (a) Conf. 1. (b) Conf. 2. (c) Conf. 3. (d) Conf. 0.

shear modulus of the matrix material and fibers (as determined by experiments using American Society for Testing and Materials Standard ASTM 412 Die D dumbbell specimens and a Poisson ratio of 0.4). The Young and shear modulus of the *nodus* were then calculated using Equation 4.3 and recorded in Table 5.1. The results show that the mechanical properties of the matrix are the most important factor in determining Young's modulus and shear modulus of the *nodus*. Additionally, increasing the number and diameter of the fibers increases these moduli.

5.2.2 Aerodynamic model of the *Tombo* propeller

Several experiments were conducted to compare the estimated and experimental aerodynamic parameters of *Tombo* propellers with different configurations (shown

in Table 5.1). As shown in Figure 5.8, the model demonstrated good thrust prediction when the estimation error was below 8 % for various levels of nodus stiffness. Additionally, as the nodus stiffness increased, the magnitude and stability of lift force at the same speed also increased. The experimental and simulated thrust forces demonstrated linear characteristics within the rotational speed range of 2000-3200 rpm. Still, the simulated results over a broader range (up to 8000 rpm) showed more clearly the nonlinear characteristics (as seen in Figure 5.9). Furthermore, Figure 5.8 indicates that a propeller with lower stiffness may lead to more significant vibrations (thrust deviation) than the others. Therefore, it is suggested that *Tombo* propellers be checked for stiffness changes in the nodus after extended use to determine if they need to be replaced.

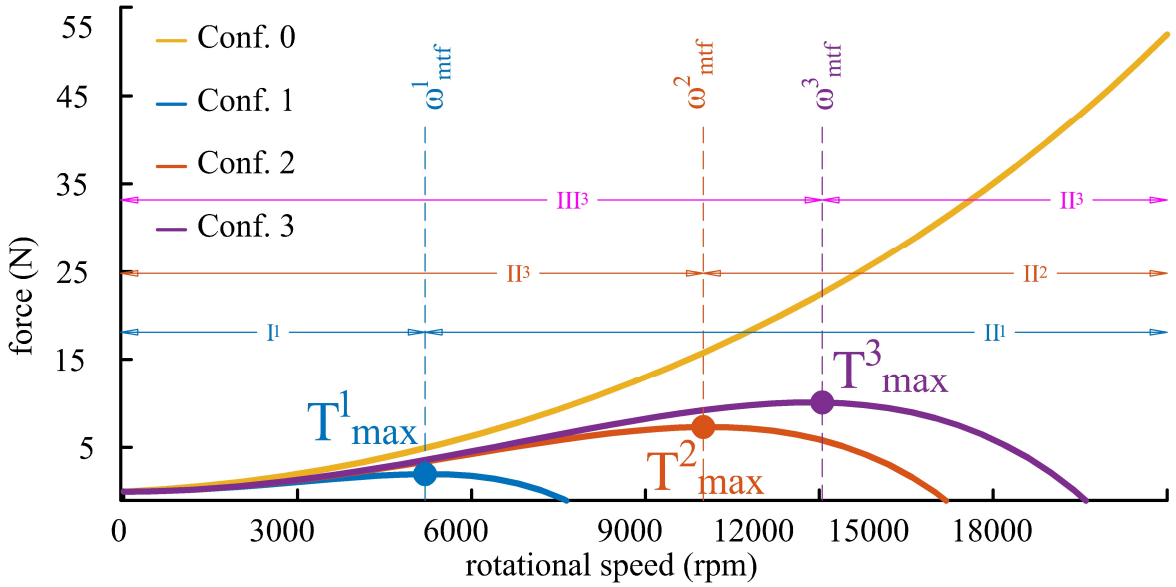

FIGURE 5.9: The thrust forces acting on four different configurations of propellers were investigated over a range of rotational speeds up to 18,000 rpm in order to determine the distribution of these forces. The maximum thrust force for each configuration (designated as Conf. 1, Conf. 2, and Conf. 3) occurred at the respective rotational speeds of ω_1, ω_2, and ω_3.

This model allows for the simulation of the aerodynamic characteristics of the *Tombo* propeller over a wider range of rotational speeds. As shown in Figure 5.9, both experimental and simulated results demonstrate that as the rotational speed increases, the thrust force of the *Tombo* propeller remains proportional to the stiffness of the nodus. However, at higher speeds, there is a notable difference between

the rigid propeller and the *Tombo* propeller. Specifically, the *Tombo* propeller experiences a maximum thrust force, known as T_{max}, at a rotational speed of ω_{mtf} (referred to as the maximum thrust speed) in a steady force state. As the rotational speed increases, the deformable angle γ increases in phases I^1, I^2, and I^3 of Conf. 1, Conf. 2, and Conf 3, respectively (as shown in Figure 5.9). This leads to a decrease in the lift coefficient (C_l). Initially, the ratio between the effect of the rotational speed increase and the decrease in C_l is greater than one, causing the thrust force to continue increasing. At ω_{mtf}, this ratio becomes equal to one, resulting in the maximum thrust force of Tmax. The critical thrust value heavily depends on the nodus stiffness, with a stiffer nodus resulting in a higher critical thrust force. In the subsequent phases III^1, II^2, and II^3 of Conf. 1, Conf. 2, and Conf 3, respectively, when the rotational speed exceeds ω_{mtf}, the aforementioned ratio is less than one, leading to a significant decrease in thrust force. This finding suggests that ω_{mtf} is a suitable choice for unmanned aerial vehicles that need to carry heavy loads or require high acceleration.

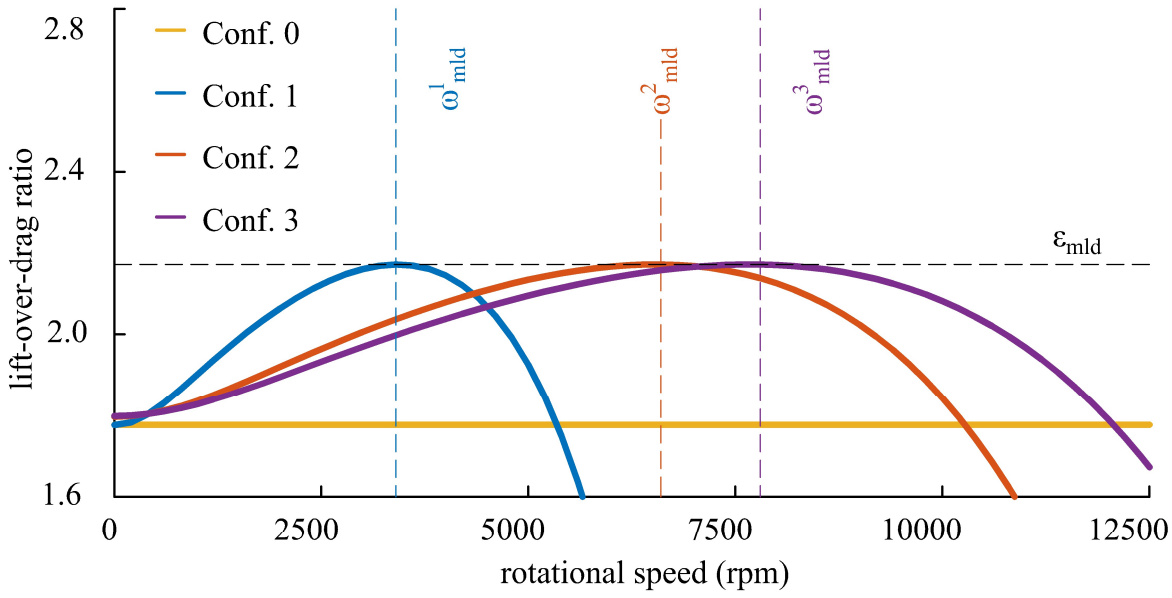

FIGURE 5.10: Simulation was conducted to determine the *lift-to-drag ratio* of three different Tombo propellers (Conf. 1, Conf. 2, and Conf. 3) at various rotor speeds. The results showed that the maximum *lift-to-drag ratio* (ε_{mld}) was achieved at specific rotational speeds (ω^1_{mld}, ω^2_{mld}, and ω^3_{mld}) for each propeller, with a value of 2.17.

Figure 5.10 illustrates the connection between the lift-to-drag ratio (ε_{lod}) and the

rotational speed of the Tombo propeller. This relationship was simulated using equations refeq: 1 and refeq: 1, with ε_{lod} equal to the ratio of the lift force (F_l) to the drag force (F_d). Rigid propellers typically have a constant ε_{lod} value regardless of rotational speed because their geometry does not change during rotation. However, the Tombo propeller exhibits a ε_{lod} that varies with rotational speed. Each Tombo propeller has a critical rotational speed (ω_{mld}) at which the ε_{lod} reaches its maximum value (denoted as ε_{mld}). This maximum value is the same for all Tombo propeller configurations, as they all have the same initial geometric design. When these configurations are deformed, they interfere with the state that produces the highest ε_{lod} value, regardless of the specific configuration. The critical lift-to-drag velocity (ω_{mld}) can vary between Tombo propellers and tends to increase with nodus stiffness. Therefore, selecting an appropriate ω_{mld} can enable the efficient operation of UAVs for tasks such as travel or delivery.

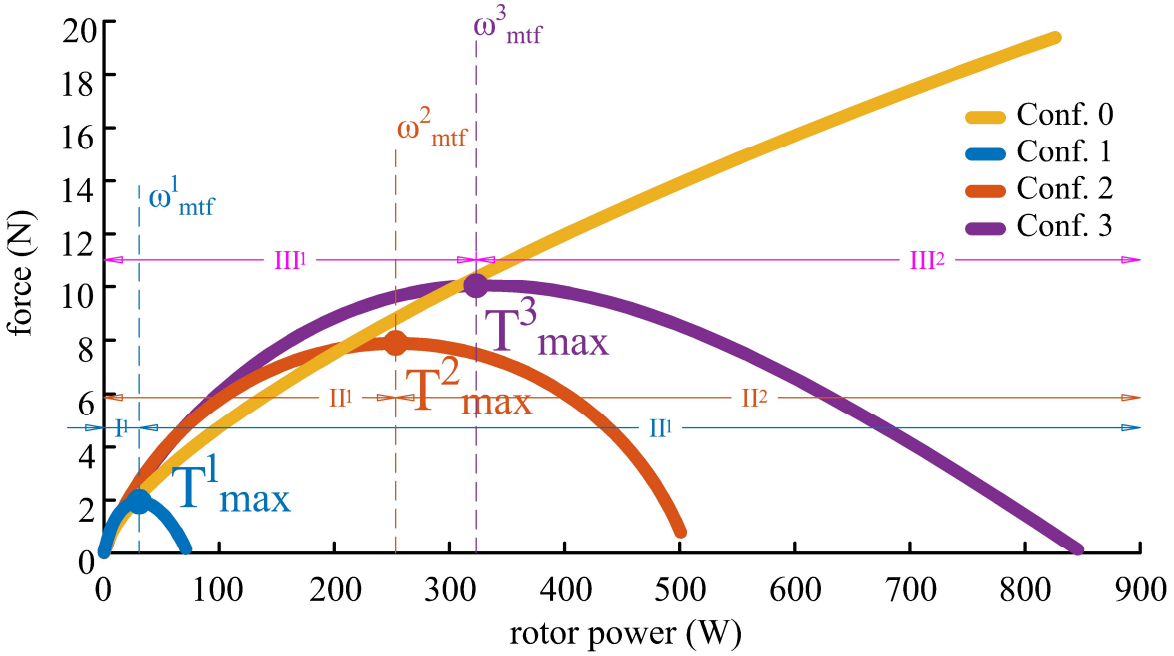

FIGURE 5.11: Simulated lift forces of propellers Conf. 0, Conf. 1, Conf. 2, and Conf. 3 versus rotor power

Figure 5.11 shows the simulated lift forces of several propellers versus rotor power that share the same details as Figure 5.9 such as the phases of recommendation or the *maximum thrust speed* ω_{mtf}. Moreover, this Figure compares the thrust

force of different propellers generated at a rotor power value. In other words, users can choose the suitable rotor power to deal with the weight of the designed drone.

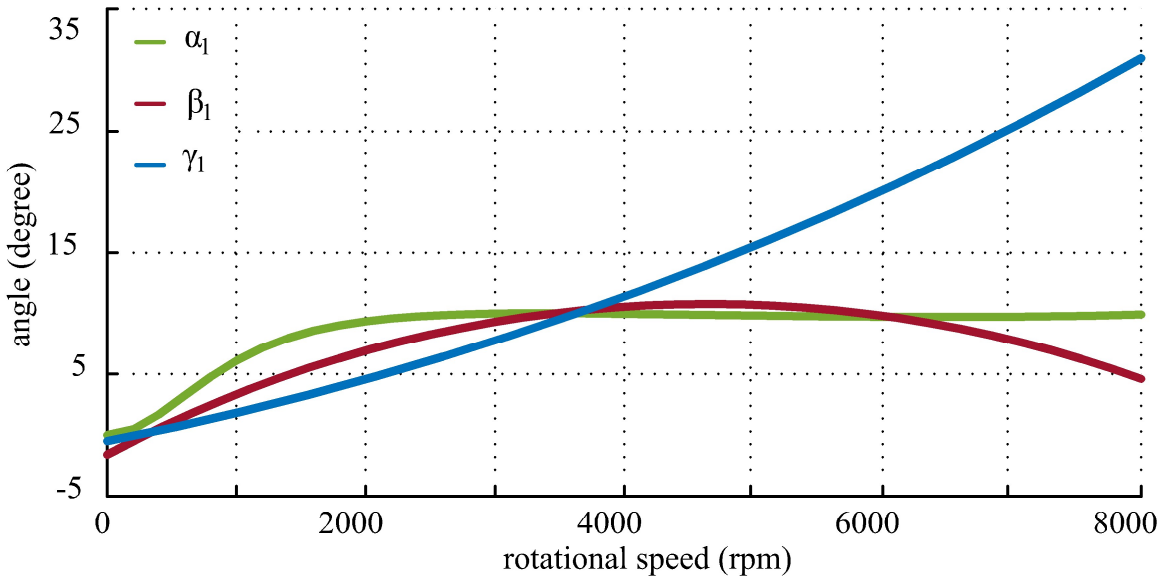

FIGURE 5.12: Simulated deformable angle of Conf. 1 versus rotational speed of rotor

The Tombo propeller's deformable angles can be predicted using Equations 4.4 and 4.5. As seen in Figure 5.12, the angles alpha and beta increase rapidly and reach a stable value of approximately 10 degrees when the propeller's rotational speed is between 2000 to 5000 rpm. γ, on the other hand, continues to increase rapidly without reaching a plateau. This trend, combined with Equation 4.10 and the information presented in Figure 5.9, demonstrates the significant impact that gamma has on the propeller's thrust force. To validate the simulated deformable angles, an experiment was conducted using a Conf. 4 Tombo propeller (shown in Figure 5.13). The results showed that the simulated value for angle beta was similar to the experimental value at rotational speeds above 2000 rpm. However, at lower speeds, the observed angle displayed a larger deviation due to limitations in the experimental model (described in Section 5.1.2). When the motor's speed was rapidly decreased, the inertia force caused the blade to flutter at a rotational speed close to zero, resulting in a significant change in the deformable angle.

To investigate the contribution of γ to the aerodynamics of the Tombo propeller, I simulated this angle as shown in Figure 5.14. Despite different configurations, *Tombo*

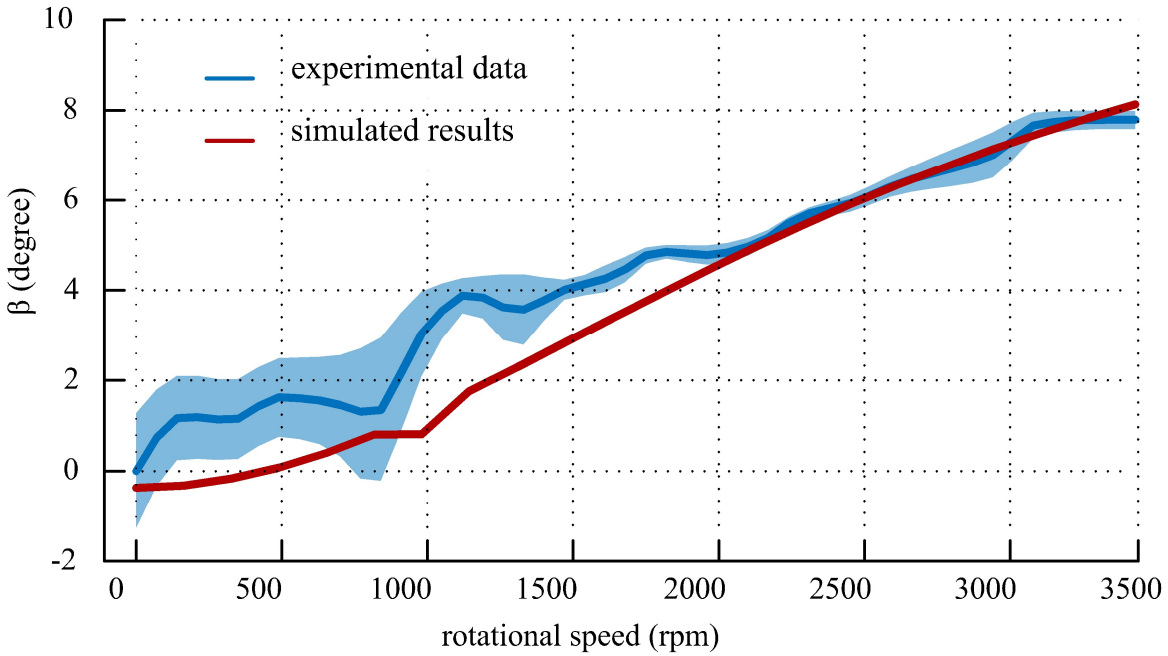

FIGURE 5.13: Comparison of theoretical and practical deformable angle β

propellers that share the same original design will reach critical thrust and critical lift-to-drag ratio states at the same γ_{mld} and γ_{mtf}. This finding strongly confirms that γ plays a decisive role in the deformable states of the *Tombo* propeller.

5.3 Characteristics of *Tombo* propeller with different configurations

The *Tombo* propeller is a deformable propeller designed specifically for use on unmanned aerial vehicles (UAVs). It is designed to improve safety and therefore, it was necessary to study its characteristics in order to understand and confirm its beneficial features. Nine different configurations of the *Tombo* propeller and one rigid propeller were analyzed, focusing on six characteristics including thrust force, deviation in thrust force, collision force, recovery time, simulated lift-to-drag (L/D) ratio, and noise (Table 5.3). All of the experiments were conducted at a propeller rotation speed of 2000 rpm, and the results were normalized based on those of the rigid propeller in order to compare them visually in Figure 5.15.

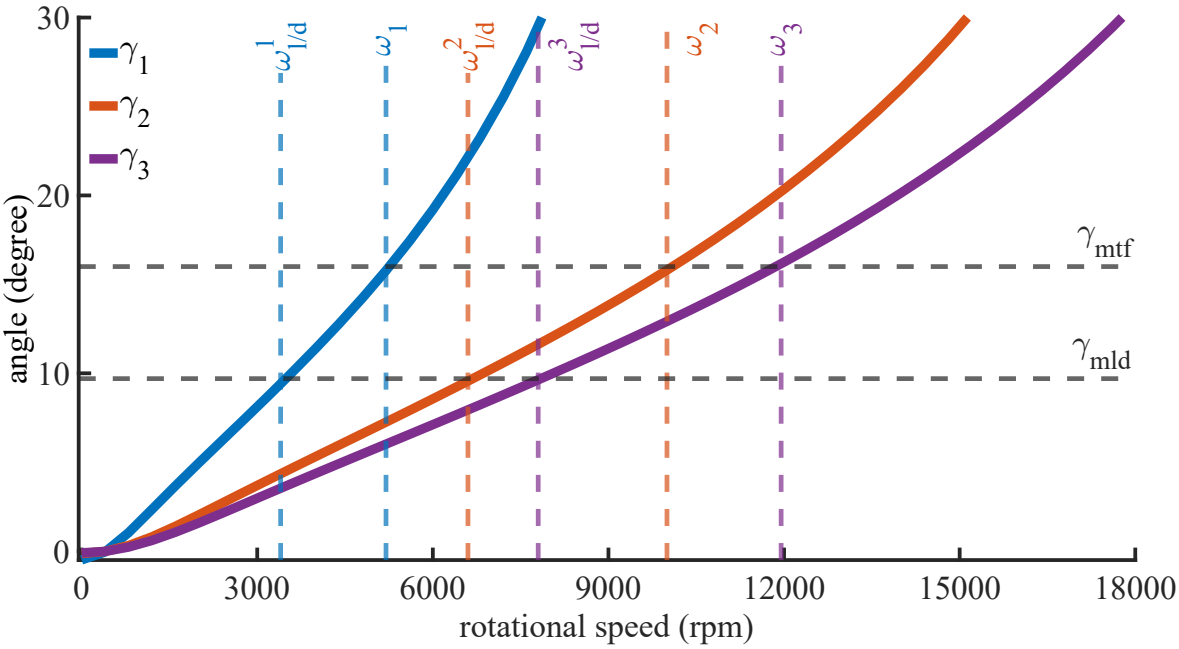

FIGURE 5.14: In Conf. 1, Conf. 2, and Conf. 3, the twist angle γ had the same value of γ_{mtf} and γ_{mld} in both situations where the maximum thrust force and the maximum lift-to-drag ratio were achieved.

In summary, the *Tombo* deformable propeller appears to have some advantages over a traditional rigid propeller. Both the *Tombo* and rigid propellers had similar levels of thrust force, thrust force deviation, simulated L/D ratio, and noise (0.621 N, 0.098 N, 1.9663, and 50 dB, respectively vs 0.658 N, 0.11 N, 1.776, and 49.4 dB, in turn). However, the *Tombo* propeller had a lower mean of thrust force deviation and a smaller collision force, which could potentially lead to less risk of injury or damage in the event of a collision. Additionally, the thrust force deviation of the *Tombo* propeller was more variable, with a range of 0.03 to 0.26 N across different configurations. In practical use, this deviation is important for maintaining balance in a drone, so the specific configuration should be taken into consideration when selecting a propeller.

TABLE 5.3: Characteristics of *Tombo* propellers and a rigid propeller measured at 2000 rpm of rotational speed

	Thrust force [N]	**Thrust force deviation [N]**	**Collision force [N]**	**Recovery time [s]**	**Simulated L/D ratio**	**Noise (distance: 5m) [dB]**
Conf. 0	0.658	0.11	269.3	0.3	1.776	49.4
Conf. 5	0.656	0.03	147.3	0.63	2.0822	49.1
Conf. 6	0.537	0.14	93.7	0.55	2.0718	51
Conf. 7	0.631	0.04	81.5	0.32	2.0652	49.6
Conf. 8	0.589	0.09	80.4	0.32	1.9323	48.7
Conf. 9	0.622	0.07	159.6	0.3	1.9251	49.2
Conf. 10	0.656	0.12	123.7	0.66	1.9206	50.2
Conf. 11	0.666	0.07	123	0.39	1.9051	49.5
Conf. 12	0.624	0.26	189.9	0.55	1.899	52.4
Conf. 13	0.611	0.06	145.5	0.42	1.8952	50.7
Mean	0.621	0.098	127.2	0.46	1.9663	50.0

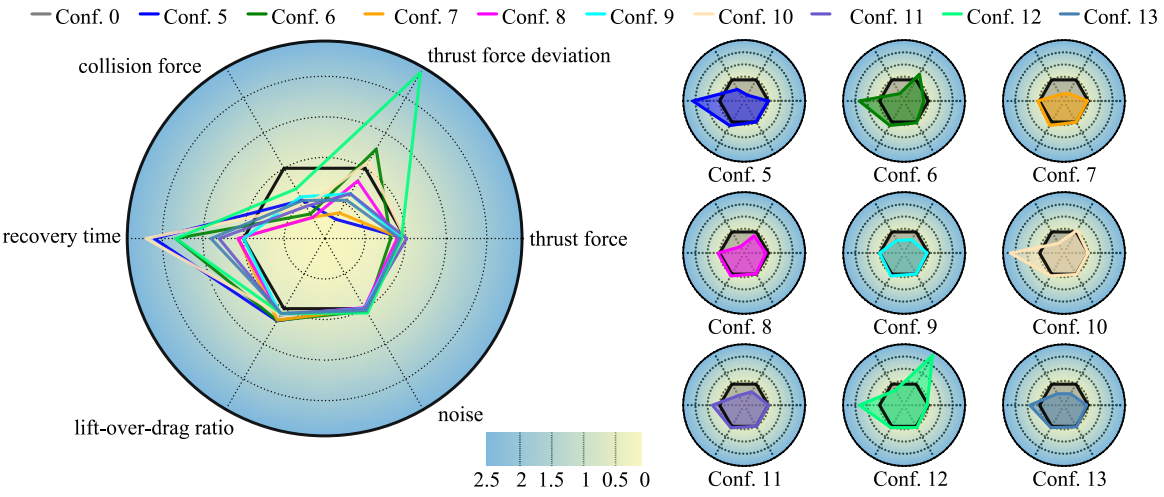

(a) Characteristics of nine Tombo propellers from Conf. 5 to Conf. 13 in comparision with that of the rigid one Conf. 0

(b) Characteristics of each Tombo propeller

FIGURE 5.15: Comparison between nine variations of the *Tombo* propeller and a traditional rigid propeller, normalized using the metrics of the rigid propeller. The results are presented in Table 5.1, showing the *Tombo* propeller in various colors and the rigid propeller in black. Table 5.3 contains further information about the metrics used for each *Tombo* propeller configuration in comparison to the rigid propeller.

6 Fly experiments with *Tombo* propellers

This section investigates the performance of *Tombo* propellers on drones (quadrotors, as depicted in Figure 6.5) during practical flight, as well as how the controller responds to a collision between the *Tombo* drone and a stationary obstacle in mid-air. The *Tombo* propellers (specifically, Conf. 13) were chosen for this experiment due to their low thrust deviation (as described in section 5.3) and high stiffness of the nodus and deformable edge (as shown in Table 5.1), which makes them easy to fabricate and produces consistent results among fabricated propellers. To enhance the self-recovery capabilities of our deformable propellers, an equilibrium bounce reaction scheme was implemented [102] specifically designed to rescue the *Tombo* drone (quadrotor) from a sudden fall in the event of a propeller-obstacle collision.

6.1 Recovery control strategy for *Tombo* propeller

In order to enhance the safety of drones through the use of deformable propeller recovery, I conducted a study on an equilibrium bounce reaction strategy that aims to prevent a Tombo quadrotor from falling in the event of a collision between a propeller and an obstacle (as shown in Figure 6.1a). I examined a scenario where the quadrotor is flying along a designated trajectory $\mathbf{X}_d$ and one of its front propellers hits an obstacle located at a designated position $\mathbf{x}_c \in \mathbb{R}^3$ in the global $\{W\}$ coordinate frame (as depicted in Figure 6.5). Once $\mathbf{x}_c$ is reached and the collision occurs, the reaction mode is activated, setting the equilibrium position to $\mathbf{x}_r = \mathbf{x}_c + d_r \mathbf{n}_r$. In this equation, $d_r > 0$ represents the bounce distance and $\mathbf{n}_r$ is the reactive normal

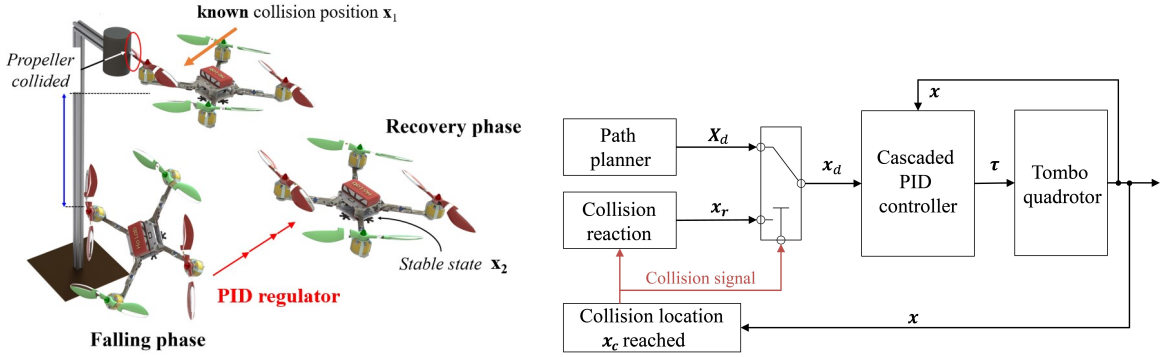

(A) Description of drone with reaction strategy

(B) Schematic of the reaction strategy

FIGURE 6.1: Illustration of the response strategy that was carried out after the *Tombo* propeller hit a stationary object is provided.

that is opposite to the direction of flight prior to the collision. This process prompts the low-level controller to generate virtual forces that guide the quadrotor towards the equilibrium state $\mathbf{x}_r$, allowing it to stabilize at a safe distance from the obstacle. Based on experiments, the falling rate of the quadrotor was found to be around 0.3 m/s and the propeller recovery time was approximately 0.42 seconds. Therefore, a PID (proportional-integral-derivative) cascaded controller could potentially be used for low-level control. The equilibrium bounce reaction strategy is summarized in Figure 6.1b, and the implementation of the reactive control strategy using **R**obot **O**perating **S**ystem (ROS) [103] is available in our git project[1] as open source.

6.2 Drone setup

6.2.1 Hardware

Based on the S500 frame[2], a customized drone was built (see Figure 6.2). The main hardware of this drone includes *Tombo* propellers, pearl markers, a Pixhawk Px4 flying controller[3], and an onboard computer TX2 Jetson[4].

[1] https://github.com/Ho-lab-jaist/tombo-propeller.git

[2] https://www.amazon.com/Readytosky-Quadcopter-Stretch-Version-Landing/dp/B01N0AX1MZ

[3] https://www.amazon.com/Readytosky-Pixhawk-Controller-Autopilot-Splitter/dp/B07CHQ7SZ4

[4] https://developer.nvidia.com/embedded/jetson-tx2

FIGURE 6.2: Main hardware of the experimental drone: *Tombo* propellers, pearl markers, a Px4 flying controller, and an onboard computer TX2 Jetson

In Figure 6.3, the control system of the PX4[5] drone is depicted. This system includes a combination of P and PID controllers, which can be used to estimate the drone's states through the application of an **E**xtended **K**alman **F**ilter 2 (EKF2) algorithm. The control architecture for the quadrotor is set up in a cascaded manner, featuring an outer loop P position controller followed by P angle and PID angular rate controllers. These controllers operate at frequencies of 50 Hz, 250 Hz, and 1 kHz, respectively. Depending on the mode selected, the outer position loop may be bypassed, as indicated by the multiplexer located after the outer loop. The position loop is only utilized when the drone is being held in a specific position through offboard control or when the requested velocity in a particular axis is zero.

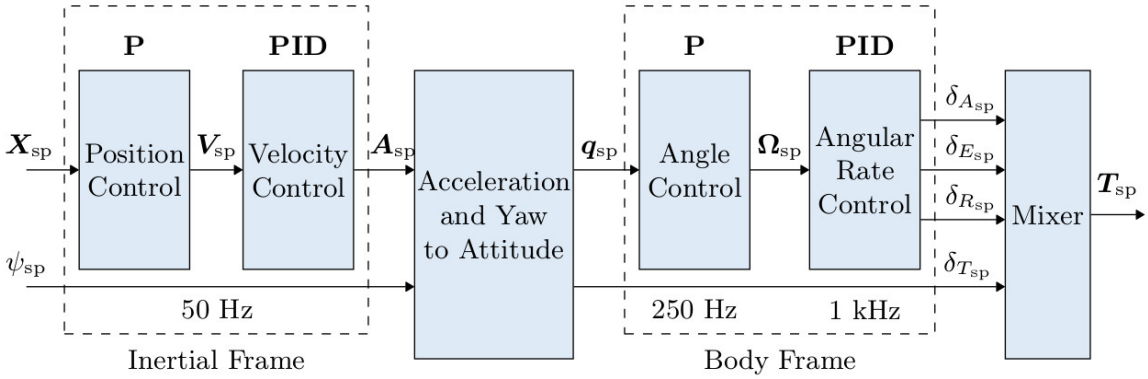

FIGURE 6.3: A standard cascaded control architecture of PX4[5]

[5] https://docs.px4.io/main/en/flight_stack/controller_diagrams.html

6.2.2 PID tunning

A **P**roportional–**I**ntegral–**D**erivative controller (PID controller) is a control loop mechanism employing feedback that is widely used in industrial control systems and a variety of other applications. In the drone field, PID is an algorithm as a part of flight controller software reads data from sensors and takes transmitter stick commands to calculate how fast the motors should spin to push the aircraft into the desired rotational speed. The desired rotational speed is referred to as a "set-point", and the displacement between the gyro sensor measurement (the actual values) and the set-point is named *error*. The goal of a PID controller in a UAV drone is to reduce *error* to zero by adjusting the speed of the rotors. It will repeat this control loop to minimize *error*.

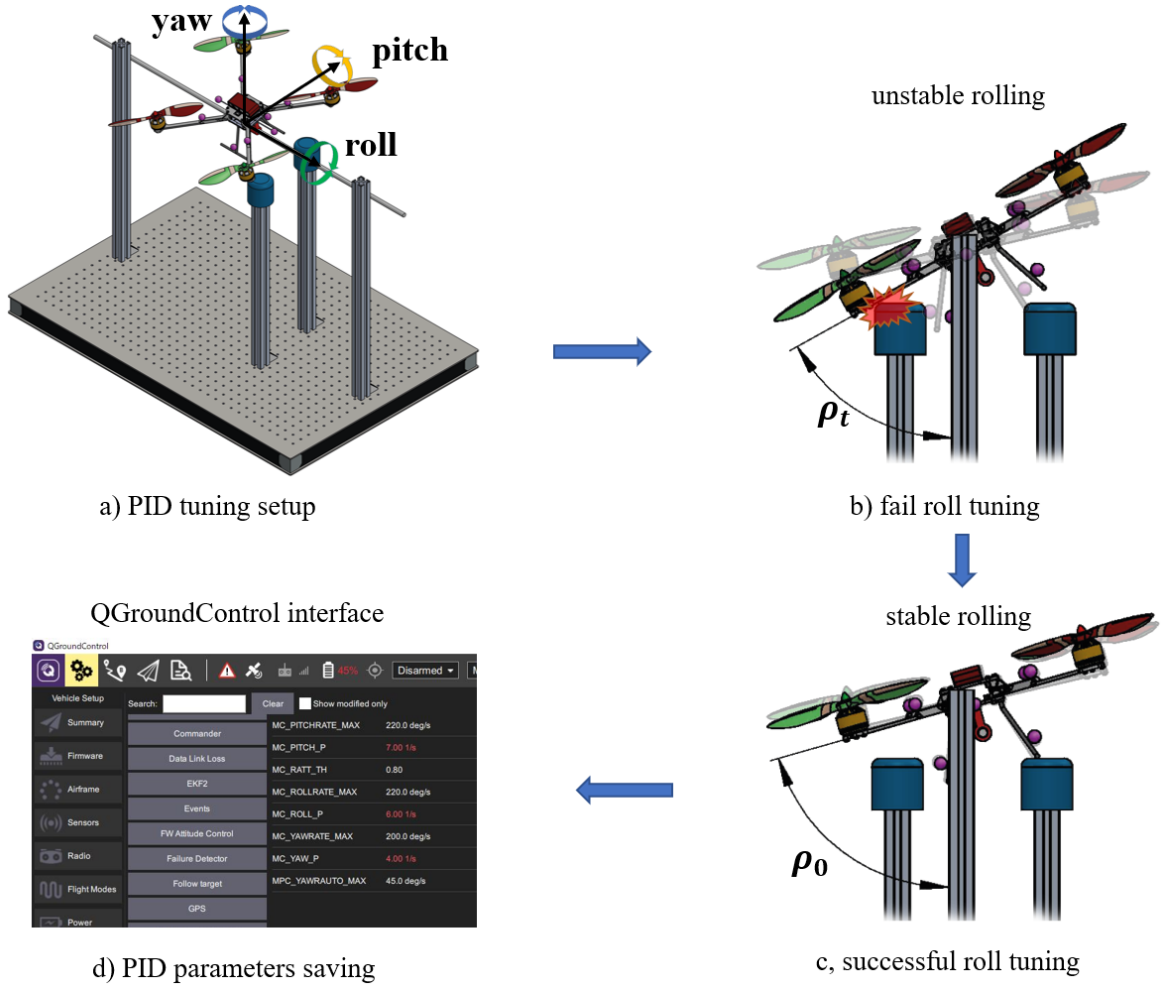

FIGURE 6.4: PID tuning experiment (case of roll tuning)

PID tuning can be done using methods such as heuristic tuning, Ziegler-Nichols

tuning, or trial-and-error PID tuning. Here, the PID of the PX4 controller was tuned by trial-and-error PID tuning because of its easy processing and practical result.

6.2.3 ROS implementation

ROS (Robot Operating System) was installed in the drone-embedded Jetson TX2 for autonomous control model (e.g., Takeoff, Landing, Hovering). Here, the position and orientation of the drone can be streamed wirelessly from the motive mocap system through the VRPN client. After that, these data and the desired state of the drone will be commanded to Px4 using an FTDI connection. ROS works as a high-level controller that promises offboard control for drone mid-air missions such as path planning, reaction, or other complex flying strategies. In fact, the proposed collision test is simple, with the recovery control strategies mentioned in the section 6.1. In this experiment, ROS kept updating the state of the drone and the fixed desired position (collision area) and triggered the recovery strategies when the collision signal was activated. Note that the collision area is characterized by a set of a radius in the YZ plane and a threshold on the collided propeller in the X direction. This radius and threshold have been tuned by a pre-test and can be applied in both flying experiments of rigid propellers and deformable propellers.

6.3 Flying test setup

The illustration in Figure 6.5 shows the indoor location where the flight and collision experiments were conducted. The experiment used a quadrotor equipped with four *Tombo* propellers and 8 reflective markers. The position of the quadrotor was accurately tracked by the *OptiTrack* motion capture system, consisting of 6 Flex 13 tracking cameras, with a positional accuracy of up to 1.2 mm. The 6-DoF pose of the quadrotor, which includes its position and orientation, was determined by the mocap system on a desktop PC (Intel i7-7700 CPU at 3.6GHz and 8 GB RAM) and then sent to an onboard computer (Jetson TX2, NVIDIA) at a rate of around 30 Hz.

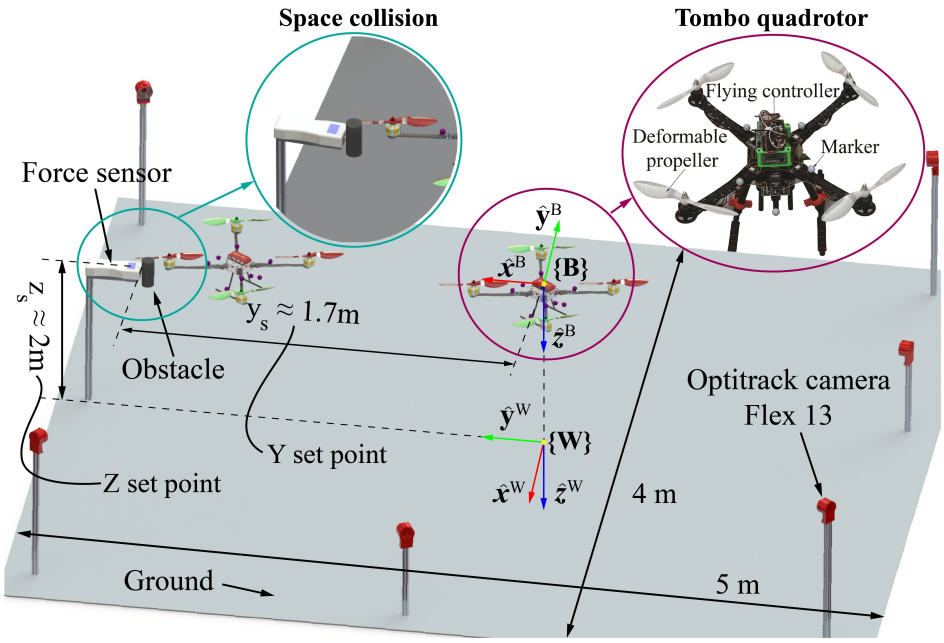

FIGURE 6.5: During flight tests and collision experiments, the OptiTrack Mocap system was utilized to determine the location of the *Tombo* quadrotor within an indoor setting. This system is specifically designed for motion picture and 3D tracking.

This allowed the real-time implementation of the automatic flight and collision reaction scheme using a PID-based low-level controller running on Pixhawk 4 autopilot hardware[6]. The real-time posture information provided feedback signals for the position and angle controllers, while the onboard inertial measurement unit was responsible for the inner PID control loop for angular rate. A collided object was mounted on a force sensor at 2 n height as the desired collision position. In this flying test, both a soft and rigid obstacle were tested to evaluate the recovery strategy performance.

6.4 Flying experiments

An experiment was conducted to assess the effectiveness of the *Tombo* propeller and the bounce reaction strategy in responding to a collision. The quadrotor was flown along a predetermined trajectory $\mathbf{X}_d$ in $\hat{y}$, and the front left propeller was made to collide with an obstacle at a specific location $\mathbf{x}_c = [0.0, 1.7, -2.0]^{\mathrm{T}}$ m. The bounce

[6] https://px4.io/

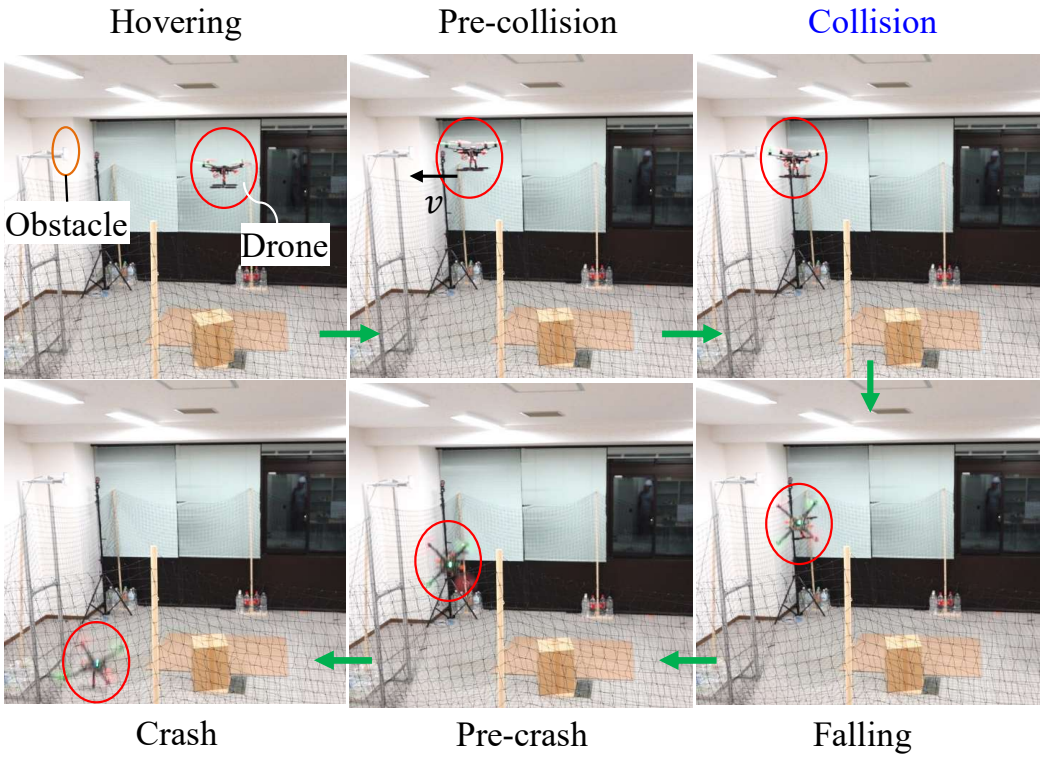

(A) Quadrotor's behaviour *without* reaction strategy

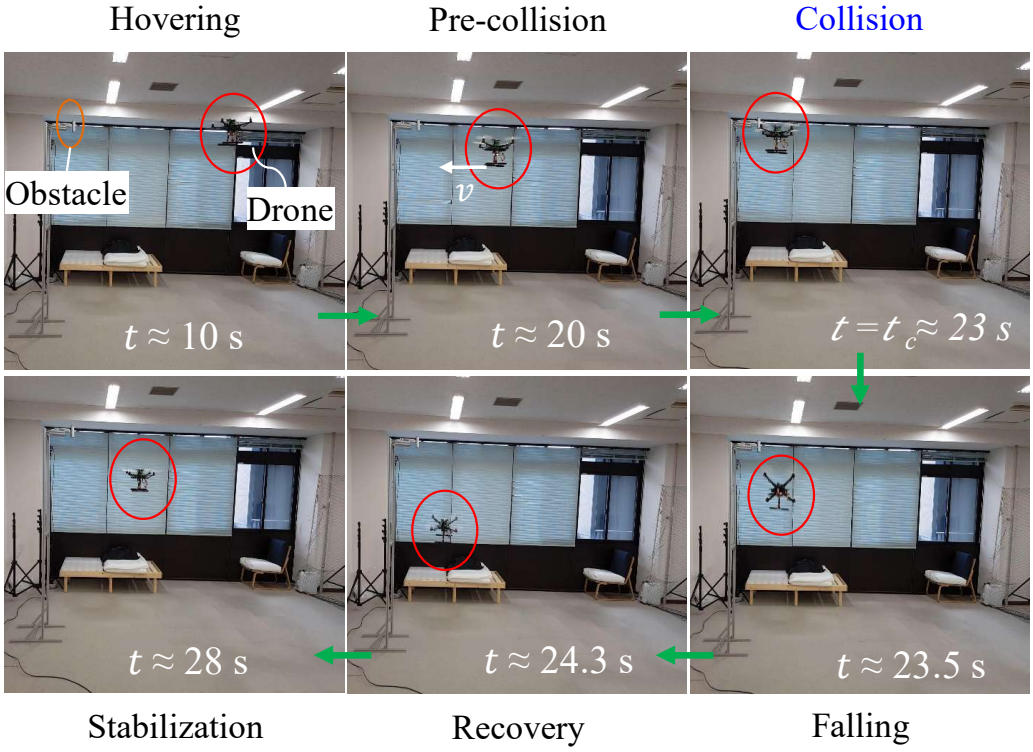

(B) Quadrotor's behaviour *with* reaction strategy

FIGURE 6.6: An investigation of how a quadrotor responds to colliding with a *Tombo* propeller obstacle revealed that without a specific reaction strategy in place, the quadrotor would crash to the ground. However, video evidence showed that the reaction strategy was able to stabilize the quadrotor within 5 seconds after the collision.

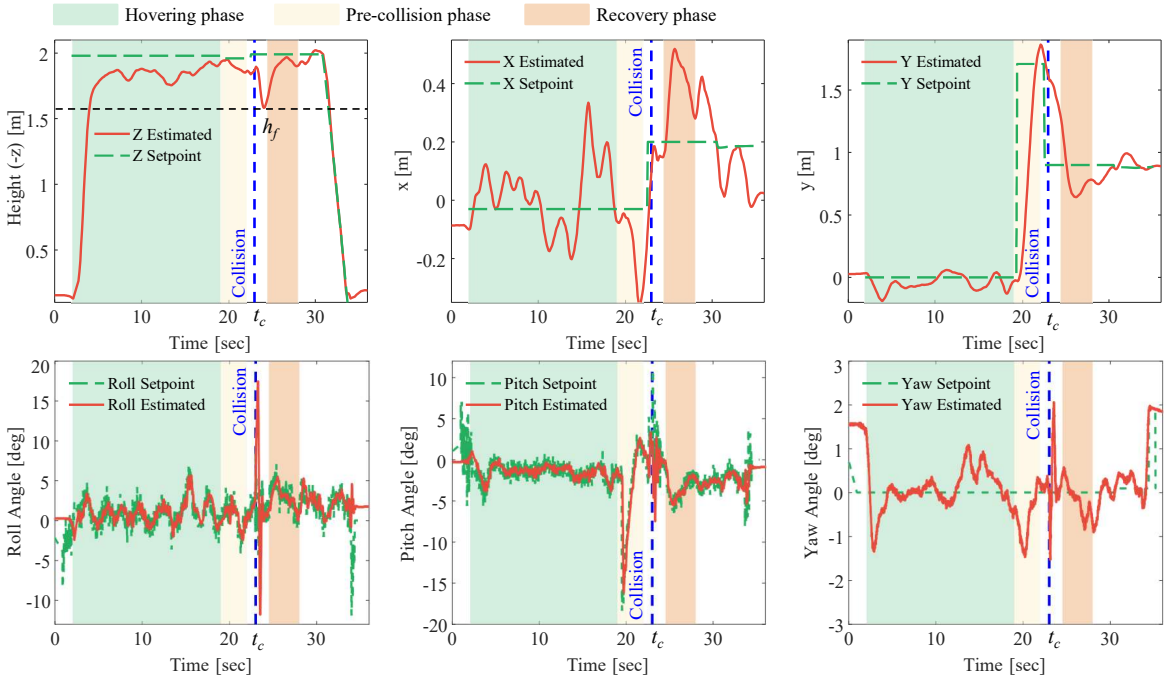

FIGURE 6.7: The records of the quadrotor's position and orientation during the flight and collision experiment reveal that the reaction control mode was activated at the moment of the collision (t_c) and attempted to stabilize the quadrotor in a safe position with coordinates $\mathbf{x}_r = [0.2,\ 0.9,\ -2.0]^{\mathrm{T}}$. It is important to note that the height of the quadrotor is represented by the negative z-coordinate.

distance was set at $d_r = 0.8\,\mathrm{m}$, resulting in the quadrotor reaching an equilibrium position $\mathbf{x}_r = [0.2,\ 0.9,\ -2.0]^{\mathrm{T}}\,\mathrm{m}$ for the recovery process to begin. During the hovering and pre-collision (flying along the y-direction) phases (Figure 6.6b), the quadrotor was able to maintain stability while tracking the reference trajectory (see Figure 6.6b). However, without the bounce reaction strategy, the quadrotor was unable to recover from the collision and crashed. However, with the use of the bounce reaction strategy and the fast recovery of the Tombo propeller, the quadrotor was able to stabilize following the collision (see Figure 6.6b).

The behavior of the quadrotor during a collision and recovery process is shown in Figure 6.7. When a collision occurred at around $t_c = 23\,\mathrm{seconds}$, the quadrotor went through an unstable phase where it oscillated and overturned, with a large fluctuation in roll angle, before starting to fall. However, it did not fall all the way to the ground, and it took about 1.5 seconds to overcome the unstable phase before

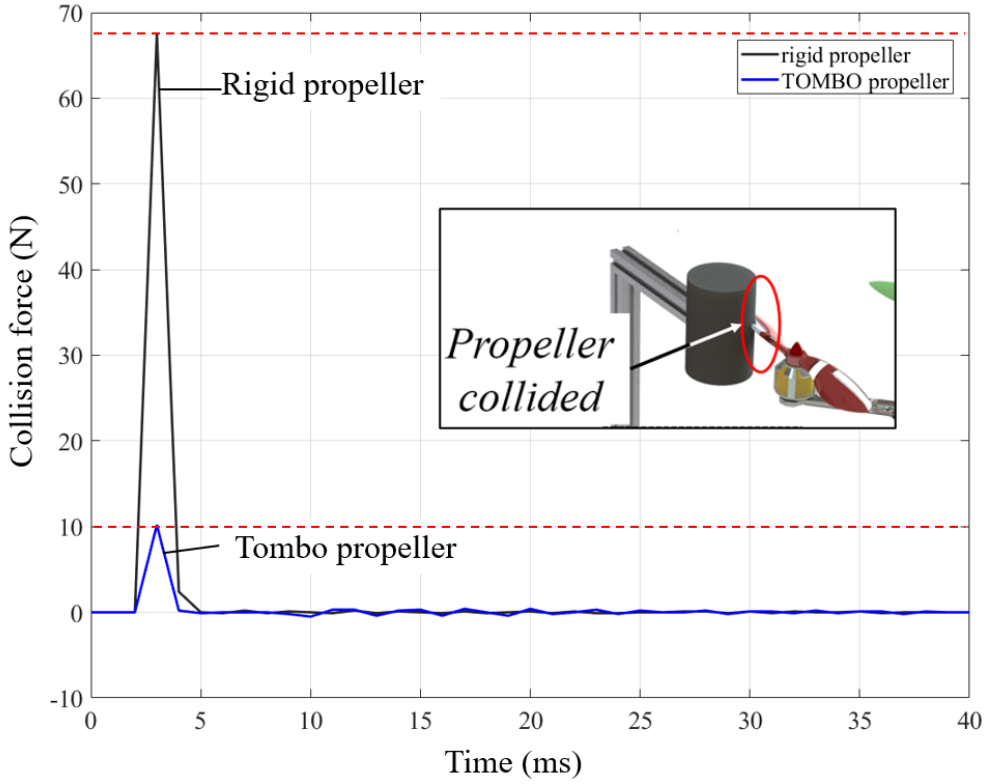

FIGURE 6.8: Mid-air collision force report

beginning a recovery process that lasted approximately 3.5 seconds. The Tombo propeller and the reaction strategy were effective in allowing the quadrotor to recover and attain a stable state. During the recovery, the quadrotor followed a straight-line path towards its predefined equilibrium position, starting from the lowest point at which its orientation had been restored to its initial state. The results of this experiment demonstrate the quadrotor's ability to recover after a collision and its ability to perform basic flight and hovering, even with the use of a softer propeller that reduces the risk of damage, that can be found in the video[7]..

Consequently, in this section, I confirmed the flight ability of the drone with a *Tombo* propeller in a real platform and the recovery ability after the collision. In addition, the obtained results reveal that with minimal invasion of the classical control strategy, the drone with *Tombo* propeller still can perform basic flight/hovering and novel reactions upon collision with the surrounding. As a result, introducing

[7] https://youtu.be/zjHvukgfJwc

softness to the propeller decreases the risk of damage and does not necessarily compromise the flight ability of the drone.

Mid-air collision force has been reported in Figure 6.8. The result indicated that the collision force made by a *Tombo* propeller was one-seventh of that of a rigid one. Although the posture of collision might be a little different between both cases cause of the error of propeller posture at the collision spot, this collision force measurement once again confirmed the essential contribution of soft material to propellers. In the future, more investigations of mid-air collisions will be conducted to elaborate on the potential of deformable propellers in different tasks.

7 *TomboHub*: Collision sensing and shock absorbing

The propeller crash topic attracts less attention than the drone collision issue because of the apparent fact that in most accidents, the collided propeller is mainly broken, and the drone is flat down. There are many studies on the state recovery of drones after a collision [102], [104]–[111], however, the level of impact, as well as the collision characteristics with the object of the propeller and other parts of the drone, is different. In detail, the crash force of the propeller is much more critical than that of the guard or body. Therefore, the most common propeller-related research public is the rotor failure [112]–[115].

The successful flying test in Chapter 6 suggests that if a drone wants to survive, recover, and keep stable working after a propeller crash, these conditions named "***un-falling conditions***" must be satisfied.

- Collided propeller is not broken,
- Recovery strategy needs to be activated on time after a collision,
- The room for recovery is enough;

In practical missions without a vision-based tracking system (e.g., outdoor delivery task), the drone remains sensitive to propeller crashes. While the *Tombo* propeller is one of the solutions for the first aforementioned condition and the third condition can be resolved by a fast and reasonable recovery strategy, the second condition remains challenging for both *Tombo* and standard propellers because of the lack of research. Despite conducting extensive research, none of reports about the method

of detecting the collision of drone's propeller was found. Moreover, the *Tombo* propeller has room for development and finishing, so it is a process of bringing *Tombo* to life. In this scenario, a new question appears in my mind: **Is there any mechanism that can sense the propeller crash to support *Tombo* propeller trigger the recovery strategy?**

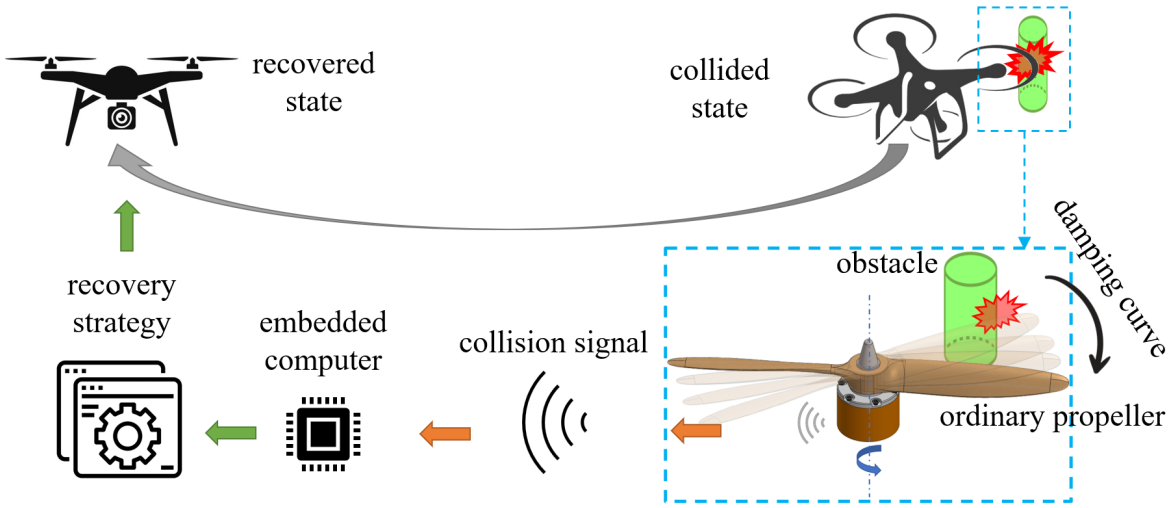

FIGURE 7.1: *TomboHub*'s structure idea

The above question becomes the motivation for proposing the *TomboHub*, a collision sensing and shock absorbing mechanism. *TomboHub* was designed as an extra device that can be mounted on the top of the rotor to support collision sensing and shock absorption.

The idea of *TomboHub* functions as illustrated in Figure 7.1. First, *TomboHub* is integrated into the drone's rotor. When a collision happens, *TomboHub* will help the propeller rotate in the inverse rotational direction while keeping the rotor rotating. If the collision force is over the impact force threshold, a collision signal is sent to the embedded computer on the drone. Then the recovery strategy that is mentioned in section 6.1 was activated. Overall, *TomboHub* can be equipped with arbitrary propellers, including *Tombo*, to support the abilities of collision impact reduction and collision detection as an essential input for re-hovering control.

7.1 Structure design

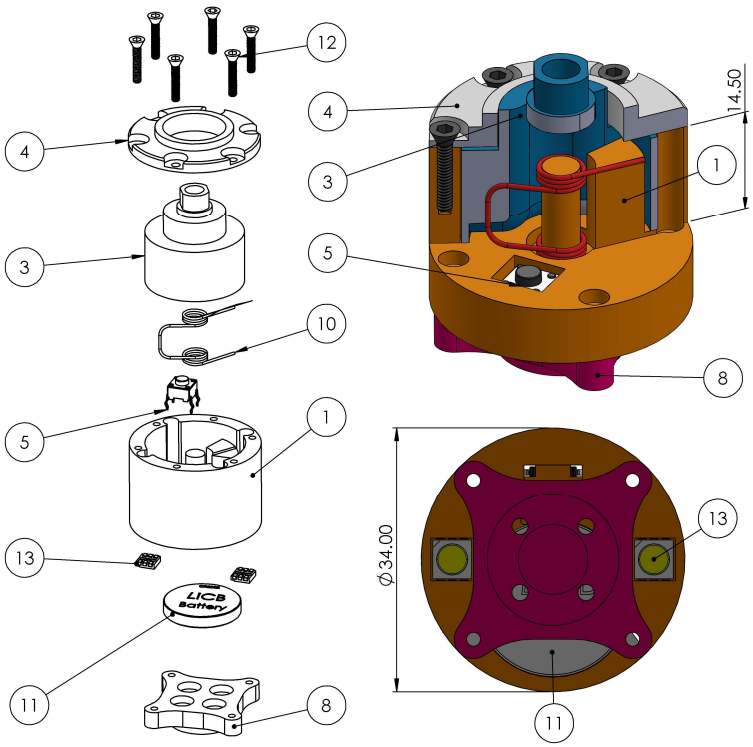

FIGURE 7.2: *TomboHub* structure includes Hub.Outer 1, Hub.Shaft 3, Hub.Ring 4, Hub.Button 5, Hub.Adapter 8, Hub.Spring 10, Hub.Battery 11, Hub.Screw(s) 12, and Hub.IR.Led(s) 13

The design of *TomboHub* is shown in Figure 7.2. Hub.Shaft 3 has a free end which is used to lock the propeller. Hub.Adapter 8 connects with a rotor for a moment transformation. In the rest state, Hub.Shaft 3 coincides with Hub.Outer 1 by the initial compress force from Hub.Spring 10, a double torsion spring, and covered by Hub.Ring 4. When the rotor rotates in the clockwise direction, Hub.Outer 1 will move in the same direction as Hub.Shaft 3, which leads to the rotation of the propeller. When a collision happens, Hub.Spring 10 will deform and bring the propeller back to an un-colliding state. This motion helps Hub.Shaft 3 triggers Hub.Button 5, as a result, collision signal generated by Hub.IR.Led 13 will be active and transferred to a receiver implemented on the drone arm. Hub.Battery 11 supports the energy for Hub.IR.Led(s) 13. Finally, the embedded computer on the drone receives and processes this signal to activate the control strategy and leads the drone bound back to a safe position.

The design helps *TomboHub* can be scaled up or universal assembly with various type of propellers. Figure 7.3 shows that a *TomboHub* can works well in practical test with these propellers with the size from 5 to 10 inch.

FIGURE 7.3: *TomboHub* universal design for assembly with various sizes propeller

7.2 Fabrication

Figure 7.4 shows the fabrication process of *TomboHub*. In the first step, *TomboHub* was designed using 3D CAD software SolidWorks 2020. Next, the Hub.Outer 1, Hub.Shaft 3, Hub.Ring 4, and Hub.Adapter 8 was made of polylactide (PLA) plastic and printed by a 3D printer Sermoon D (Creality 3D, China). Finally, these printed parts are assembled with other commercial products (such as a button battery 3 V, two infrared LEDs, and a push-button) to get a completed *TomboHub*.

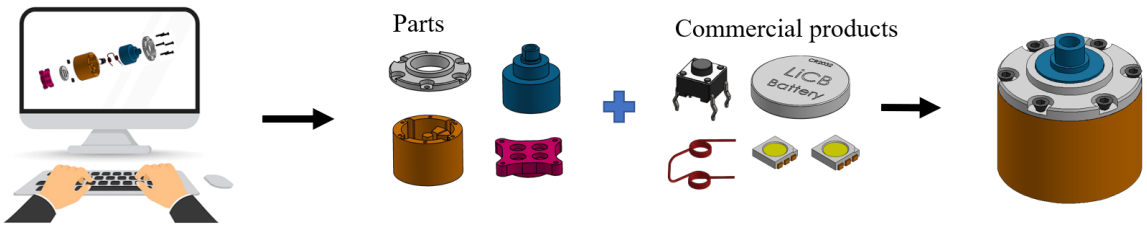

FIGURE 7.4: *Tombo* Hub fabrication process

7.3 *TomboHub* modelling

In this section, a propeller collision event is modeled to define the behavior of *TomboHub* (see Figure 7.5). The following assumptions were used for simplicity in this event investigation.

- The energy losses when transmitted through the contact surfaces of the *TomboHub* are neglected,
- The propeller is rigid, and the impact is absolutely elastic.

The collision process is complex in the case of a *Tombo* propeller crash. The main reason is the soft *nodus* and deformable edge can absorb impact energy and deform. In this case, a development collision modeling must be elaborated in the future.

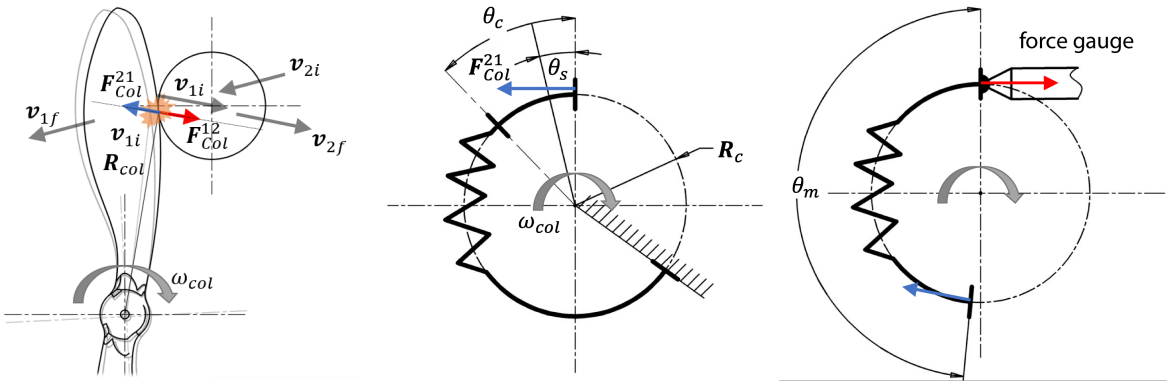

(A) Impact force modelling (B) Twist angle modelling (C) Torsion spring rigidity coefficient experiment

FIGURE 7.5: Illustration of *TomboHub* collision modelling and rigidity coefficient measurement

7.4 Impact force modelling

Figure 7.5a illustrates a propeller collision. Assume that a propeller has mass m_1 rotating with the rotational speed at ω_i collides with an obstacle of mass m_2 approaching with velocity v_{2i} at a point R_i from the center of the propeller. With the aforementioned assumptions, the kinetic energy and momentum of the system are conserved before and after the state of collision, therefore

$$\frac{1}{2}m_1\mathbf{v}_{1i}^2 + \frac{1}{2}m_2\mathbf{v}_{2i}^2 = \frac{1}{2}m_1\mathbf{v}_{1f}^2 + \frac{1}{2}m_2\mathbf{v}_{2f}^2 \tag{7.1}$$

$$m_1\mathbf{v}_{1i}^2 + m_2\mathbf{v}_{2i}^2 = m_1\mathbf{v}_{1f}^2 + m_2\mathbf{v}_{2f}^2 \tag{7.2}$$

with $\mathbf{v}_{1i}$, $\mathbf{v}_{1f}$ are the velocities of the collided point in the propeller before and after the collision, respectively; $\mathbf{v}_{2f}$ is the velocity of the obstacle after the collision; therefore, I have

$$v_{1i} = \omega_i \pi R_i \tag{7.3}$$

From Equation 7.1 and Equation 7.2, the velocities of the propeller and obstacle after a collision can be defined below

$$v_{1f} = \frac{m_1 - m_2}{m_1 + m_2}\mathbf{v}_{1i} + \frac{2m_2}{m_1 + m_2}\mathbf{v}_{2i} \tag{7.4}$$

$$v_{2f} = \frac{2m_1}{m_1 + m_2}\mathbf{v}_{1i} + \frac{m_2 - m_1}{m_1 + m_2}\mathbf{v}_{2i} \tag{7.5}$$

If I call Δt the length of the collision duration time (or the time of contact), $\Delta\mathbf{P}$ is the change of propeller's momentum (impulse) during the collision process,

$$\Delta\mathbf{P} = m_1(\mathbf{v}_{1i} - \mathbf{v}_{1f}) \tag{7.6}$$

$$\Delta\mathbf{P} = \frac{2m_1m_2}{m_1 + m_2}(\mathbf{v}_{2i} - \mathbf{v}_{1i}) \tag{7.7}$$

Finally, I have

$$-\mathbf{F}^{12} = \mathbf{F}^{21} = \mathbf{F}_{col} \tag{7.8}$$

$$\mathbf{F}_{col} = \frac{\Delta \mathbf{P}}{\Delta t} \tag{7.9}$$

$$\mathbf{F}_{col} = \frac{2m_1 m_2}{m_1 + m_2} \frac{\mathbf{v}_{2i} - \mathbf{v}_{1i}}{\Delta t} \tag{7.10}$$

with $\mathbf{F}^{12}$ and $\mathbf{F}^{21}$ are the collision forces from the propeller applies to the obstacle and vice versa, respectively.

Equation 7.7 indicates that the impulse of a propeller with or without *TomboHub* after a collision is the same. However, the difference between in two cases is presented in Equation 7.10. Here, the time of contact decides the magnitude of the impact force. The system includes *TomboHub* seems "softer" than the standard one, therefore, it is forecasted that the collision force of a propeller equipped *TomboHub* is lower than that of the one without *TomboHub*. This assumption needs to be proved by practical experiments.

7.5 Twist angle modelling

Based on the aforementioned assumptions, the kinetic energy of the propeller will be transmitted intact to Hub.Shaft 3 and canceled by the resistance of the spring (see Figure 7.5b). In other words, the kinetic energy of the propeller will be transformed into the potential energy of the torsion spring. Therefore, I have

$$\frac{1}{2} m_1 \mathbf{v}_{1f}^2 = \frac{1}{2} k \theta_c^2 \tag{7.11}$$

with θ_c the maximum twist angle of the torsion spring

$$\theta_c = \sqrt{\frac{m_1}{k}} v_{1f} \tag{7.12}$$

Here k is the rigidity coefficient of the torsion spring defined by a pre-experiment. From Equation 7.12, the *TomboHub* can be designed based on the sensing range of magnitude of impact force as below.

- The maximum twist angle of the torsion spring in the design must be larger than θ_c (calculated by the maximum impact force of the sensing range). That means I can change this maximum twist angle by design or choose another torsion spring with different rigidity to satisfy this condition,
- The position of Hub.Button 5 is defined by the minimum twist angle of the torsion spring, calculated by the maximum impact force of the sensing range
- The magnitude of impact force is estimated by the time length between two collision signals (the former activates when the torsion spring starts deforming, and the latter receives when the torsion is recovering). In detail, this time length t_{col} is calculated as below

$$t_{col} = 2\sqrt{\frac{m_1}{k}} \arccos \frac{\theta_s}{\theta_c} \tag{7.13}$$

with θ_s is the angle design of Hub.Button 5 (see Figure 7.5b).

7.6 Torsion spring rigidity coefficient measurement

Figure 7.5c shows the principle of the experiment for measuring the rigidity of the torsion spring k. This principle is simple. One of this spring's ends is fixed at the top of the force gauge, while the other end is free. Note that the central axis of the force gauge must be normalized with the spring's fixed end. First, the free end of the spring will be set at a rotational angle θ_m. Then, the measured force F_m will be reported, and k can be calculated by Equation 7.14.

$$k = \frac{F_m}{\theta_m} \tag{7.14}$$

FIGURE 7.6: Propellers used for experiments

TABLE 7.1: Recovery time of several propellers with/without *TomboHub*

Propeller's name	**Hobby**	**Foldable 10x6**	***Tombo***
	with/without TomboHub	with/without *TomboHub*	with/without *TomboHub*
Recovery time (second)	0.517/0.733	0.448/1.35	0.439/0.378

7.7 Experimental setup and results

7.7.1 Recovery time experiment

This experiment was conducted as in section 5.1.3 with three types of propellers: commercial Hobby 10 inch propellers, a commercial foldable Aero Naucam 10x6 propeller, and *Tombo* propellers (see Figure 7.6) in both cases: with and without *TomboHub*. The result was summarized in Table 7.1.

The results indicate that *TomboHub* plays an important role in shortening the recovery time of commercial propellers after the collision. While the Hobby propeller's recovery time was reduced by about 30%, the foldable Aero Naucam 10x6 propeller with *TomboHub* saw a significant reduction as the recovery time was only one-third compared to that of this propeller without *TomboHub*. This change is important for the recovery process as mentioned in the ***un-falling conditions***. Based on my understanding, none of the extra mechanisms can benefit the same value as this.

In the case of the *Tombo* propeller, the story follows a different scenario. Because

the *Tombo* propeller allows the blade to be folded at *nodus*, the hypothesis put forward here is that in the event of a collision without *TomboHub*, most of the impact energy will be transferred to *nodus* and cause extensive local deformation here. As a result, the axial portion of the propeller continues to rotate, and only a fraction of the impact energy impedes this rotation, causing recovery time. In case of a collision with *TomboHub*, the collision energy will be transferred to *nodus*. However, because *TomboHub* enables *Tombo* propeller to rotate around the axis in the opposite direction of the rotor's rotation, a more significant part of the energy has been applied to the propeller's shaft, making the energy impeding the rotation of the *Tombo* wing larger than without *TomboHub*. As a result, *Tombo* propellers will recover more slowly in this case. However, this also benefits the durability of *nodus* because the cumulative impact energy is less, so I believe *TomboHub* will help increase the working lifetime of *Tombo* Propellers.

7.7.2 Collision force experiment

This experiment was conducted with the same principle as in section 5.1.4. Commercial propellers and *Tombo* propellers were used to test this experiment, and the result was summarized in Figure 7.7.

It can be seen that *TomboHub* does not contribute to reducing the collision force of *Tombo* propeller according to the experiment result. That leads us back to Equation 7.10, where the Δt depends on the time of collision θ_c. Here, thank to the deformable leading edge of *Tombo* propeller, the process of impulse transferring was decided by the deformation of the soft material that is almost the same in both collision cases with or without *TomboHub*. However, in the case of rigid propellers, the commercial Hobby propellers, the contribution of *TomboHub* is clearly seen. In the rotational speed range from 2000 to 3500 rpm, the collision forces were reduced significantly. Especially, the decrease at the rotational speed of 3000 rpm goes to 30%, which can improve the lifetime of rigid propellers. At least two Hobby propellers were broken

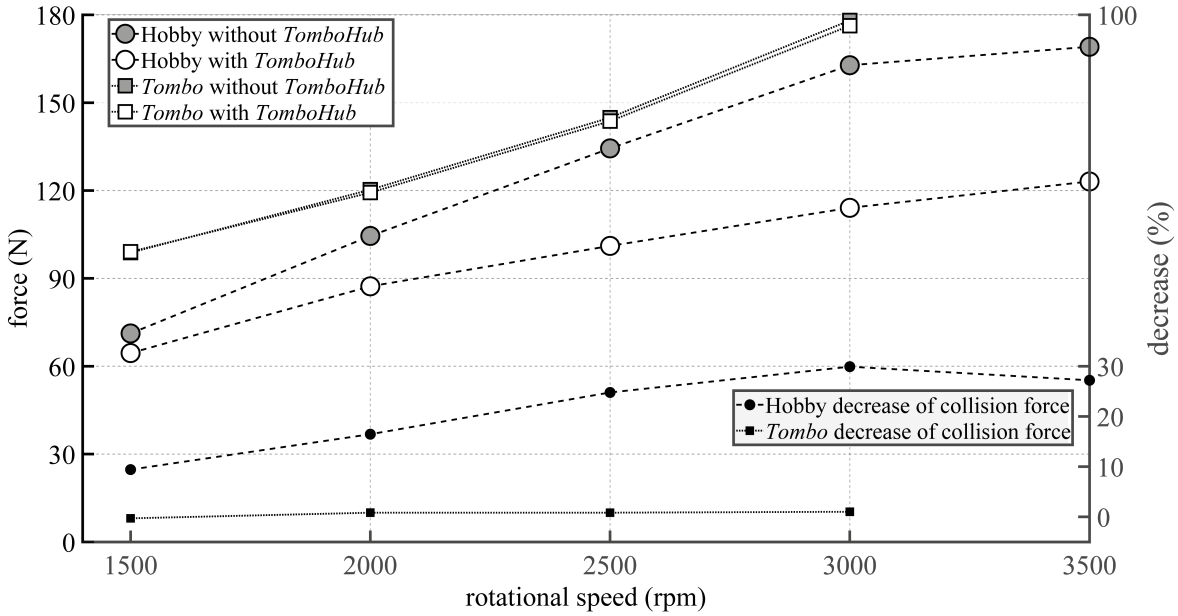

FIGURE 7.7: Comparison of collision forces of propellers with and without *TomboHub*

in the experiment without *TomboHub*, while none of the damage was reported in the experiment with this novel hub.

7.7.3 Collision sensing experiments

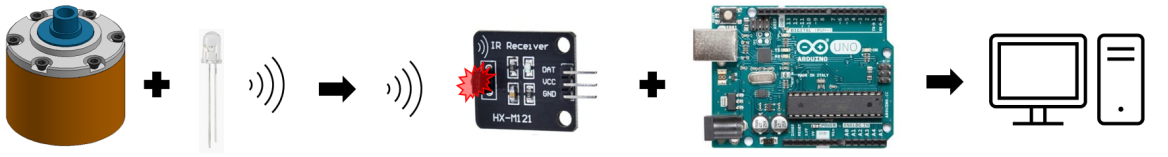

(1) TomboHub with infrared led

(2) Collision signal transmission

(3) Arduino UNO embed infrared receiver

(4) Processing by a PC

FIGURE 7.8: *TomboHub* collision sensing experiment setup

In these experiments, an Arduino UNO board with an embedded infrared receiver was used to collect the infrared signal from the infrared LEDs. The Arduino board connected to a PC, and the data was recorded and saved into a CSV file for later processing (see Figure 7.8). Only Hobby propellers were used to conduct these experiments.

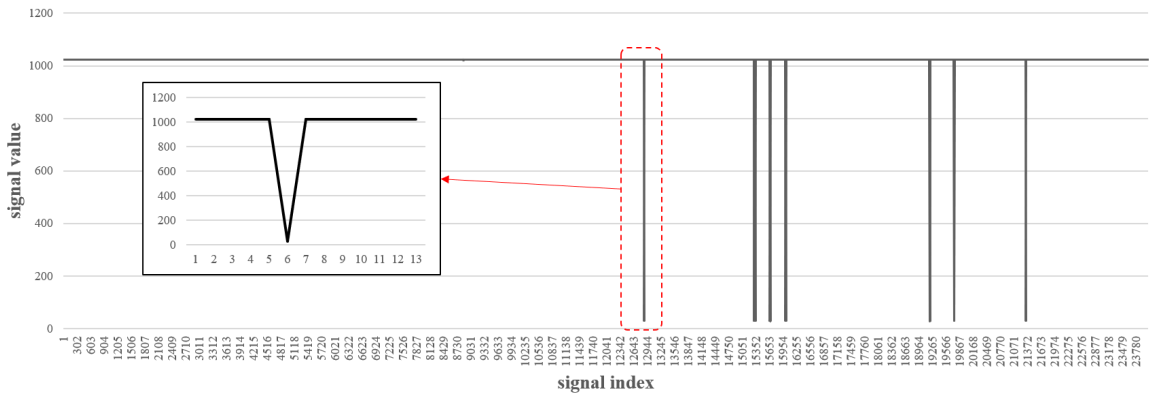

FIGURE 7.9: *TomboHub* collision sensing sensitivity performance

The sensitivity

Here, the sensitivity of *TomboHub* was defined by the frequency of the infrared signal reading from the receiver. I have set the baud rate to 2,000,000 in the program and the Arduino board setting. Finally, the infrared signal was read at 432 Hz. In other words, this *TomboHub* can sense all collisions if the button is kept pushing longer than 2.32 μs. This calculation helps to optimize the design of *TomboHub*. For example, the easiest way is to change the size of the button-touch part of the Hub.Shaft 3 is to be giant enough for a long press. Note that this time of pressing will affect the result in Equation 7.13. Therefore, the sensing abilities, such as the force sensing range and the sensitivity, strongly depend on the *TomboHub* design. In my test, *TomboHub* has successfully detected every collision event with various kinds of colliding. One of these has been reported in Figure 7.9.

Collision sensing demonstration

The experiment presents the collision sensing ability of *TomboHub*. A commercial Hobby propeller was used to conduct at the rotational speed of 2500 rpm (see Figure 7.10). The collision process and the infrared signal were recorded by a high-frame camera and an Arduino board, in turn. The results indicate that the *TomboHub* defines the collision in every case. None of the missing signals was reported. However, the latency between the time when the collision event happens and the PC record time has not been indicated. Therefore, the practical sensitivity of *TomboHub* does

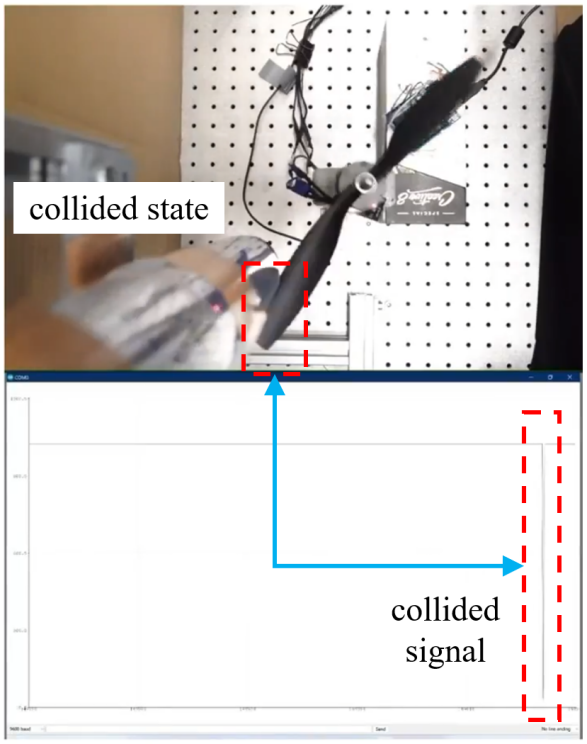

FIGURE 7.10: *TomboHub* collision sensing demonstration

not clearly elaborate. This missing point is essential because it affects the time of activating the recovery strategies leading to the safety of UAVs.

7.7.4 Flying demonstration

In this experiment, a drone presented in section 6.2 was equipped with four *TomboHub*s and four Hobby 10 inch propellers (see Figure 7.11). The experiment was conducted indoors, and the drone was controlled manually for hovering tasks. The result shows that the drone hovered and changed direction well, and no significant vibration was recorded. Therefore, it can be concluded initially that the *TomboHub* does not affect the drone's fly ability. However, a drone mid-air collision has not been processed to evaluate the ability of this hub in practical application.

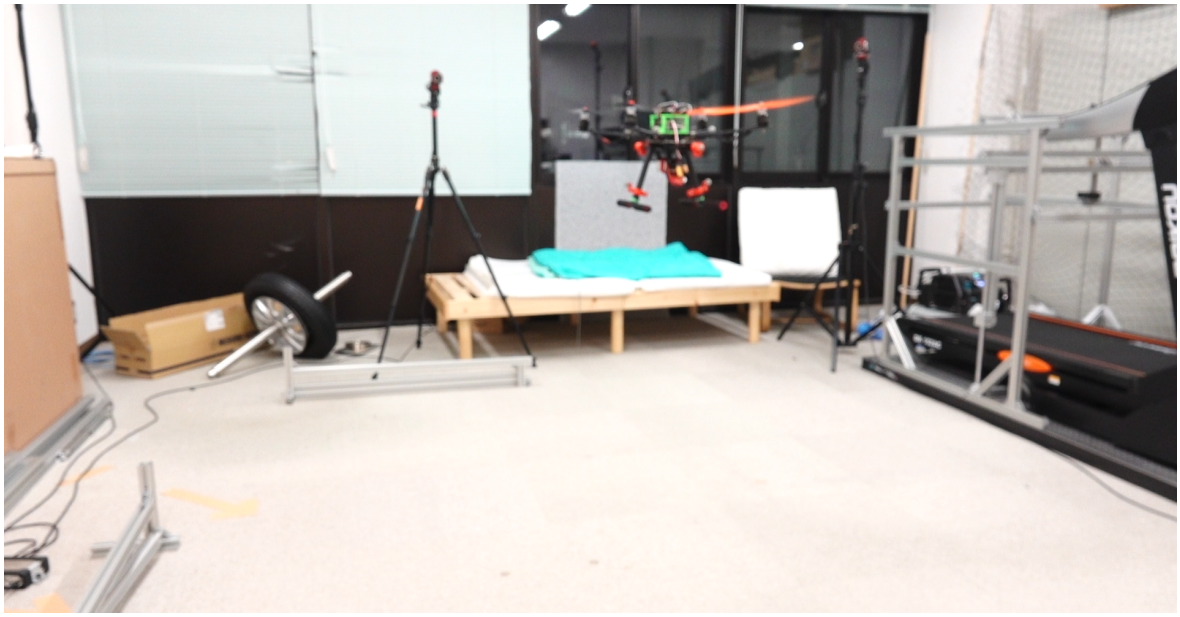

FIGURE 7.11: Succesful hovering demonstration of a drone equipped *TomboHub*

8 Discussion and conclusion

In this work, I proposed designing and fabricating a bio-inspired propeller named *Tombo*. This approach was developed that can be used on various kinds of propellers, such as flapping wing and glider wings. This aerodynamic model should be able to accurately predict the propeller's thrust force and deformation angle in the plane perpendicular to the rotor plane. Examining the *Tombo* propeller showed that it has useful features and can be used on various vehicles. Moreover, multiple flight tests showed that the *Tombo* propeller can improve a drone's collision resistance while still maintaining its mechanical structure after the impact. In addition, a novel deformable hub was introduced to support a sensing ability for this *Tombo* propeller. The combination of *Tombo* propellers and *TomboHub*s is expected to be the optimal solution to the problem of collisions with propellers toward an absolutely safety - unfalling drone

8.1 Impact of bio-inspired structure on collision accommodated control for robotics system

8.1.1 Design and fabrication

Applying soft materials in traditional propellers can improve the safety of drones, particularly when it comes to recovery and reducing the risk of collisions. The process of attaching tendons to the propeller's matrix by gluing them to the rigid parts (hub and wing) requires a lot of skill and precision. However, this process can impact the quality of the propeller, decreasing its durability over time. In order to mass produce the *Tombo* propeller, it is necessary to automate the fabrication process. One

of the most difficult tasks is accurately placing the tendons during the assembly of the *Tombo* propeller. This process can be automated using hole processing and heat welding to attach the tendons to the holes in the rigid parts. Additionally, using injection molding to create rigid parts can improve their rigidity, smoothness, and consistency, rather than using 3D printing. This mass-production method will increase the efficiency and durability of the *Tombo* propeller. Through evaluation experiments, it was also found that during rotation, the entire *Tombo* propeller from the hub to the tip becomes very stiff due to centrifugal force. Therefore, if the connection between the nodus and the rigid parts is secure, the tendons may not be necessary. For example, the double injection method could be used in mass production of the *Tombo* propeller, creating a reliable connection between the soft nodus and the rigid parts, as well as increasing the propeller's lifespan. This method is also expected to result in high-quality *Tombo* propellers at low manufacturing costs, which benefits both manufacturers and users. Further investigation into this approach will be conducted in future work.

In our current design, thick airfoils were chosen for ease of manufacturing, especially the fabrication and assembly of the nodus part. However, users interested in *Tombo* propellers may choose suitable airfoils to develop their own deformable propellers. The experiment results in Chapter 5 indicate that the average thrust force, thrust force deviation, and noise of the experimental *Tombo* propellers are almost the same as those of the rigid propeller. Therefore, if the original morphology of *Tombo* (the rigid one) has high efficiency, it can improve the energy consumption performance of the Tombo also. Additionally, the posture of *Tombo* has changed at each rotational speed of the rotor, which results in the thrust force. This change differs from the configurations of *Tombo*. In other words, the posture of *Tombo* decides the efficiency of these propellers. Although the current design of the Tombo propeller may be more cost and challenging to manufacture, its efficiency can be improved by using high-performance airfoils for the blade parts. Despite this, the results of experiments presented in this paper demonstrate that the Tombo propeller is able

to withstand multi-directional collisions and significantly reduce the impact force on surrounding objects, thanks to its unique design. These benefits result in improved collision adaptation compared to traditional rigid propellers. Additionally, the Tombo propeller is durable enough for use in actual flight scenarios, as demonstrated by the fact that it was able to continue operating after ten collision events, even though the propeller repeatedly hit the obstacle during each event. The scalability of the Tombo propeller has also been demonstrated, as it has been successfully fabricated in various sizes including 5, 9, 10, and 20 inches in length. The durability, scalability, and flying performance of the 5-inch Tombo propeller-equipped drone can be seen in video[6]. In the future, the Tombo propeller will be explored in different sizes and shapes. Therefore, although the Tombo propeller may have some limitations in terms of efficiency, its inherent flexibility and resilience provide potential advantages for the overall safety of drones.

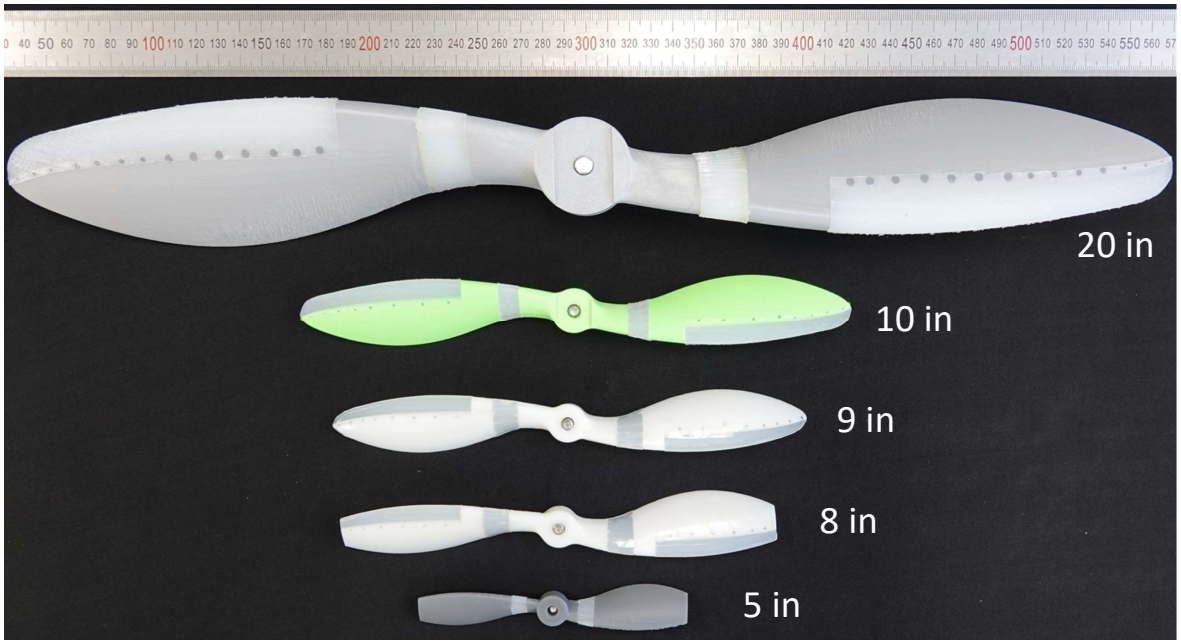

FIGURE 8.1: Scalable design for various sizes of *Tombo* propeller

The lack of collision detection of the *Tombo* propeller can be compensated for by the *TomboHub* mechanism. It is seen that the very first prototype of *TomboHub* required an upgrade for both design and fabrication. First, the durability of the Hub.Shaft 3 needs to be improved. Our experiments indicate that a PLA Hub.Shaft

3 was broken after 100 times of collisions. This number seems not too small, but it is not convenient to change a *TomboHub* instead of a propeller. Therefore, strong materials such as carbon fibers or aluminum alloy are considered the next choice for *TomboHub*. As a result, the cutting machining method will replace 3D printing for fabrication in the case of alloy material. Secondly, the size of *TomboHub* needs to be decreased to reduce the risk of collision made by the bulk size of drones. Now the height and the diameter of *TomboHub* are about 35 mm and 34 mm, respectively, which makes this hub even bigger than a rotor. The main reason is the thickness of the hub's wall and the size of the torsion spring and the button battery. Finally, an implementation of this hub into a standard propeller to make a novel propeller capable of shock absorbing and collision sensing.

8.1.2 Aerodynamics model

The proposed aerodynamic model can estimate the aerodynamic forces (the normal, the tangential, the lift, and the drag force), the lift-to-drag ratio, and the deformable angles. However, some of the outputs are not evaluated completely. The thrust force experimental results indicated that the errors of these estimations are under 8%. Nonetheless, this force model has just been evaluated with the rotational speed range from 2000 rpm to 3000 rpm. I do not have a chance to extend this measurement to a higher speed because of the limitation of the rotor power, so a stronger rotor could be considered to conduct future experiments toward a more comprehensive assessment. Our *Tombo* aerodynamic model can predict the lift-to-drag ratio, but it also is not evaluated. In the next experiment, I plan to use the power consumption of the rotor, calculated by the input voltage and the current from the power source, to estimate the drag force and make a comparison with the model output. The evaluations of the deformable angle α and γ are still missing, therefore a novel method to measure these angle at high rotational speed need to be proposed. In my opinion, a measurement system of industrial high-speed cameras is worth a try to do this task.

The proposed model has not yet been able to integrate and predict some other important parameters, such as the structure of the deformable leading edge, the applied vortex, or the distribution of the air pressure on the blade. The soft edge is predicted to deform during the rotation. However, this implementation has not been demonstrated in our proposed model. The vortex and the pressure distribution on the blade required another model for calculation and commercial Computational Fluid Dynamics (CFD) software for analysis.

8.1.3 Flight ability

The experiments conducted in this study demonstrated, for the first time, the ability of a drone with a deformable propeller to successfully fly and recover from collisions. However, there were certain limitations to the study. The trials were conducted indoors, so external factors such as wind and weather were not taken into account. Additionally, PID controllers, which are typically effective with rigid propellers, had some tracking errors when used with deformable *Tombo* propellers, particularly in the $\hat{x}$-direction (Figure 6.7), which resulted in different collision directions and recovery behaviors during flight trials (as can be seen in the video linked above). It is also possible that the fabricated propellers did not exhibit consistent behavior, which may have impacted the operation of the controller. These results provide a benchmark for reactive performance in the critical case of a collision and show that the average recovery time of $\Delta t_{\text{recovery}} = 5\,\text{seconds}$ and the average maximum falling distance of $\Delta h_{\text{fall}} = 0.5\,\text{m}$ were acceptable given that the mid-air collision occurred at the height of 2 m indoors. However, there is room for improvement in future reaction control algorithms, such as model predictive control or impedance/admittance reactive controllers [102], as the recovery time of the tested propellers ($\approx 0.46\,\text{seconds}$) was shorter than the overall recovery time ($\approx 5\,\text{seconds}$). It should also be noted that the "collision" in this study was defined based on the position of the propeller, which would not be feasible in a scenario

without a vision-based tracking system. The *TomboHub*, however, does support collision signals that can be combined with data from the drone's IMU to provide a better definition of a collision event.

In future research, I plan to create a detailed model of quadrotor dynamics that includes the effects of Tombo propellers on aerodynamics. This model will serve as the basis for advanced controllers that enable model-based interaction and tracking, as well as for optimizing the design of the quadrotor's structure. Additionally, the integration of collision detection and avoidance capabilities will be necessary for the development of autonomous quadrotors that can navigate agilely and robustly.

8.1.4 The contribution of *TomboHub*

The result in section 7.7 indicates that the hub can bring a noticeable impact to rigid propellers but Tombo. From a high level point of view, if we consider the propellers and the hubs as the elastic element 1 and the elastic element 2, in turn, (see Figure 8.2) in series. The color gradient indicates the deformation state (green – no deformation, red – critical deformation). For example, both elements are green at the normal state, as in Figure 8.2a. First, in the case of the combo *TomboHub* and *Tombo* propeller (see Figure 8.2b). Here, the external force is applied to the *Tombo* propeller first (defined by the change of color). Because the impact is in the accommodating range of the *Tombo* propeller's ability, most impact affects the *Tombo* propeller. At the same time, just a minor deformation of the hub (elastic element 1) can be found. That can explain why the hub doesn't bring a noticeable impact. In the case of commercial Hobby propellers and *TomboHub* (see Figure 8.2c). A Hobby propeller can be considered an elastic element with low-impact accommodating ability. When a collision happens, this ability is fulfilled very fast (almost red color), which leaves room for the hub to show its impact-accommodating ability. That can explain why the hub offers a critical impact in the Hobby case. Overall, it can be seen that the key to explaining the behavior of both the propeller and hub is their sequence in a collision scenario.

In order to analyze or verify this aforementioned statement, the below methods can be considered.

- Using an analytical model of elastic element series, which uses the conservation of energy,
- Simulating by specialized software such as Abaqus with a simplified model of elastic elements,
- Test a combo of Tombo propeller and TomboHub with a super critical hit (such as Figure 8.3).

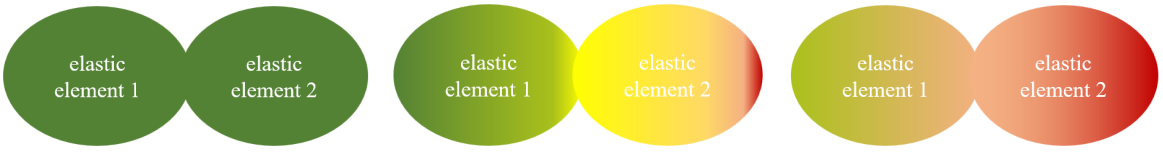

(A) Normal state (B) *TomboHub* and *Tombo* propeller (C) *TomboHub* and Hobby propeller

FIGURE 8.2: Behavior of two elastic elements in series with external force

8.1.5 Possible Applications

The *Tombo* propellers are designed to be used on drones in order to decrease the risk of damage from collisions with obstacles in any direction. This also gives the drone a higher chance of recovery after a collision, making it safer for the drone and any objects on the ground compared to simply crashing. By using *Tombo* propellers in combination with other safety measures, the overall safety of drones in tasks near objects or humans (such as infrastructure inspection and cargo transport) can be increased. For instance, drones equipped with *Tombo* propellers can operate in cluttered environments like forests or mountains due to their ability to recover from collisions that may be unavoidable. It is expected that the use of *Tombo* propellers will become more prominent as drone delivery services expand into more complex environments such as buildings and residential areas where a high level of safety

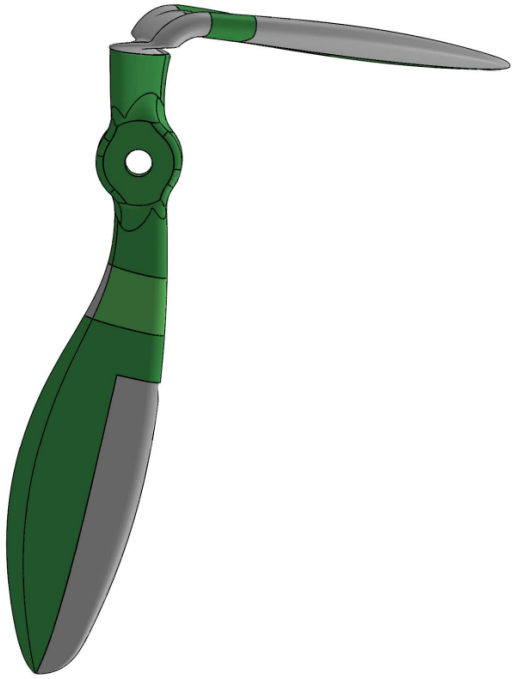

FIGURE 8.3: An sample state of a supercritical hit

FIGURE 8.4: Potential applications of *Tombo* family toward a sustainable solution for nature

is required. Additionally, these propellers can also be used in the entertainment industry, such as in drone shows where drones flying close to one another may have a higher risk of collision, or in situations where drones interact with humans [116], [117]. This bio-inspired approach could also be applied to other sectors, such as small-scale wind power generation propellers (to decrease the risk of bird strikes), agricultural machine cutting blades (to limit damage from collisions with rocks or branches), and ship propellers (to reduce entanglement with marine litter and fish, as well as accidents involving divers). Overall, the use of *Tombo* propellers could be a sustainable solution for nature.

8.2 Directions for future research

This work has opened up a lot of thoughts and directions for my future research. First of all, improve the aerodynamic model of the *Tombo* propeller by considering the impact of the flexible leading edge. This soft part can generate unwanted vibration that affects the fly ability of the drone. Therefore, a vibration model of this propeller is necessary for the users to develop the next version of *Tombo* propeller. Next, a collision and recovery model for *Tombo* is another interesting topic that has not been fulfilling. Our experiments indicate the deformable leading edge plays the most crucial role in shock absorbing and changing the collision state. As a result, the size and shape of this edge need further analysis, and a collision model is indispensable for the shock-absorbing evaluation. The behavior of *Tombo* propeller during the collision event is a black box now. The reaction of *Tombo*, the deformable angles α and γ needs to be investigated. A system of high-speed 5000 fps+ cameras seems to be a good solution candidate. After all, I would like to use the previously mentioned models to create a software application that utilizes an aerodynamic model to generate aerodynamic measurements automatically and provide a bio-inspired design for a traditional propeller as the output to the user..

Secondly, in parallel with completing the aerodynamic model of the *Tombo* propeller, I would like to analyze further the characteristics of this propeller using specialized CFD software such as JAXA, or ABAQUS/CFD[1] (Dassault Systèmes). The latter software is well-known for providing advanced, scalable, and parallel computational fluid dynamics for various simulations. This software allows for the simulation of various complex issues involving fluid and structural interactions as well as nonlinear coupled fluid-thermal dynamics. It can be accessed through Abaqus/CAE, providing a user-friendly and efficient platform for efficient simulations. Another approach that needs to be considered is Simulation Open Framework Architecture (SOFA) developed by INRIA, France. This software taking advantage of simulation-based dynamical investigation and powerful data-driven techniques,

[1] https://www.3ds.com/products-services/simulia/products/abaqus/

promises a high potential for optimizing the structure of *Tombo* propeller in a shorter time than other standard CFD analysis software. However, the remaining issues hinder the use of SOFA for the *Tombo* case. Firstly, SOFA aims toward real-time application. Thus dynamic behavior of the soft body usually obeys a linear constitutive relationship (e.g., Hooke's laws) to compromise the computation cost. As a result, the intrinsic reaction of the soft body will not be accurately emulated. More importantly, a CFD module has not been provided yet in SOFA. Therefore, this is a critical challenge to introduce a real impact of airflow on the *Tombo* propeller, especially in the soft components.

Next, the efficiency combination of *Tombo* propellers and *TomboHub* is desirable. In this work, the mid-air collision area is already known in advance. Therefore, a complete recovery strategy with various collision scenarios needs to be developed to have a reasonable reaction when an arbitrary collision happens. In detail, the information on the drone postures, the collision signal, the magnitude of impact force, etc., need to be mined and fullest utilized to best support drone controller decision-making.

Last but not least, another exciting challenge that I would like to face is the idea of embedding the *TomboHub* into a standard propeller design to make a novel one that can accommodate and sense collision. This idea has not stopped motivating me since the very first experiments of the *TomboHub* were successful.

Bibliography

[1] EmergenResearch. *Unmanned Aerial Vehicle (UAV) Market By Product Type, By Wing Type, By Operation Mode, By Range, By Maximum Takeoff Weight (MTOW), By System, By Application, By End-User, Forecasts to 2027*. Dec. 2020. (accessed: 05.25.2021).

[2] Matthew Ayamga, Selorm Akaba, and Albert Apotele Nyaaba. "Multifaceted applicability of drones: A review". In: *Technological Forecasting and Social Change* 167.February (2021), p. 120677. ISSN: 00401625. DOI: 10.1016/j.techfore.2021.120677. URL: https://doi.org/10.1016/j.techfore.2021.120677.

[3] John Koetsier. *Drone Explosion: 5B Investment In 2 Years, 129 Startups, 170 New Craft*. 2022. URL: https://www.forbes.com/sites/johnkoetsier/2022/02/07/drone-innovation-check-up-5b-investment-129-companies-170-craft/?sh=601b3cbd38f6.

[4] Jack Stewart. *Boeing's Flying Taxi Prototype Takes to the Air (Briefly) | WIRED*. 2019. URL: https://www.wired.com/story/boeing-air-taxi-uber/.

[5] Ben Sampson. *Airbus and Audi show flying taxi prototype for the first time | Aerospace Testing International*. 2018. URL: https://www.aerospacetestinginternational.com/news/drones-air-taxis/airbus-and-audi-show-flying-taxi-prototype-for-the-first-time.html.

[6] Hannah Sparks. *Paris to test drive flying taxis ahead of 2024 Olympics*. Dec. 2021. URL: https://nypost.com/2021/11/29/paris-to-test-drive-flying-taxis-ahead-of-2024-olympics/.

[7] Metro News. *Real life Angry Birds: delivery drones attacked in mid-air by ravens*. URL: https://metro.co.uk/2021/09/23/real-life-angry-birds-delivery-drones-attacked-in-mid-air-by-ravens-15303095/ (visited on 09/13/2022).

[8] Alberto Susini. "A Technocritical Review of Drones Crash Risk Probabilistic Consequences and its Societal Acceptance". In: *RIMMA Risk Information Management, Risk Models, and Applications; LNIS Vo. 7* November 2015 (2015), pp. 27–38. DOI: 10.2370/9783844083293.

[9] Dinh Quang Nguyen, Giuseppe Loianno, and Van Anh Ho. "Towards Design of a Deformable Propeller for Drone Safety". In: *2020 3rd IEEE International Conference on Soft Robotics (RoboSoft)*. 2020, pp. 464–469. DOI: 10.1109/RoboSoft48309.2020.9115983.

[10] Gang Chen, Wei Dong, Xinjun Sheng, et al. "An Active Sense and Avoid System for Flying Robots in Dynamic Environments". In: *IEEE/ASME Transactions on Mechatronics* 26.2 (2021), pp. 668–678. DOI: 10.1109/TMECH.2021.3060511.

[11] K. N. McGuire, C. De Wagter, K. Tuyls, et al. "Minimal navigation solution for a swarm of tiny flying robots to explore an unknown environment". In: *Science Robotics* 4.35 (2019), eaaw9710. DOI: 10.1126/scirobotics.aaw9710. eprint: https://www.science.org/doi/pdf/10.1126/scirobotics.aaw9710.

[12] Bruno Herissé, Tarek Hamel, Robert Mahony, et al. "Landing a VTOL Unmanned Aerial Vehicle on a Moving Platform Using Optical Flow". In: *IEEE Transactions on Robotics* 28.1 (2012), pp. 77–89. DOI: 10.1109/TRO.2011.2163435.

[13] Jiang Bian, Xiaolong Hui, Xiaoguang Zhao, et al. "A point-line-based SLAM framework for UAV close proximity transmission tower inspection". In: *2018*

IEEE International Conference on Robotics and Biomimetics (ROBIO). IEEE. 2018, pp. 1016–1021.

[14] Massimiliano Iacono and Antonio Sgorbissa. "Path following and obstacle avoidance for an autonomous UAV using a depth camera". In: *Robotics and Autonomous Systems* 106 (2018), pp. 38–46. ISSN: 0921-8890. DOI: https://doi.org/10.1016/j.robot.2018.04.005.

[15] Daniel Pohl, Sergey Dorodnicov, and Markus Achtelik. "Depth map improvements for stereo-based depth cameras on drones". In: *2019 Federated Conference on Computer Science and Information Systems (FedCSIS)*. IEEE. 2019, pp. 341–348.

[16] Nils Gageik, Paul Benz, and Sergio Montenegro. "Obstacle Detection and Collision Avoidance for a UAV With Complementary Low-Cost Sensors". In: *IEEE Access* 3 (2015), pp. 599–609. DOI: 10.1109/ACCESS.2015.2432455.

[17] Nils Gageik, Paul Benz, and Sergio Montenegro. "Obstacle detection and collision avoidance for a UAV with complementary low-cost sensors". In: *IEEE Access* 3 (2015), pp. 599–609.

[18] L.M. González-deSantos, J. Martínez-Sánchez, H. González-Jorge, et al. "UAV payload with collision mitigation for contact inspection". In: *Automation in Construction* 115 (2020), p. 103200. ISSN: 0926-5805. DOI: https://doi.org/10.1016/j.autcon.2020.103200.

[19] Hongru Li, Witold Kinsner, Yan Wang, et al. "Airborne Radar Based Collision Detection and Avoidance System for Unmanned Aircraft Systems in a Varying Environment". In: *2021 IEEE International Conference on Wireless for Space and Extreme Environments (WiSEE)*. Cleveland, Ohio, USA, 2021, pp. 43–48. DOI: 10.1109/WiSEE50203.2021.9613842.

[20] Milton Cesar Paes Santos, Claudio Dario Rosales, Mario Sarcinelli-Filho, et al. "A novel null-space-based UAV trajectory tracking controller with collision avoidance". In: *IEEE/ASME Transactions on Mechatronics* 22 (6 Dec. 2017), pp. 2543–2553. ISSN: 10834435. DOI: 10.1109/TMECH.2017.2752302.

[21] Albert S. Huang, Abraham Bachrach, Michael Krainin, et al. *Robotics Reseach*. Vol. 100. Springer Tracts in Advanced Robotics. Springer, Cham, 2017, pp. 235–252. ISBN: 9783319293622. DOI: 10.1007/978-3-319-29363-9_14.

[22] Pascal Gohl, Dominik Honegger, Sammy Omari, et al. "Omnidirectional visual obstacle detection using embedded FPGA". In: *2015 IEEE/RSJ International Conference on Intelligent Robots and Systems (IROS)*. IEEE. 2015, pp. 3938–3943.

[23] Gang Chen, Wei Dong, Xinjun Sheng, et al. "An active sense and avoid system for flying robots in dynamic environments". In: *IEEE/ASME Transactions on Mechatronics* 26.2 (2021), pp. 668–678.

[24] Massimiliano Iacono and Antonio Sgorbissa. "Path following and obstacle avoidance for an autonomous UAV using a depth camera". In: *Robotics and Autonomous Systems* 106 (2018), pp. 38–46. ISSN: 09218890. DOI: 10.1016/j.robot.2018.04.005. URL: https://doi.org/10.1016/j.robot.2018.04.005.

[25] Davide Falanga, Kevin Kleber, and Davide Scaramuzza. "Dynamic obstacle avoidance for quadrotors with event cameras". In: *Science Robotics* 5.40 (2020). DOI: 10.1126/scirobotics.aaz9712. eprint: https://robotics.sciencemag.org/content/5/40/eaaz9712.full.pdf.

[26] Sachin Umesh Sharma and Dharmesh J. Shah. "A Practical Animal Detection and Collision Avoidance System Using Computer Vision Technique". In: *IEEE Access* 5 (2017), pp. 347–358. DOI: 10.1109/ACCESS.2016.2642981.

[27] Allistair Moses, Matthew J. Rutherford, and Kimon P. Valavanis. "Radar-based detection and identification for miniature air vehicles". In: *2011 IEEE*

International Conference on Control Applications (CCA). 2011, pp. 933–940. DOI: 10.1109/CCA.2011.6044363.

[28] *DJI CSM Radar For M300 RTK - heliguy.com*. URL: https://www.heliguy.com/products/csm-radar-m300-rtk (visited on 09/26/2022).

[29] Dennis Laurijssen, Robin Kerstens, Girmi Schouten, et al. "A Flexible Low-Cost Biologically Inspired Sonar Sensor Platform for Robotic Applications". In: *2019 International Conference on Robotics and Automation (ICRA)*. 2019, pp. 9617–9623. DOI: 10.1109/ICRA.2019.8794165.

[30] J. Colorado, M. Perez, I. Mondragon, et al. "An integrated aerial system for landmine detection: SDR-based Ground Penetrating Radar onboard an autonomous drone". In: *Advanced Robotics* 31.15 (2017), pp. 791–808. DOI: 10.1080/01691864.2017.1351393. eprint: https://doi.org/10.1080/01691864.2017.1351393. URL: https://doi.org/10.1080/01691864.2017.1351393.

[31] Hashem Shahsavani. "An aeromagnetic survey carried out using a rotary-wing UAV equipped with a low-cost magneto-inductive sensor". In: *International Journal of Remote Sensing* 42 (23 2021), pp. 8805–8818. ISSN: 13665901. DOI: 10.1080/01431161.2021.1930269. URL: https://doi.org/10.1080/01431161.2021.1930269.

[32] Randall Reynolds, Benjamin Barrowes, Tornike Shubitidze, et al. "Electromagnetic induction sensing of unexploded ordinance and soil properties from unmanned aerial systems". In: *Detection and Sensing of Mines, Explosive Objects, and Obscured Targets XXVI*. Vol. 11750. SPIE. 2021, p. 1175002.

[33] *TOMAT FPV Propeller Guard for DJI Drone, 360°Propeller Protector for DJI FPV Accessories : Toys & Games - Amazon.com*. URL: https://www.amazon.com/TOMAT-Propeller-360%5C%C2%5C%B0Propeller-Protector-Accessories/dp/B0989SCYTJ (visited on 09/26/2022).

[34] Adam Klaptocz, Adrien Briod, Ludovic Daler, et al. "Euler spring collision protection for flying robots". In: *2013 IEEE/RSJ International Conference on Intelligent Robots and Systems (IROS)*. Tokyo, Japan, 2013, pp. 1886–1892. DOI: 10.1109/IROS.2013.6696606.

[35] P.M. Kornatowski, S. Mintchev, and D. Floreano. "An origami-inspired cargo drone". In: *2017 IEEE/RSJ International Conference on Intelligent Robots and Systems (IROS)*. Vancouver, BC, Canada, 2017, pp. 6855–6862. DOI: 10.1109/IROS.2017.8206607.

[36] Carl John Salaan, Kenjiro Tadakuma, Yoshito Okada, et al. "UAV with two passive rotating hemispherical shells for physical interaction and power tethering in a complex environment". In: *2017 IEEE International Conference on Robotics and Automation (ICRA)*. Marina Bay Sands, Singapore, 2017, pp. 3305–3312. DOI: 10.1109/ICRA.2017.7989377.

[37] Adrien Briod, Przemyslaw Kornatowski, Jean-Christophe Zufferey, et al. "A Collision-resilient Flying Robot". In: *Journal of Field Robotics* 31.4 (2014), pp. 496–509. DOI: https://doi.org/10.1002/rob.21495. eprint: https://onlinelibrary.wiley.com/doi/pdf/10.1002/rob.21495.

[38] Na Zhao, Yudong Luo, Hongbin Deng, et al. "The deformable quad-rotor: Design, kinematics and dynamics characterization, and flight performance validation". In: *2017 IEEE/RSJ International Conference on Intelligent Robots and Systems (IROS)*. Vancouver, BC, Canada, 2017, pp. 2391–2396. DOI: 10.1109/IROS.2017.8206052.

[39] Davide Falanga, Kevin Kleber, Stefano Mintchev, et al. "The Foldable Drone: A Morphing Quadrotor That Can Squeeze and Fly". In: *IEEE Robotics and Automation Letters* 4.2 (2019), pp. 209–216. DOI: 10.1109/LRA.2018.2885575.

[40] Jing Shu and Pakpong Chirarattananon. "A Quadrotor With an Origami-Inspired Protective Mechanism". In: *IEEE Robotics and Automation Letters* 4.4 (2019), pp. 3820–3827. DOI: 10.1109/LRA.2019.2929978.

[41] Stefano Mintchev, Sébastien de Rivaz, and Dario Floreano. "Insect-Inspired Mechanical Resilience for Multicopters". In: *IEEE Robotics and Automation Letters* 2.3 (2017), pp. 1248–1255. DOI: 10.1109/LRA.2017.2658946.

[42] Pooya Sareh, Pisak Chermprayong, Marc Emmanuelli, et al. "Rotorigami: A rotary origami protective system for robotic rotorcraft". In: *Science Robotics* 3.22 (2018). DOI: 10.1126/scirobotics.aah5228. eprint: https://robotics.sciencemag.org/content/3/22/eaah5228.full.pdf.

[43] Zhichao Liu and Konstantinos Karydis. "Toward Impact-resilient Quadrotor Design, Collision Characterization and Recovery Control to Sustain Flight after Collisions". In: *CoRR* abs/2011.02061 (2020). arXiv: 2011.02061.

[44] Or D. Dantsker, Marco Caccamo, Robert W. Deters, et al. "Performance testing of aero-naut CAM folding propellers". In: *AIAA Aviation 2020 Forum* 1 PartF (2020), pp. 1–52. DOI: 10.2514/6.2020-2762.

[45] *Aeronaut Fiberglass Blade Stopper for 3-Blade Folding Spinners-espritmodel.com*. URL: https://www.espritmodel.com/aeronaut-fiberglass-blade-stopper-for-folding-spinners-3blade.aspx (visited on 09/27/2022).

[46] Ryan Goldstein. "Self-folding propeller". US 2018/0257769 A1. Sept. 2018.

[47] *2PCS for DJI mavic quadcopter Propeller UAV accessories 8331 DJI mavic quick release noise paddle blade | quadcopter propeller | quadcopter accessoriespropeller quadcopter - AliExpress*. URL: https://www.aliexpress.com/item/32839858371.html (visited on 09/27/2022).

[48] JaeHyung Jang, Kyunghwan Cho, and Gi-Hun Yang. "Design and Experimental Study of Dragonfly-Inspired Flexible Blade to Improve Safety of Drones". In: *IEEE Robotics and Automation Letters* 4.4 (2019), pp. 4200–4207. DOI: 10.1109/LRA.2019.2928773.

[49] H. Rajabi, N. Ghoroubi, K. Stamm, et al. "Dragonfly wing nodus: A one-way hinge contributing to the asymmetric wing deformation". In: *Acta Biomaterialia* 60 (2017), pp. 330–338. ISSN: 1742-7061. DOI: https://doi.org/10.1016/j.actbio.2017.07.034.

[50] Andrew M. Mountcastle and Stacey A. Combes. "Biomechanical strategies for mitigating collision damage in insect wings: Structural design versus embedded elastic materials". In: *Journal of Experimental Biology* 217.7 (2014), pp. 1108–1115. ISSN: 00220949. DOI: 10.1242/jeb.092916.

[51] Robin J. Wootton. "Functional Morphology of Insect Wings". In: *Annual Review of Entomology* 37.1 (1992), pp. 113–140. DOI: 10.1146/annurev.en.37.010192.000553. eprint: https://doi.org/10.1146/annurev.en.37.010192.000553.

[52] Hamed Rajabi, Jan-Henning Dirks, and Stanislav N. Gorb. "Insect wing damage: causes, consequences and compensatory mechanisms". In: *Journal of Experimental Biology* 223.9 (May 2020). jeb215194. ISSN: 0022-0949. DOI: 10.1242/jeb.215194. eprint: https://journals.biologists.com/jeb/article-pdf/223/9/jeb215194/1983011/jeb215194.pdf.

[53] Jafar Hasan, Anindo Roy, Kaushik Chatterjee, et al. "Mimicking Insect Wings: The Roadmap to Bioinspiration". In: *ACS Biomaterials Science & Engineering* 5.7 (2019). PMID: 33405511, pp. 3139–3160. DOI: 10.1021/acsbiomaterials.9b00217. eprint: https://doi.org/10.1021/acsbiomaterials.9b00217. URL: https://doi.org/10.1021/acsbiomaterials.9b00217.

[54] T L Hopkins and K J Kramer. "Insect Cuticle Sclerotization". In: *Annual Review of Entomology* 37.1 (1992), pp. 273–302. DOI: 10.1146/annurev.en.37.010192.001421. eprint: https://doi.org/10.1146/annurev.en.37.010192.001421. URL: https://doi.org/10.1146/annurev.en.37.010192.001421.

[55] Julian F.V Vincent and Ulrike G.K Wegst. "Design and mechanical properties of insect cuticle". In: *Arthropod Structure & Development* 33.3 (2004). Arthropod Locomotion Systems: from Biological Materials and Systems to Robotics, pp. 187–199. ISSN: 1467-8039. DOI: https://doi.org/10.1016/j.asd.2004.05.006. URL: https://www.sciencedirect.com/science/article/pii/S1467803904000325.

[56] Neil F Hadley. "The arthropod cuticle". In: *Scientific American* 255.1 (1986), pp. 104–113.

[57] Elena P Ivanova, Song Ha Nguyen, Hayden K Webb, et al. "Molecular organization of the nanoscale surface structures of the dragonfly Hemianax papuensis wing epicuticle". In: *PLoS One* 8.7 (2013), e67893.

[58] Song Ha T Nguyen, Hayden K Webb, Jafar Hasan, et al. "Dual role of outer epicuticular lipids in determining the wettability of dragonfly wings". In: *Colloids and Surfaces B: Biointerfaces* 106 (2013), pp. 126–134.

[59] Svend Olav Andersen. "Biochemistry of insect cuticle". In: *Annual review of entomology* 24.1 (1979), pp. 29–59.

[60] Esther Appel, Lars Heepe, Chung-Ping Lin, et al. "Ultrastructure of dragonfly wing veins: composite structure of fibrous material supplemented by resilin". In: *Journal of Anatomy* 227.4 (2015), pp. 561–582.

[61] Jan Michels and SN Gorb. "Detailed three-dimensional visualization of resilin in the exoskeleton of arthropods using confocal laser scanning microscopy". In: *Journal of microscopy* 245.1 (2012), pp. 1–16.

[62] Fabian Haas, Stanislav Gorb, and Reinhard Blickhan. "The function of resilin in beetle wings". In: *Proceedings of the Royal Society of London. Series B: Biological Sciences* 267.1451 (2000), pp. 1375–1381.

[63] Stanislav N Gorb. "Serial elastic elements in the damselfly wing: mobile vein joints contain resilin". In: *Naturwissenschaften* 86.11 (1999), pp. 552–555.

[64] Seth Donoughe, James D Crall, Rachel A Merz, et al. "Resilin in dragonfly and damselfly wings and its implications for wing flexibility". In: *Journal of morphology* 272.12 (2011), pp. 1409–1421.

[65] Robin Wootton. "The geometry and mechanics of insect wing deformations in flight: A modelling approach". In: *Insects* 11 (7 2020), pp. 1–19. ISSN: 20754450. DOI: 10.3390/insects11070446.

[66] Matthew Keennon, Karl Klingebiel, and Henry Won. "Development of the nano hummingbird: A tailless flapping wing micro air vehicle". In: *50th AIAA aerospace sciences meeting including the new horizons forum and aerospace exposition*. 2012, p. 588.

[67] Quoc Viet Nguyen, Hoon Cheol Park, Nam Seo Goo, et al. "Characteristics of a beetle's free flight and a flapping-wing system that mimics beetle flight". In: *Journal of Bionic Engineering* 7.1 (2010), pp. 77–86.

[68] Nina Gaissert, Rainer Mugrauer, Günter Mugrauer, et al. "Inventing a micro aerial vehicle inspired by the mechanics of dragonfly flight". In: *Conference Towards Autonomous Robotic Systems*. Springer. 2013, pp. 90–100.

[69] Gregory Gremillion, Paul Samuel, and J Sean Humbert. "Yaw feedback control of a bio-inspired flapping wing vehicle". In: *Micro-and Nanotechnology Sensors, Systems, and Applications IV*. Vol. 8373. SPIE. 2012, pp. 361–369.

[70] David Coleman, Moble Benedict, Vikram Hrishikeshavan, et al. "Design, development and flight-testing of a robotic hummingbird". In: *AHS 71st annual forum*. 2015, pp. 5–7.

[71] HV Phan, S Aurecianus, T Kang, et al. "Attitude control mechanism in an insect-like tailless two-winged flying robot by simultaneous modulation of stroke plane and wing twist". In: *International Micro Air Vehicle Conference and Competition*. 2018.

[72] Nina Gaissert, Rainer Mugrauer, Günter Mugrauer, et al. "Inventing a micro aerial vehicle inspired by the mechanics of dragonfly flight". In: *Conference Towards Autonomous Robotic Systems*. Springer. 2013, pp. 90–100.

[73] Jian Zhang, Fan Fei, Zhan Tu, et al. "Design optimization and system integration of robotic hummingbird". In: *2017 IEEE International Conference on Robotics and Automation (ICRA)*. IEEE. 2017, pp. 5422–5428.

[74] Christophe De Wagter, Matěj Karásek, and Guido de Croon. "Quad-thopter: Tailless flapping wing robot with four pairs of wings". In: *International Journal of Micro Air Vehicles* 10.3 (2018), pp. 244–253.

[75] Quoc-Viet Nguyen and Woei Leong Chan. "Development and flight performance of a biologically-inspired tailless flapping-wing micro air vehicle with wing stroke plane modulation". In: *Bioinspiration & biomimetics* 14.1 (2018), p. 016015.

[76] Xiaokai Chi, Shaoping Wang, Yixin Zhang, et al. "A tailless butterfly-type ornithopter with low aspect ratio wings". In: *CSAA/IET International Conference on Aircraft Utility Systems (AUS 2018)*. IET. 2018, pp. 1–6.

[77] Matěj Karásek, Florian T Muijres, Christophe De Wagter, et al. "A tailless aerial robotic flapper reveals that flies use torque coupling in rapid banked turns". In: *Science* 361.6407 (2018), pp. 1089–1094.

[78] Andrew M. Mountcastle, E. Farrell Helbling, and Robert J. Wood. "An insect-inspired collapsible wing hinge dampens collision-induced body rotation rates in a microrobot". In: *Journal of the Royal Society Interface* 16 (150 2019). ISSN: 17425662. DOI: 10.1098/rsif.2018.0618.

[79] Hoang Vu Phan and Hoon Cheol Park. "Mechanisms of collision recovery in flying beetles and flapping-wing robots". In: *Science* 370 (6521 2020), pp. 1214–1219. ISSN: 10959203. DOI: 10.1126/science.abd3285.

[80] J.S. Carlton. *Marine Propellers and Propulsion (Third Edition)*. Third. Oxford: Butterworth-Heinemann, 2012, pp. 271–298. ISBN: 978-0-08-097123-0. DOI: https://doi.org/10.1016/B978-0-08-097123-0.00011-3.

[81] Emmanuel Simon Pierre Branlard. *Wind Turbine Aerodynamics and Vorticity-Based Methods: Fundamentals and Recent Applications*. English. Vol. 7. Research Topics in Wind Energy. Springer, 2017. ISBN: 978-3-319-55163-0. DOI: 10.1007/978-3-319-55164-7.

[82] S. Abrate. *2 - Dynamic behavior of composite marine propeller blades*. Ed. by Valentina Lopresto, Antonio Langella, and Serge Abrate. Woodhead Publishing, 2017, pp. 47–83. ISBN: 978-0-08-100887-4. DOI: https://doi.org/10.1016/B978-0-08-100887-4.00002-0.

[83] Michael H. Dickinson, Fritz-Olaf Lehmann, and Sanjay P. Sane. "Wing Rotation and the Aerodynamic Basis of Insect Flight". In: *Science* 284.5422 (1999), pp. 1954–1960. DOI: 10.1126/science.284.5422.1954. eprint: https://www.science.org/doi/pdf/10.1126/science.284.5422.1954.

[84] Rafic Younes, Ali Hallal, Farouk Fardoun, et al. "Comparative Review Study on Elastic Properties Modeling for Unidirectional Composite Materials". In: *Composites and Their Properties*. Ed. by Ning Hu. InTech, Aug. 2012, pp. 391–408. DOI: 10.5772/50362.

[85] Fionnuala Connolly, Conor J. Walsh, and Katia Bertoldi. "Automatic design of fiber-reinforced soft actuators for trajectory matching". In: *Proceedings of the National Academy of Sciences of the United States of America* 114 (1 2017), pp. 51–56. ISSN: 10916490. DOI: 10.1073/pnas.1615140114.

[86] T. Ranzani, G. Gerboni, M. Cianchetti, et al. "A bioinspired soft manipulator for minimally invasive surgery". In: *Bioinspiration and Biomimetics* 10 (3 2015), pp. 1–14. ISSN: 17483190. DOI: 10.1088/1748-3190/10/3/035008. URL: http://dx.doi.org/10.1088/1748-3190/10/3/035008.

[87] Siqi Wang, Lei Li, Yufeng Chen, et al. "A bio-robotic remora disc with attachment and detachment capabilities for reversible underwater hitchhiking". In: (2019), pp. 4653–4659. ISSN: 10504729. DOI: 10.1109/icra.2019.8793703.

[88] Moses Bangura, Marco Melega, Roberto Naldi, et al. "Aerodynamics of Rotor Blades for Quadrotors". In: (Jan. 2016). URL: http://arxiv.org/abs/1601.00733.

[89] Ferdinand P. Beer, Jr. E. Russell Johnston, John T. DeWolf, et al. *Mechanics of materials*. 7th. McGraw-Hill Education, Jan. 2015, p. 902. ISBN: 9781420036589. DOI: 10.4324/9781315636764-23.

[90] Gene E. Maddux, Leon A. Vorst, Joseph F. Giessler, et al. *Stress Analysis Manual*. Tech. rep. US. Department of Commerce, 1969.

[91] John Anderson. *Fundamentals of Aerodynamics*. Vol. 5. McGraw-Hill Education, 2013, pp. 447–469. ISBN: 0814471323.

[92] Kevin M. Lynch and Frank C. Park. *Modern Robotics: Mechanics, Planning, and Control*. 1st. USA: Cambridge University Press, 2017. ISBN: 1107156300.

[93] Yasutada Tanabe and Shigeru Saito. "Significance of all-speed scheme in application to rotorcraft CFD simulations". In: *The 3rd International Basic Research Conference on Rotorcraft Technology* (2009).

[94] Yasutada Tanabe, Shigeru Saito, Oki Takayama, et al. "A new hybrid method of overlapping structured grids combined with unstructured fuselage grids for rotorcraft analysis". In: *36th European Rotorcraft Forum, ERF 2010* 1 (071 2010), pp. 192–200.

[95] Yasutada Tanabe, Shigeru Saito, and Hideaki Sugawara. "Construction and validation of an analysis tool chain for rotorcraft active noise reduction". In: *38th European Rotorcraft Forum 2012, ERF 2012* 1 (2012), pp. 235–247.

[96] Yasutada Tanabe, Shigeru Saito, and Hideaki Sugawara. "Evaluation of Rotor Noise Reduction by Active Devices Using a CFD/CSD Coupling Analysis Tool Chain". In: *1st Asian Australian Rotorcraft Forum and Exhibition 2012* (2012).

[97] Yasutada Tanabe and Hideaki Sugawara. "Aerodynamic validation of rFlow3d code with UH-60A data including high advance ratios". In: *41st European Rotorcraft Forum 2015, ERF 2015* 1 (2015), pp. 108–116.

[98] Hideaki Sugawara, Yasutada Tanabe, Noriaki Itoga, et al. "Numerical simulation of aerodynamic interaction between a rotor and a wing". In: *7th Asian/Australian Rotorcraft Forum, ARF 2018* M (2019), pp. 1–7.

[99] John C Houbolt. "National advisory committee for aeronautics". In: *Journal of the Franklin Institute* 230 (1 1940), pp. 136–138. ISSN: 00160032. DOI: 10.1016/s0016-0032(40)90670-6.

[100] D. H. Hodges and E. H. Dowell. *NONLINEAR EQUATIONS OF MOTION FOR THE ELASTIC BENDING AND TORSION OF TWISTED NONUNIFORM ROTOR BLADES*. 1974. URL: https://ntrs.nasa.gov/search.jsp?R=19750005242.

[101] Martin A. Fischler and Robert C. Bolles. "Random Sample Consensus: A Paradigm for Model Fitting with Applications to Image Analysis and Automated Cartography". In: *Commun. ACM* 24.6 (July 1981), pp. 381–395. ISSN: 0001-0782.

[102] Teodor Tomić, Christian Ott, and Sami Haddadin. "External Wrench Estimation, Collision Detection, and Reflex Reaction for Flying Robots". In: *IEEE Transactions on Robotics* 33.6 (2017), pp. 1467–1482. DOI: 10.1109/TRO.2017.2750703.

[103] Morgan Quigley, Ken Conley, Brian Gerkey, et al. "ROS: An open-source Robot Operating System". In: *ICRA Workshop on Open Source Software*. 2009.

[104] Adrian Battiston, Inna Sharf, and Meyer Nahon. "Attitude estimation for normal flight and collision recovery of a quadrotor UAV". In: *2017 International Conference on Unmanned Aircraft Systems, ICUAS 2017* (2017), pp. 840–849. DOI: 10.1109/ICUAS.2017.7991468.

[105] Karishma Patnaik, Shatadal Mishra, Zachary Chase, et al. "Collision recovery control of a foldable quadrotor". In: *IEEE/ASME International Conference on Advanced Intelligent Mechatronics, AIM* 2021-July (2021), pp. 418–423. DOI: 10.1109/AIM46487.2021.9517341.

[106] Albert Albers, Simon Trautmann, Thomas Howard, et al. "Semi-autonomous flying robot for physical interaction with environment". In: *2010 IEEE Conference on Robotics, Automation and Mechatronics, RAM 2010* (2010), pp. 441–446. DOI: 10.1109/RAMECH.2010.5513152.

[107] Gareth Dicker, Fiona Chui, and Inna Sharf. "Quadrotor collision characterization and recovery control". In: *Proceedings - IEEE International Conference on Robotics and Automation* (3 2017), pp. 5830–5836. ISSN: 10504729. DOI: 10.1109/ICRA.2017.7989685.

[108] Daniel Mellinger, Nathan Michael, and Vijay Kumar. "Trajectory generation and control for precise aggressive maneuvers with quadrotors". In: *International Journal of Robotics Research* 31 (5 2012), pp. 664–674. ISSN: 02783649. DOI: 10.1177/0278364911434236.

[109] Zhichao Liu and Konstantinos Karydis. "Toward Impact-resilient Quadrotor Design, Collision Characterization and Recovery Control to Sustain Flight after Collisions". In: *Proceedings - IEEE International Conference on Robotics and Automation* 2021-May (Icra 2021), pp. 183–189. ISSN: 10504729. DOI: 10.1109/ICRA48506.2021.9561089.

[110] Matthias Faessler, Davide Falanga, and Davide Scaramuzza. "Thrust Mixing, Saturation, and Body-Rate Control for Accurate Aggressive Quadrotor

Flight". In: *IEEE Robotics and Automation Letters* 2 (2 2017), pp. 476–482. ISSN: 23773766. DOI: 10.1109/LRA.2016.2640362.

[111] Zhichao Liu and Konstantinos Karydis. "Toward Impact-resilient Quadrotor Design, Collision Characterization and Recovery Control to Sustain Flight after Collisions". In: (2020). URL: http://arxiv.org/abs/2011.02061.

[112] Mohammadreza Mousaei, Junyi Geng, Azarakhsh Keipour, et al. "Design, Modeling and Control for a Tilt-rotor VTOL UAV in the Presence of Actuator Failure". In: (2022). URL: http://arxiv.org/abs/2205.05533.

[113] Fang Nan, Sihao Sun, Philipp Foehn, et al. "Nonlinear MPC for Quadrotor Fault-Tolerant Control". In: *IEEE Robotics and Automation Letters* 7 (2 2022), pp. 5047–5054. ISSN: 23773766. DOI: 10.1109/LRA.2022.3154033.

[114] Mark W. Mueller and Raffaello D'Andrea. "Relaxed hover solutions for multicopters: Application to algorithmic redundancy and novel vehicles". In: *International Journal of Robotics Research* 35 (8 2016), pp. 873–889. ISSN: 17413176. DOI: 10.1177/0278364915596233.

[115] Daniel Mellinger and Vijay Kumar. "Minimum snap trajectory generation and control for quadrotors". In: *Proceedings - IEEE International Conference on Robotics and Automation* (2011), pp. 2520–2525. ISSN: 10504729. DOI: 10.1109/ICRA.2011.5980409.

[116] Jane Cleland-Huang and Ankit Agrawal. "Human-drone interactions with semi-autonomous cohorts of collaborating drones". In: *CEUR Workshop Proceedings* 2617.April 2020 (2020). ISSN: 16130073. arXiv: 2010.04101.

[117] Kotaro Yamaguchi, Ginga Kato, Yoshihiro Kuroda, et al. "A non-grounded and Encountered-type haptic display using a drone". In: *SUI 2016 - Proceedings of the 2016 Symposium on Spatial User Interaction* (2016), pp. 43–46. DOI: 10.1145/2983310.2985746.

A Appendix

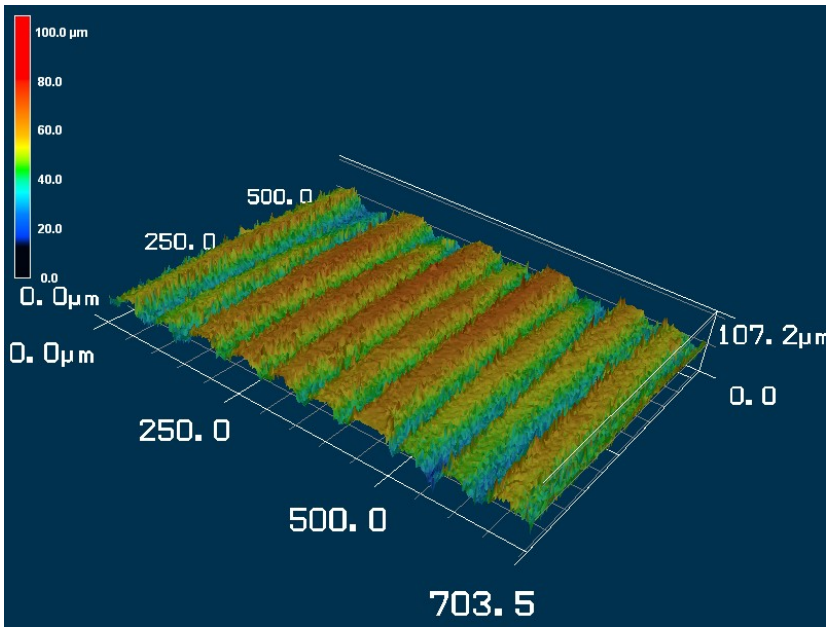

(A) *Tombo* v1 upper mid

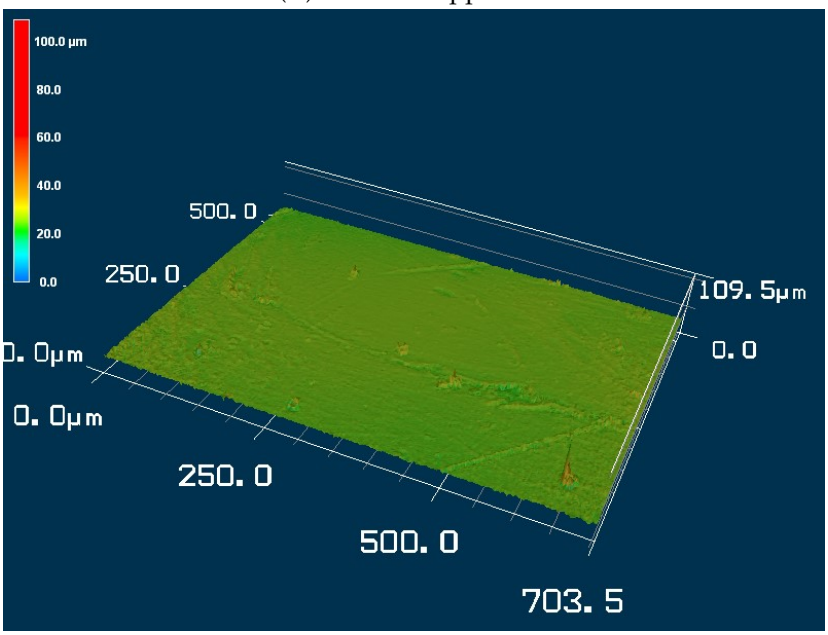

(B) *Tombo* v2 upper mid

FIGURE A.1: Improvement of *Tombo* upper mid surface quality by injection molding, measured by color 3D laser microscopy VK-9700 (Keyence, USA), 20x, scale bar 500 μm

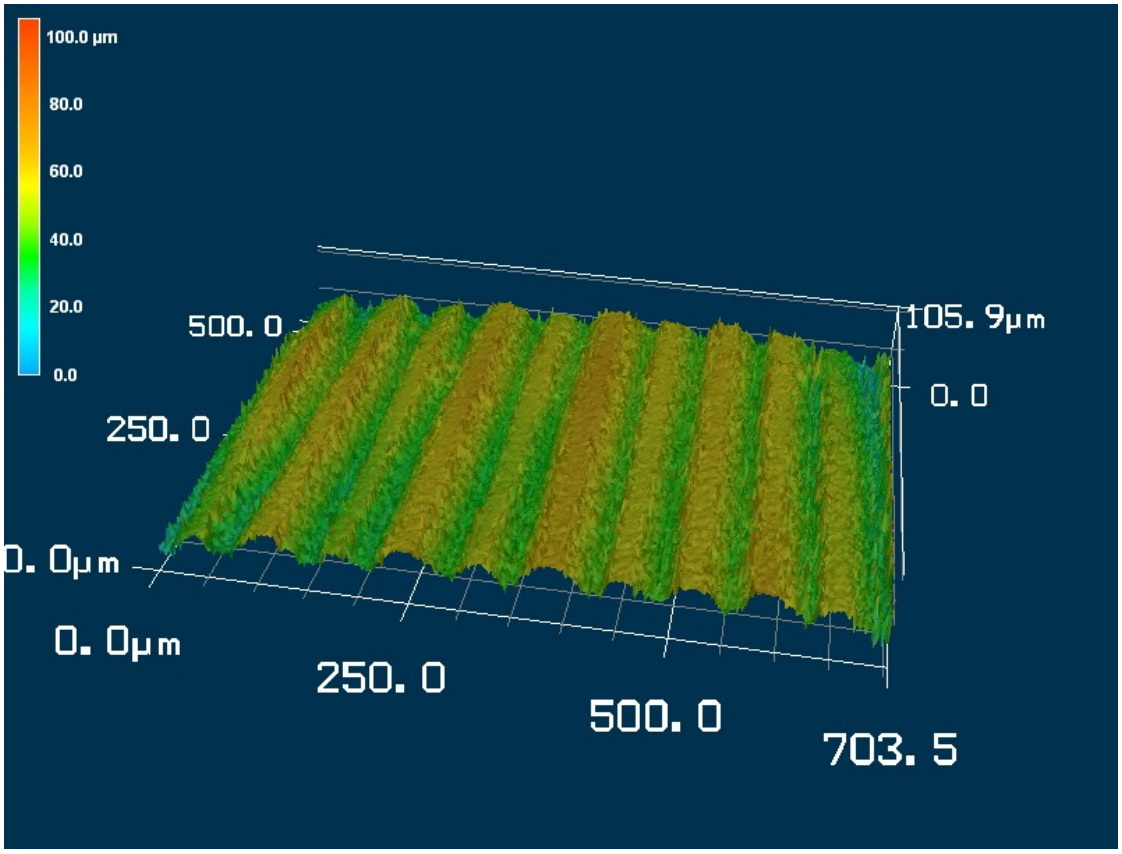

(A) *Tombo* v1 upper tip

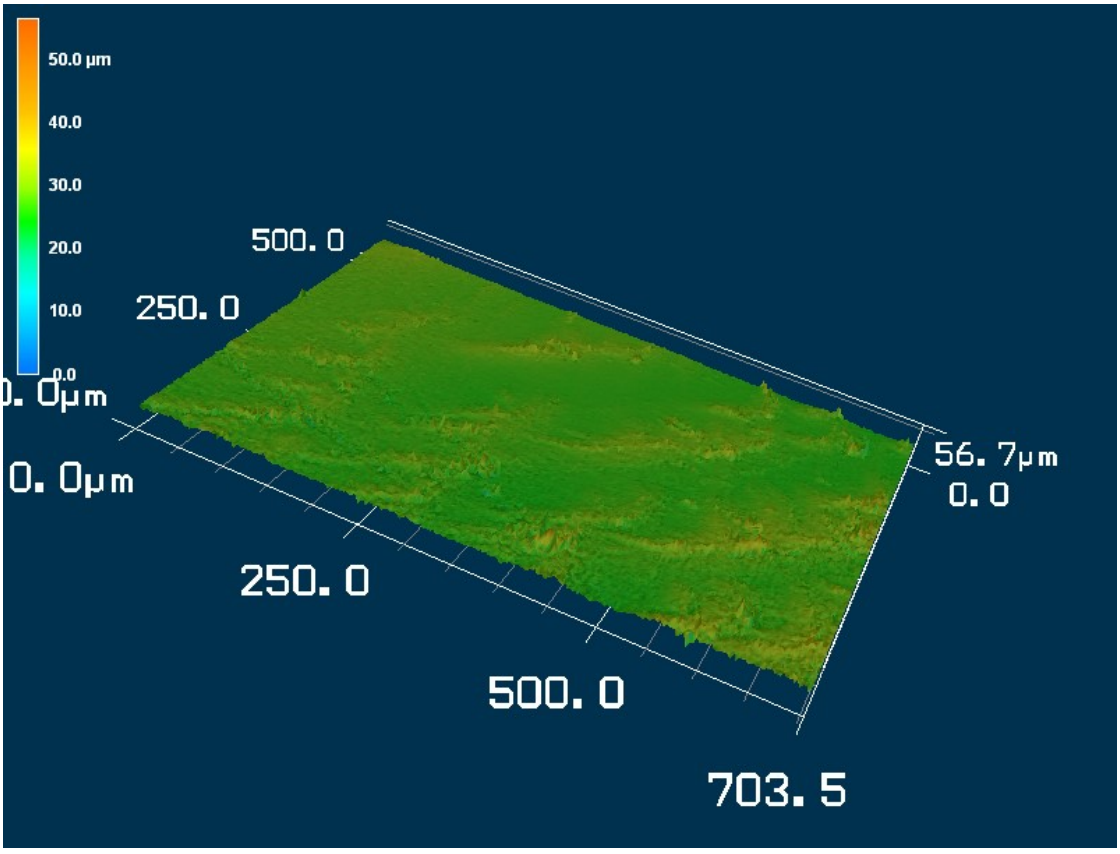

(B) *Tombo* v2 upper tip

FIGURE A.2: Improvement of *Tombo* upper tip surface quality by injection molding, measured by color 3D laser microscopy VK-9700 (Keyence, USA), 20x, scale bar 500 μm

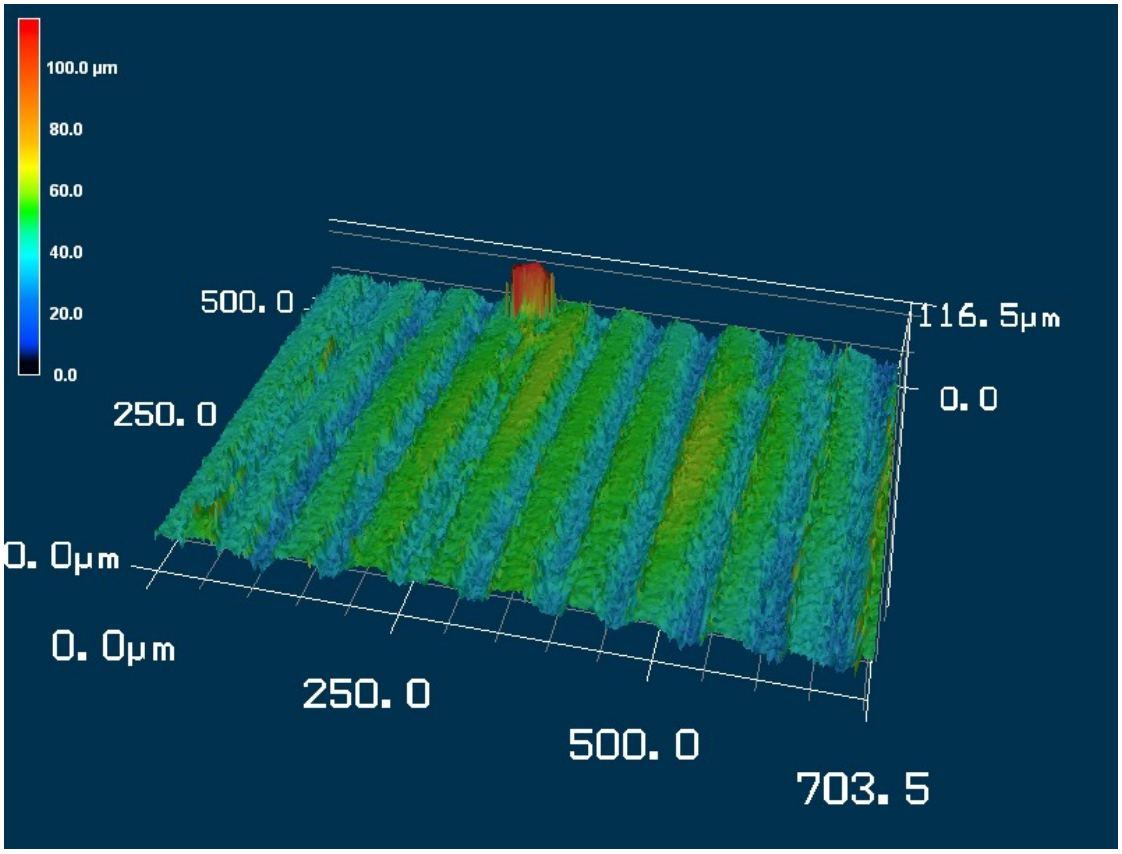

(A) *Tombo* v1 lower end

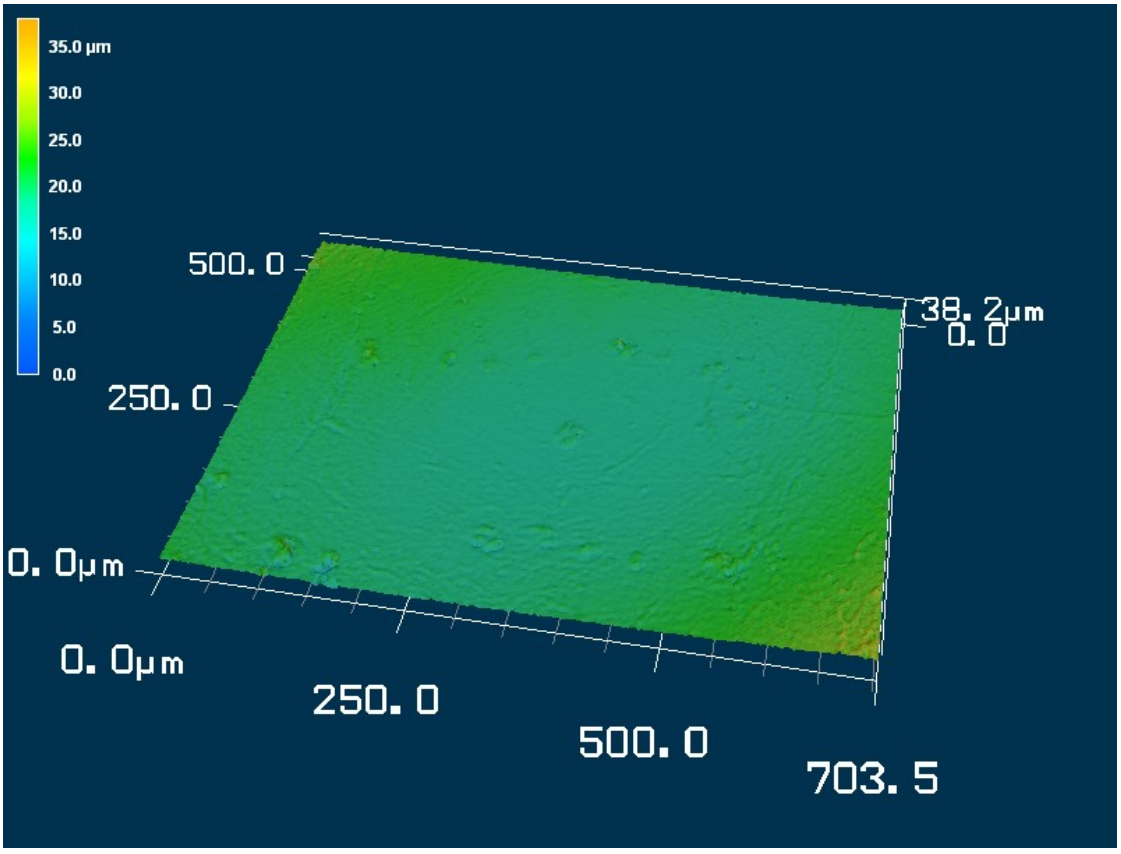

(B) *Tombo* v2 lower end

FIGURE A.3: Improvement of *Tombo* lower end surface quality by injection molding, measured by color 3D laser microscopy VK-9700 (Keyence, USA), 20x, scale bar 500 μm

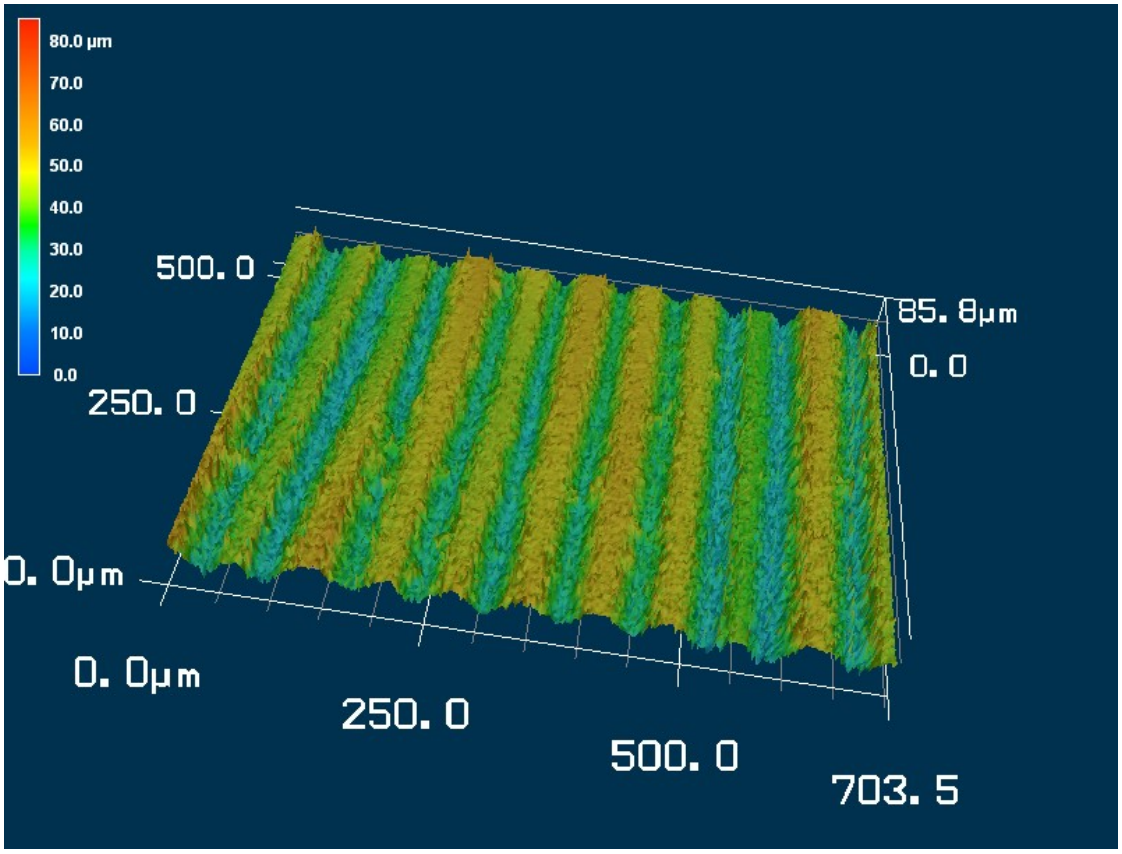

(A) *Tombo* v1 lower mid

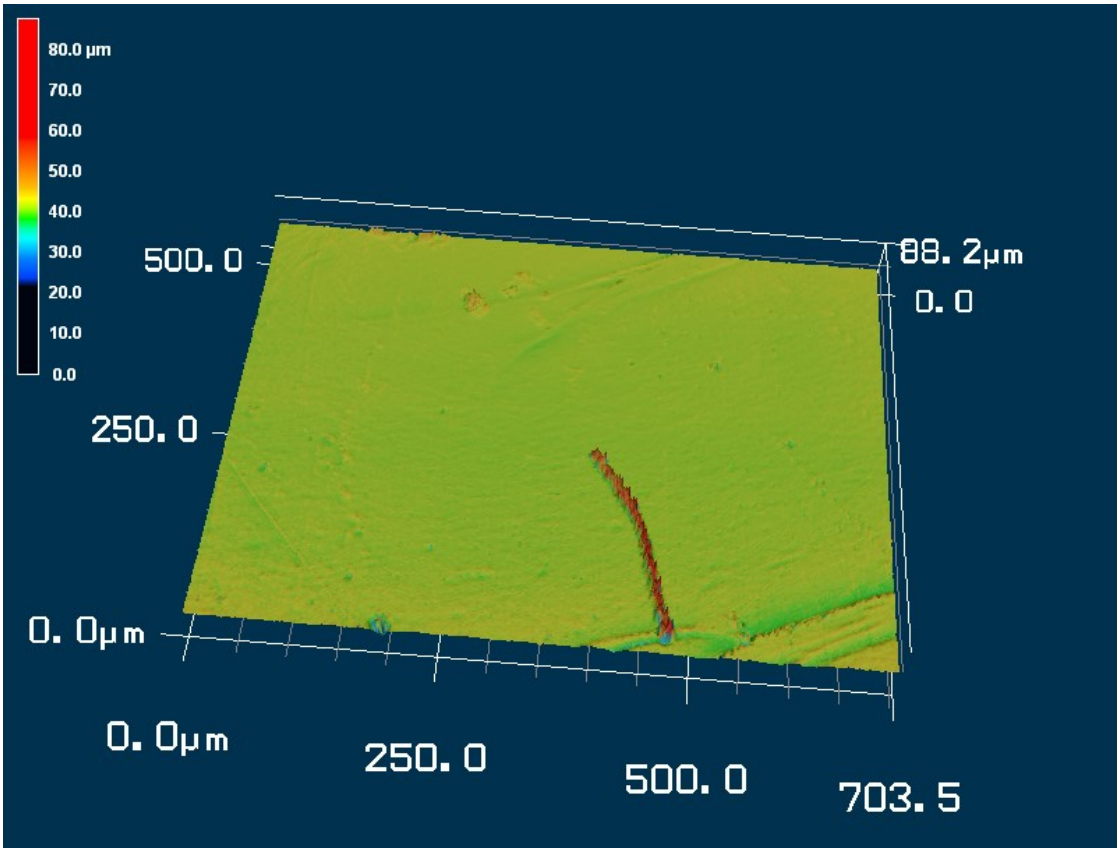

(B) *Tombo* v2 lower mid

FIGURE A.4: Improvement of *Tombo* lower mid surface quality by injection molding, measured by color 3D laser microscopy VK-9700 (Keyence, USA), 20x, scale bar 500 μm

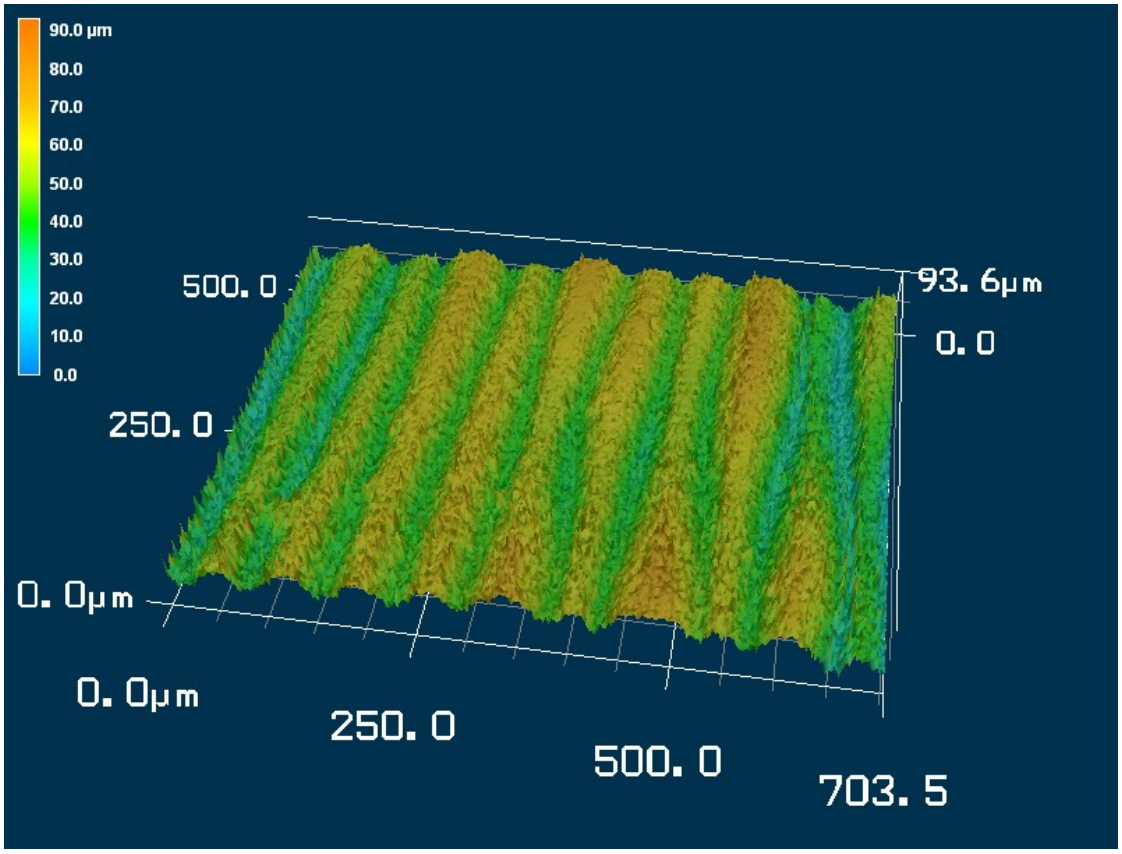

(A) *Tombo* v1 lower tip

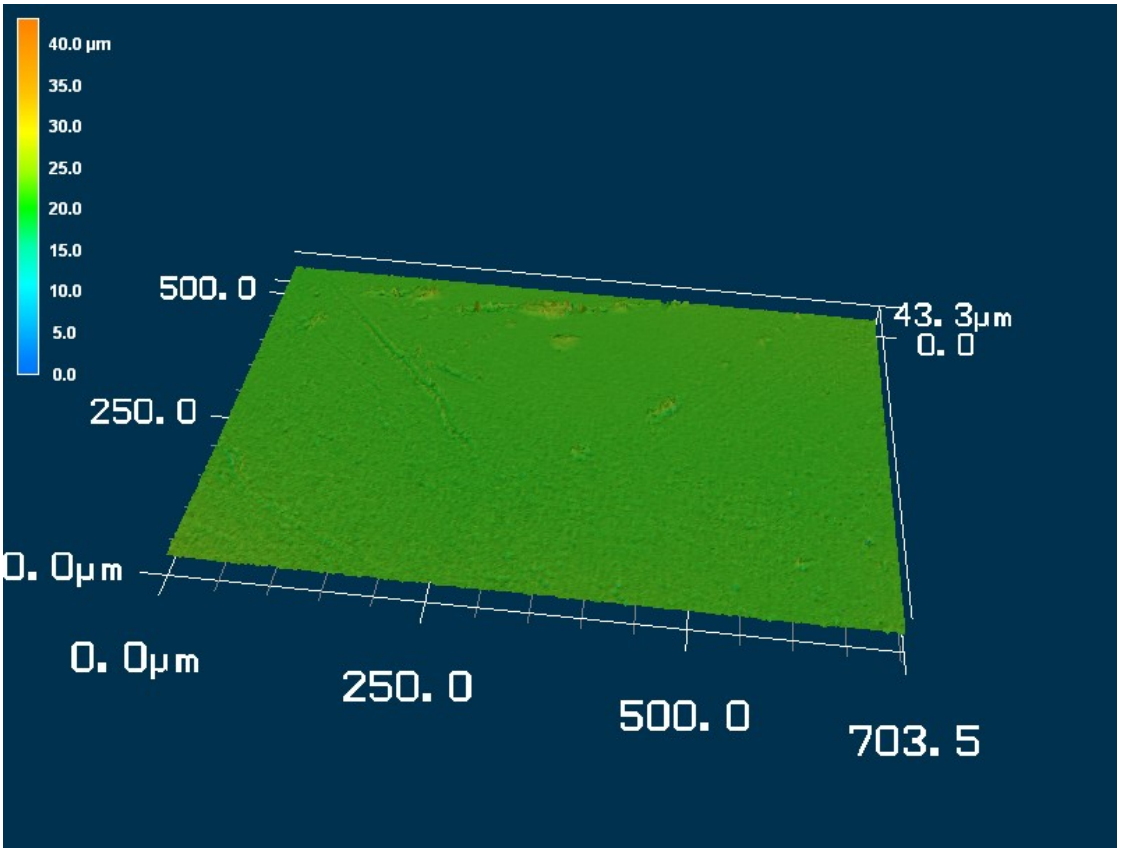

(B) *Tombo* v2 lower tip

FIGURE A.5: Improvement of *Tombo* lower tip surface quality by injection molding, measured by color 3D laser microscopy VK-9700 (Keyence, USA), 20x, scale bar 500 μm